seit 1558

High Energy radiation from compact plasma-based sources

Bifeng Lei

Dissertation

Presented for the Academic Degree

of Doctor of Philosophy

(Dr. rer. nat.)

Recommended for Acceptance

by the Department of

Physics and Astronomy

Friedrich-Schiller-Universität Jena

December 16, 2019

seit 1558

Hochenergetische Strahlung aus kompakten Plasmaquellen

Bifeng Lei

Dissertation

zur Erlangung des akademischen Grades

doctor rerum naturalium

(Dr. rer. nat.)

vorgelegt dem Rat der Physikalisch-Astronomischen Fakultät

der Friedrich-Schiller-Universität Jena

December 16, 2019

Gutachter:

1. **Prof. Dr. Sergey G. Rykovanov**

   Skolkovo Institute of Science and Technology

   Skolkovo Innovation Center

   3 Nobel Street

   143026 Moscow, Russia

2. **Prof. Dr. Matt Zepf**

   Institut für Optik und Quantenelektronik

   Friedrich-Schiller-Universität Jena

   Helmholtz-Institut Jena

   Fröbelstieg 3

   07743 Jena, Germany

3. **Prof. Dr. Malte C. Kaluza**

   Institut für Optik und Quantenelektronik

   Friedrich-Schiller-Universität Jena

   Helmholtz-Institut Jena

   Fröbelstieg 3

   07743 Jena, Germany

4. **Prof. Dr. Christian Spielamann**

   Institut für Optik und Quantenelektronik

   Friedrich-Schiller-Universität Jena

   Max-Wien-Platz 1

   07743 Jena, Germany

5. **Prof. Dr. Bernhard Hidding**

   University of Strathclyde

   John Anderson Building

107 Rottenrow East

Glasgow

G4 0NG, UK

6. **Dr. Brendan Dromey**

Department of Physics and Astronomy

Queen's University Belfast

Road Belfast BT7 1NN

Belfast, UK

Tag der Disputation: November 14th 2019

Ehrenwörtliche Erklärung

Ich erkläre hiermit ehrenwörtlich, dass ich die vorliegende Arbeit selbständig, ohne unzulässige Hilfe Dritter und ohne Benutzung anderer als der angegebenen Hilfsmittel und Literatur angefertigt habe. Die aus anderen Quellen direkt oder indirekt übernommenen Daten und Konzepte sind unter Angabe der Quelle gekennzeichnet.

Bei der Auswahl und Auswertung folgenden Materials haben mir die nachstehend aufgeführten Personen in der jeweils beschriebenen Weise unentgeltlich geholfen:

1. Prof. Dr. Sergey G. Rykovanov

Weitere Personen waren an der inhaltlich-materiellen Erstellung der vorliegenden Arbeit nicht beteiligt. Insbesondere habe ich hierfür nicht die entgeltliche Hilfe von Vermittlungsbzw. Beratungsdiensten (Promotionsberater oder andere Personen) in Anspruch genommen. Niemand hat von mir unmittelbar oder mittelbar geldwerte Leistungen für Arbeiten erhalten, die im Zusammenhang mit dem Inhalt der vorgelegten Dissertation stehen.

Die Arbeit wurde bisher weder im In- noch im Ausland in gleicher oder ähnlicher Form einer anderen Prüfungsbehörde vorgelegt.

Die geltende Promotionsordnung der Physikalisch-Astronomischen Fakultät ist mir bekannt.

Ich versichere ehrenwörtlich, dass ich nach bestem Wissen die reine Wahrheit gesagt und nichts verschwiegen habe.

Ort, Datum Unterschrift d. Verfassers

Zusammenfassung

Im aktuellen Jahrhundert sind kompakte, hoch-energetische Strahlenquellen äußerst wichtig geworden für hochentwickelte Anwendungen in der Medizin, Industrie, Bildung und Wissenschaft. Im Gegensatz zu konventionellen Strahlungsquellen, die aus riesige Anlagen bestehen, können plasma-basierte Quellen mit einer Länge von Zentimetern sehr flexibel eingesetzt werden und die Forschung voranbringen.

In dieser Doktorarbeit wurden verschiedene Modelle von Plasma-Wakefield-Undulatoren parallel entwickelt. Zuerst wurde die Führung eines Laserstrahls, in Form eines einzelnen Gauß-Pulses, Hermite-Gauß-Moden und Laguerre-Gauß-Moden, in einem parabolischen Plasma-Kanal untersucht. Dazu wurde die schrödingergleichungs-artige Wellengleichung für einen harmonischen Oszillator mit paraxialen und quasistatischen Näherungen gelöst. Wenn der Laserpuls unter einer transversalen Verschiebung oder unter einem Winkel zur Ausbreitungsachse in den Plasmakanal injiziert wird, wird sein Schwerpunkt oszillieren. Spezielle Bedingungen wurden hergeleitet, um die wichtigen Eigenschaften einer solchen Oszillation zu beeinflussen: Frequenz, Amplitude und Polarisation.

Als zweites wurde die Anregung des Wakefields durch den oszillierenden Laserpuls theoretisch und nummerisch im linearen und nichtlinearen Bereich untersucht. Die konkrete Struktur des Feldes wird für jede der Varianten gezeigt. Für kurze, weite Laserpulse erzeugt das Wakefield eine lineare Fokussierkraft nahe der Ausbreitungsachse, die Betatronschwingungen der injizierten Elektronen anregt. Diese zusätzlichen Kräfte treten durch die Schwerpunktschwingungen des Laserpulses auf. Überraschenderweise wird das Undulatorfeld, erzeugt durch die Überlagerung vieler verschiedener Hermite-Gauß-Moden, monochromatisch sinusförmig, wenn die Stärke des Laserpulses einer speziellen Bedingung entspricht. Dies erweist sich als sehr vorteilhaft für die Erzeugung von schmalbandigen Strahlungsspektren.

Drittens wurde die Bewegung eines einzelnen Elektrons sowie eines Elektronen-

strahls in diesen Undulatorfeldern untersucht. Im Allgemeinen vollzieht ein Elektron eine kombinierte Bewegung aus Betatron- und Undulatorschwingungen. Allerdings können die Betatronschwingungen komplett unterdrückt werden, wenn bestimmte Bedingungen für die Injektion des Elektrons erfüllt sind. Weitergehende theoretische Untersuchungen über die Bewegungen der beschleunigten Elektronen zeigen, dass es eine Resonanz zwischen den Betatronschwingungen der Elektronen sowie der Schwerpunktschwingungen des Laserpulses gibt. Diese Resonanz kann genutzt werden, um die Amplitude und Stärke der Elektronenschwingung schnell innerhalb der ersten Rayliegh-Längen der Ausbreitung zu erhöhen. Während der Beschleunigung im Wakefield wird die Resonanz gebrochen. Dies resultiert in einer semi-stabilen Oszillation mit großer Amplitude und Stärke, welche die Erzeugung von starken γ-Strahlen ermöglicht.

Zuletzt wird das Strahlungsspektrum der Schwingung eines Elektronenstrahls berechnet. Die vorgeschlagenen Modelle sind in der Lage, ein schmalbandiges Röntgenspektrum oder synchrotron-ähnliche γ-Strahlen mit hoher Energie zu erzeugen. Die Energie und Helligkeit sind mit aktuell verfügbaren konventionellen Strahlenquellen vergleichbar. Es wird außerdem gezeigt, dass diese flexiblen Modelle so abgestimmt werden können, dass die erzeugte Strahlung einen wohldefinierten Drehimpuls besitzt.

Abstract

Throughout the current century, compact, high-energy radiation sources have become critically important for many advanced applications in medicine, industry, education, and scientific research. In contrast to conventional radiation sources mainly produced in huge facilities, plasma-based radiation sources with centimetre lengths can provide great flexibility and drive science forward.

In this thesis, several plasma wakefield-based undulator schemes have been developed in parallel. First, the guiding of laser beams, including a single Gaussian pulse, Hermite-Gaussian (HG) modes, and Laguerre-Gaussian (LG) modes, is studied through the Schrödinger-like wave equation for a harmonic oscillator with paraxial and quasistatic approximations in a parabolic plasma density channel. If the laser pulse is injected into the plasma channel with a transverse offset or an angle with respect to the propagation axis, it will undergo centroid oscillation. Special conditions are found to control the interesting properties of such oscillation: frequency, amplitude, and polarisation.

Second, wakefield excitation driven by the oscillating laser pulse is theoretically and numerically studied in the linear/nonlinear regime. The specific field structure of each scheme is demonstrated. For a short, wide laser pulse, the wakefield provides a linear focusing force near the propagation axis that drives the betatron oscillation of the injected electrons. The extra driving force is introduced by the centroid oscillation of the laser pulse. Surprisingly, the undulator field generated by beating several different HG modes becomes monochromatically sinusoidal when the strength of laser pulses matches a special condition. This is very beneficial for the generation of a narrow radiation spectrum.

Third, the dynamics of both a single electron and an electron beam are studied in these generated undulator fields. Generally, an electron undergoes the combined motion of betatron and undulator oscillations. However, the weak betatron oscillation

could be totally removed if certain injection conditions for an electron can be satisfied. Further theoretical work on the dynamics of an accelerated electron indicates that there is a resonance between the betatron oscillation of the electrons and centroid oscillation of the laser pulse. This resonance can be used to increase the oscillation amplitude and strength for the electron rapidly within the first several Rayleigh lengths of propagation. While being accelerated in the wakefield, the resonance is broken and results in a semi-steady oscillation with large amplitude and strength, which enables the generation of strong γ-ray radiation.

Ultimately, the radiation spectrum from the oscillation of an electron beam is calculated. The proposed schemes are capable of generating an x-ray radiation spectrum with a narrow bandwidth or synchrotron-like x/γ-ray radiation of high energy. The energy and brightness are comparable with currently available conventional radiation sources. It is also demonstrated that these flexible schemes can be tuned to generate radiation carrying well-defined angular momentum.

Acknowledgements

First of all, I would like to thank my advisors Prof. Dr. Sergey G. Rykovanov and Prof. Dr. Matt Zepf for encouraging me to carry out my research with their unlimited patience and support. On many occasions, they were not only tutors but also friends with warm hearts during the past four years in Jena. I still remember the day at Darmstadt when I met Prof. Rykovanov the first time. We drank coffee and talked about physics. Even though I seemed so childish at that time, he still kindly accepted me into his group. That gave me the first chance to explore this fantastic field of laser plasma interaction freely. I will appreciate it all my life.

I am also deeply grateful to all of my fellows in our group of Helmholtz Institute Jena. Dr. Jingwei Wang was always so patient and enthusiastic to discuss with me whenever needed. Dr. Vasily Kharin has given me so many guides in the theory of physics and selflessly shared his own numerical code with me during this thesis. I would like to thank Ph.D student Stefan Tietze, Dr. Sizhong Wu, Ph.D student Tom Teter, and all members of HIJ for helping me with many difficult positions, and having so much fun together.

Many thanks to supercomputer JURECA at the Juülich Supercomputing Center (JSC) and Helmholtz-Zentrum Dresden (HZDR) for providing me computational resources during this thesis.

Finally, I thank my family from the depth of my heart, just for everything.

To my parents and wife.

Contents

List of Figures

Chapter 1

Introduction

1.1 Introduction and motivation

Our understanding of the universe largely depends on how close we are when looking at things. Throughout the 20^{th} century, light sources have been indispensable tools to drive such progress consistently, especially in purpose-built facilities for X-ray production that were first constructed in the 1980s. For example, an X-ray pulse with a time duration of a few to 100 fs, the peak power of 10 to 100 GW, over a wavelength range extending from approximately 100 nm to less than 0.1 nm, is capable of resolving the complex structure and inter-atomic dynamics of the matter. Such light sources serve many areas of natural science, medicine, and industrial applications, including fundamental physics research [72, 86, 105], radiography [68, 123], molecular crystallography [1, 64, 113], structural biomicroscopy [12], radiotherapy [2], inspection security, fluorescence analysis in manufacturing quality control [119], and even fraud detection in art.

Radiation was initially thought of as an obstacle when accelerating charged particles to high energy in accelerators and storage rings [92, 124]. However, it was quickly realised that user-based radiation facilities, known as synchrotron radiation sources,

should be seriously considered for many applications [122, 125]. Then the first generation of light sources was introduced, by using bending-magnets of the accelerator rings under the so-called parasitic operation [11]. This produced continuous radiation, guaranteeing long periods of exposure to the samples. Optimally designed equipment that emerged for its exclusive use was known as the second generation of synchrotron light sources [23, 76]. Light is produced when the electron beam path is curved by the well-designed magnetic lattice, guaranteeing the greatest quantity and best quality of synchrotron radiation. With a demand for increasing brightness, the second-generation rings, such as NSLS II [76], PETRA III [43], and SSRF [112], were redesigned with the possibility of incorporating insertion devices called undulators and wigglers. These new light sources were known as the third generation. The magnetic undulator is an array of closely spaced, vertically oriented dipole magnets of alternating polarity, that makes the electrons oscillate while passing longitudinally in the horizontal plane. Owing to the relatively weak field, radiation cones emitted at each bend in the trajectory overlap, giving rise to a constructive interference effect that results in one or a few narrow spectral peaks (a fundamental and harmonics) in a beam that is highly collimated in both the horizontal and vertical directions. As a result, the beam has high spectral brightness. Wigglers are similar to undulators, but have higher fields and fewer dipoles; thus, they produce a continuous spectrum with higher flux and a spectrum that extends to shorter wavelengths than bending magnets [34]. Therefore, such machines are capable of producing the intense and monochromatic radiation with a tunable wavelength from mid-IR to X-ray range, arbitrary polarisation, and sub-nanosecond pulse duration [21]. Recently, the fourth generation of synchrotron light sources have been proposed with the aim of vastly enhanced performance (e.g. ultra-low emittance with lower costs). One of these−MAX-IV−has been in operation in Sweden since 2015 [29]. Another major step has been taken in the development of the free-electron laser (FEL), where spatially coherent radiation is

produced with further increased power. In 1992, the first self-amplified spontaneous emission (SASE) x-ray FEL was proposed to be built (with a wavelength range of 0.1 to 4 nm using one-third of the 40 GeV), two miles long in the linear accelerator of the SLAC National Accelerator Laboratory [91]. Since then, many other facilities have been designed and constructed around the world, LCLS [129], SACLA [62], XFEL [3], SwissFEL [90].

However, these radiation sources mentioned above rely heavily on large conventional accelerators to accelerate charged particles to high energy initially, usually in the scale of GeV, before being injected into oscillating structures. Because of the peak power and breakdown limits of the materials, the energy gain is less than 50 MeV/m. Therefore, such facilities are usually very large and very expensive. For example, the Diamond Light Source cost a total £380 million and XFEL cost €684 million for construction. Reducing the size and cost of such facilities is highly beneficial, as this will greatly increase user accessibility. There are two ways to make these light sources more compact. Either the conventional accelerator should be replaced with a compact accelerator, such as a laser-plasma electron accelerator (LPA), or the period of an undulator should be decreased, which leads to the concept of a micro-undulator. In recent decades, LPAs have been intensively studied as a promising solution. Plasma is an ionised gaseous substance of unbound positive and negative particles in an electrically neutral state. While propagating inside plasma, an intense laser pulse or high-energy electron beam can expel the plasma electrons outwards from the axis. The expelled electrons are then pulled back by the quasi-static heavy ions. This forms the Langmuir wave, with the frequency determined by the plasma density [57], and provides ideal accelerating and focusing properties for electrons in proper phase [46], as demonstrated in Fig. 1.1. The laser-driven case is referred to as laser-driven accelerators−LPAs [46], which provide ultra-high accelerating gradients, several orders of magnitude higher than those in conventional linacs. These then lead to the

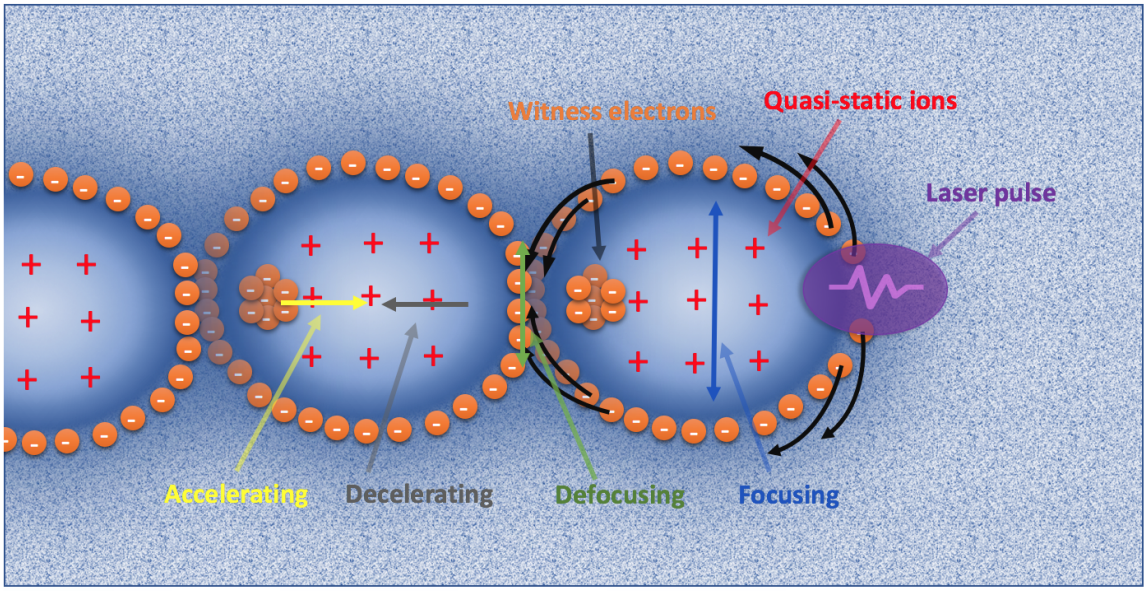

Figure 1.1: A demonstration of plasma wakefield driven by a short laser pulse (indicated by the purple spot on the right). Plasma electrons (indicated by small orange balls) are expelled outward, due to the ponderomotive force of the laser pulse, they are then pulled back by quasi-static ions (indicated by the red plus). The formed cavitation has its half phase with accelerating force and full phase with focusing force, and leads to the acceleration and the betatron oscillation of witness electrons

extremely compact accelerators in centimetre scale. Notably, monoenergetic electron bunches [56, 81, 52] have been demonstrated, and the energy of such bunches has recently reached the multi-GeV level [80].

Micro-undulator concepts have been proposed, including crystalline [117, 20, 126], electrostatic [115, 89], microwave [114], plasma [37, 101], nano-wire [10], and laser-based undulators [130, 109, 14, 15, 8, 9, 41, 79, 31], to provide radiation sources with comparable qualities to conventional sources, but with a much lower cost at the same time. Particularly, plasma-based radiation sources are promising alternatives, not only because of their compactness and low cost but also because of their capability of providing a high-quality light beam competing with that from conventional radiation sources. The basic idea is that electrons injected or self-trapped inside the plasma wakefield or bubble undergo harmonic oscillation (called betatron oscillation) with a frequency in the scale of plasma frequency because of the intrinsic focusing force

inside. Such oscillation usually produces the synchrotron-like radiation with broad bandwidth spanning from X-ray to γ-ray [36, 98, 47].

This thesis aims to develop new concepts of the laser-plasma-based radiation sources, plasma-based undulators/wigglers (PIGGLERs), which could provide us the great flexibility to control radiation properties, such as brightness, polarisation, energy range, bandwidth, and orbital angular momentum (OAM). These radiation sources should be achievable in current experimental conditions and with comparable qualities to the third generation of conventional radiation sources.

1.2 Thesis outline

The thesis is organised as follows:

In Chapter 2, the fundamental theories of laser-plasma interaction and radiation are discussed, with emphasis on the laser pulse guiding inside a plasma channel and wakefield excitation. The generation of radiation from an undulator/wiggler is theoretically described.

In Chapter 3, a plasma undulator driven by a single Gaussian laser pulse in a parabolic plasma channel is presented. This can generate a narrow-bandwidth x-ray radiation with high brightness. Some properties, such as tunable polarisation and controllable bandwidth are discussed.

In Chapter 4, a scheme of γ-ray generation from a plasma-based wiggler is presented. The fundamental physics is based on the resonance between the betatron oscillation of the injected electron and the centroid oscillation of the laser pulse. The brightness compared to the 3^{rd}-generation of the synchrotron radiation source is calculated.

In Chapter 5, a plasma channel undulator excited by beating several high-order HG laser modes is presented. A special structure of the undulator/wiggler field (without the betatron focusing force) is generated near the propagation axis inside the plasma

wakefield by matching the initial strength of the fundamental and first-order HG modes. Its capability to generate a very narrow bandwidth x-ray and the synchrotron-like high-energy x/γ-ray radiation is discussed.

In Chapter 6, the radiation carrying OAM from a plasma-based undulator is discussed. It is shown that the harmonics, except the fundamental, can carry the well-defined OAM.

In Chapter 7, the conclusion is made and potential ideas for future work are outlined.

Chapter 2

Theory of laser-plasma interaction and radiation generation

In this chapter, the basic theory of laser-plasma interaction and radiation generation from moving charged particles is reviewed. In Sec. 2.1, the fundamentals of electrodynamics and useful concepts of plasma physics required for this thesis are introduced. In Sec. 2.2, theory of laser pulse propagation in underdense plasma is presented, laying a basis for the plasma wakefield excitation discussed in Sec. 2.3. Related subjects, for example, electron injection, dephasing and phase lock, are also discussed. The method used to calculate the radiation is outlined in Sec. 2.4.

2.1 Basis of electrodynamics and plasma

2.1.1 Basic of electromagnetism

The concepts of electric **E** and magnetic **B** field were originally introduced to descibe the dynamics of a point charge q with the velocity $\mathbf{v}$ by means of the Lorentz force

equation in Coulomb's [18] and Ampère's [85] experiments,

$$\mathbf{F} = q\left(\mathbf{E} + \frac{\mathbf{v}\times\mathbf{B}}{c}\right), \tag{2.1}$$

c is the speed of light. Note that the formulation within this thesis is done in the Gaussian unit system (CGS) unless declared. $\mathbf{E}$ and $\mathbf{B}$ are the classical fields and can be thought of as the classical limit of quantum-mechanical description in the terms of real or virtual photons. Since the discrete aspect of the electromagnetic field can be ignored for some specific situations, e.g. macroscopic and even some atomic phenomena, where the effect of an individual photon is not sensible, a completely classical description is permitted and used here. Maxwell's equations provide a mathematical model for describing such phenomena, here in microscopic formulation [63],

$$\nabla\cdot\mathbf{E} = 4\pi\rho(\mathbf{x},t), \qquad \text{(Gauss's law)} \tag{2.2a}$$

$$\nabla\cdot\mathbf{B} = 0, \qquad \text{(Gauss's law for magnetism)} \tag{2.2b}$$

$$\nabla\times\mathbf{E} + \frac{\partial\mathbf{B}}{\partial ct} = 0, \qquad \text{(Faraday's law)} \tag{2.2c}$$

$$\nabla\times\mathbf{B} - \frac{\partial\mathbf{E}}{\partial ct} = -\frac{4\pi}{c}\mathbf{J}(\mathbf{x},t), \qquad \text{(Ampère"s law)} \tag{2.2d}$$

where $\rho(\mathbf{x},t)$, the electric charge density, and $\mathbf{J}(\mathbf{x},t)$, the electric current density, are assumed to be continuous in space. An electrostatic problem can be sufficiently described by Eq. (2.2a). The charge continuity equation is implicitly obtained by combining the time derivative of Eq. (2.2a) and the divergence of Eq. (2.2d),

$$\frac{\partial\rho}{\partial t} + \nabla\cdot\mathbf{J} = 0. \tag{2.3}$$

This is an empirical law expressing of local charge conservation which is more fundamental than Maxwell's equations and states that the change of amount of charge contained in a volume element is equal to the net charge current negatively flowing

through its surface in the closed system.

It is often convenient to introduce potentials to allow a much easier way to solve particular problems using specific gauge transformation [60]. The starting point is from Gauss's law for magnetism in Eq. (2.2b) where a vector potential $\mathbf{A}$ can be defined according

$$\mathbf{B} = \nabla \times \mathbf{A}. \tag{2.4}$$

By substituting Eq. (2.4) into the equation of Faraday's law in Eq. (2.2c), a scalar potential can be naturally defined according

$$\mathbf{E} = -\nabla\Phi - \frac{\partial \mathbf{A}}{\partial ct}. \tag{2.5}$$

These identities contain degrees of freedom for the potentials, since the fields $\mathbf{E}$ and $\mathbf{B}$ are invariant under the gauge transformation

$$\mathbf{A}' = \mathbf{A} + \nabla\Lambda, \tag{2.6a}$$

$$\Phi' = \Phi - \frac{\partial \Lambda}{\partial ct}, \tag{2.6b}$$

where Λ is an arbitrary scalar function. This means that the description of a problem with the potentials is confined by the choice of gauge. With these defined potentials in Eqs. (2.4) and (2.5), the inhomogeneous Maxwell's equations in Eqs. (2.2a) and (2.2d) can be written as

$$\nabla^2\Phi + \frac{\partial}{\partial ct}(\nabla \cdot \mathbf{A}) = -4\pi\rho, \tag{2.7a}$$

$$\nabla^2\mathbf{A} - \frac{\partial^2 \mathbf{A}}{\partial ct^2} - \nabla\left(\nabla \cdot \mathbf{A} + \frac{\partial \Phi}{\partial ct}\right) = -\frac{4\pi}{c}\mathbf{J}. \tag{2.7b}$$

With the *Lorentz condition* satisfied as

$$\nabla \cdot \mathbf{A} + \frac{\partial \Phi}{\partial ct} = 0, \tag{2.8}$$

Eqs. (2.7a) and (2.7b) are then decoupled into two wave equations. By substituting the gauge transformation in Eqs. (2.6a) and (2.6b) into Eq. (2.8), the condition for the Lorentz gauge is given as

$$\nabla^2 \Lambda - \frac{\partial^2 \Lambda}{\partial ct^2} = 0. \tag{2.9}$$

All potentials restricted in this class is said to belong to *Lorentz gauge* which is Lorentz invariant [30]. Another popular gauge is the so-called *Coulomb gauge* in which

$$\nabla \cdot \mathbf{A} = 0. \tag{2.10}$$

From Eq. (2.7a), the scalar potential satisfies the Poisson equation, which gives an instantaneous Coulomb potential due to the charge density. Then, the equation of vector potential $\mathbf{A}$ can be written as

$$\nabla^2 \mathbf{A} - \frac{\partial^2 \mathbf{A}}{\partial ct^2} = -\frac{4\pi}{c} \mathbf{J_t}, \tag{2.11}$$

where $\mathbf{J_t}$ is the transverse current. This means that the vector potential contributes to the transverse radiation field. It is very useful for problems when no source is present. Then, $\Phi = 0$, and vector potential $\mathbf{A}$ satisfies the homogeneous wave equation.

2.1.2 Basic concepts and properties of plasma

Basically, a plasma is an many-body system consisting of an equal number of positive and negative charge carriers, e.g. electrons, with mass m_e and charge $-e$, and ions, with mass m_i and q_i. The average kinetic energy of particles of species s is given in

non-relativistic case as [22]

$$KE_s = \frac{1}{2} m_s \langle v_s^2 \rangle = \frac{2}{3} kT, \tag{2.12}$$

where m_s is the mass, v_s is the speed, k is the Boltzmann constant and T is the kinetic temperature. In most cases, a plasma can be assumed to be a quasi-neutral state that demands both electrons and ions are characterized by the same T and charge density n. Then, the so-called thermal speed for species s can be estimated from Eq. (2.12) by

$$v_s = \sqrt{\frac{2kT}{m_s}}. \tag{2.13}$$

It is easily to see that thermal speed of ions is much smaller than electron

$$v_s = \sqrt{\frac{m_e}{m_i}} v_e \ll v_e, \tag{2.14}$$

and the ions are usually regarded as being static with respect to electrons in the case of low temperature.

A plasma exhibits strong forces between its constituents, and tends to stay electrically neutral via their self-consistent electric and magnetic field on macroscopic length-scales [75]. Dynamics of each particle is described by combining the momentum equations

$$m_i \ddot{\boldsymbol{r}}_i = q_i \Big[\boldsymbol{E}(\boldsymbol{r}_i) + \boldsymbol{\beta}_i \times \boldsymbol{B}(\boldsymbol{r}_i) \Big], \tag{2.15}$$

with Maxwell equations of electromagnetic field in Eqs. (2.2a)-(2.2d), where m_i, q_i and $\boldsymbol{r}_i$ are the mass, charge and position of i^{th} particle. Due to a tremendous amount of particles contained inside a plasma, an exact analytical solution for these equations is usually impossible. Therefore, there are two parallel levels of description for such problems. One is the analytical solution with simplifications. Another is the

numerical method, for example, Particle-In-Cell (PIC) simulation. Throughout this thesis, all of the simplifications or approximations for the analytical solutions will be presented clearly and PIC simulations will be used to benchmark the results.

Collisionless plasma

A reasonable simplification is the consideration of cold plasma [40] where the magnetic field is neglected and the electric field is deposed into two components by their distinct spatial scales: a) rapidly fluctuating micro-field which has spatial variations on a scale length much less than Debye length λ_{De} and is generated by the collisions of discrete charges; b) coherent macro-field which has spatial variations greater than or comparable to Debye length and leads to the collective behavior of the charges. To mention that the Debye length is a measure of how far a charge carrier is shielded by the plasma and defined in Eq. (A.6). The Debye sphere is a volume whose radius is the Debye length. Please see more details in Appendix. A.1.

The collision between charged particles is a basic phenomenon in plasma. A simple estimation of the electron-ion collision rate is approximately made by assuming that ions are randomly spaced, and the average velocity of ions is zero $\langle \Delta v_i \rangle = 0$. The scattering rate of an electron by an ion is given as [75]

$$\frac{\nu}{\omega_{pe}} \simeq \frac{Z \ln \Lambda}{10} \frac{1}{N_D}, \tag{2.16}$$

where Z is the charge number of an ion and n_e is the plasma electron density. Λ is defined as the ratio of maximum and minimum impact parameters of the collision. N_D is the number of plasma electrons in a Debye sphere and ω_{pe} is the plasma electron frequency. Not surprisingly that N_D is typically very large in the case of an underdense plasma, such as in a plasma-wakefield-based accelerator where

$n_e > 10^{16}$ cm^{-3}. With the collisionless limit $N_D \to \infty$, the fine scale colliosional interaction becomes not totally negligible and we can mainly focus our attention on the collective plasma behaviors.

Vlasov Equation

Theoretically, the collective plasma behaviors are described by Vlasov Equation with the phase space distribution function $f_j(\boldsymbol{x}, \boldsymbol{v}, t)$ [75]

$$\frac{\partial f_j}{\partial t} + \boldsymbol{v} \cdot \frac{\partial f_j}{\partial \boldsymbol{x}} + \frac{q_j}{m_j}\left(\boldsymbol{E} + \frac{\boldsymbol{v} \times \boldsymbol{B}}{c}\right) \cdot \frac{\partial f_j}{\partial v} = 0, \tag{2.17}$$

where j denotes j^{th} species. $\boldsymbol{x}$ and $\boldsymbol{v}$ are vectors of the position and velocity of species j, respectively. Note that $\boldsymbol{E}$ and $\boldsymbol{B}$ are coarse-grained fields associated with these collective behaviors. By applying various moments of the distribution function and truncation, equations of collective dynamics can be derived. For example, from the first moment, Eq. (2.17) gives the continuity equation of the species density n_j

$$\frac{\partial n_j}{\partial t} + \frac{\partial}{\partial \boldsymbol{x}} \cdot (n \boldsymbol{v}_{jm}) = 0, \tag{2.18}$$

where $\boldsymbol{v}_{jm}$ denotes the mean velocity of j^{th} species, and from the second moment, the force equation is obtained,

$$n_j\left(\frac{\partial \boldsymbol{v_{jm}}}{\partial t} + \boldsymbol{v_{jm}} \cdot \frac{\partial \boldsymbol{v_{jm}}}{\partial \boldsymbol{x}}\right) = \frac{n_j q_j}{m_j}\left(\boldsymbol{E} + \frac{\boldsymbol{v}_{jm} \times \boldsymbol{B}}{c}\right) - \frac{1}{m_j}\frac{\partial p_j}{\partial \boldsymbol{x}}, \tag{2.19}$$

where p_j is the fluid thermal pressure. Together with the adiabatic equation of isothermal state

$$\frac{p_j}{n_j^\gamma} = \text{constant}, \tag{2.20}$$

where $\gamma = (2+N)/N$ and N is the number of degrees of freedom, the plasma wave equations for electron and ion are obtained,

for electron:

$$\left(\frac{\partial^2}{\partial t^2} - 3v_{em}^2\frac{\partial^2}{\partial x^2} + \omega_{pe}^2\right)\tilde{n}_e = 0, \tag{2.21}$$

for ion:

$$\left(\frac{\partial^2}{\partial t^2} - \frac{ZT_e + 3T_i}{m_i}\frac{\partial^2}{\partial x^2}\right)\tilde{n}_i = 0, \tag{2.22}$$

where $\tilde{n}_e = n_e - n_0$ and $\tilde{n}_i = n_i - n_0$ are the small amplitude fluctuations in electron and ion density with respect to the equilibrium background density n_0, respectively. The wave described by Eq. (2.21) is the so-called plasma electron wave, and Eq. (2.22) is the so-called ion acoustic wave. T_e and T_i are the corresponding temperatures. m_i is the mass of ion. The cold electron plasma frequency is defined as

$$\omega_{pe} = \sqrt{\frac{4\pi e^2 n_0}{m_e}}. \tag{2.23}$$

In the cold plasma limit which is usually the case in a laser wakefield acceleration, temperatures are approximately set to zero, $T_e \simeq 0$ and $T_i \simeq 0$. Therefore, thermal effects are neglected in Eqs. (2.21) and (2.22).

2.2 Laser pulse propagation and guiding in plasma

Usually, to study the laser pulse propagation in a cold plasma, the plasma ions are assumed stationary. This is typically true for the case of a short pulse laser ($\ll$ 1ps) propagating in an underdense plasma ($\omega_{p0}^2/\omega^2 \ll 1$). Without consideration of collision effects as discussed in Sec. 2.1.2, the equations describing laser pulse propagation in a fully ionized plasma are obtained from potential equations in Eqs. (2.7a) and

(2.7b) with Coulomb gauge in Eq. (2.10) as [46]

$$\left(\nabla^2 - \frac{\partial^2}{\partial t^2}\right)\boldsymbol{a} = \frac{n}{n_0}\frac{\boldsymbol{u}}{\gamma} + \frac{\partial}{\partial t}\nabla\phi, \tag{2.24a}$$

$$\nabla^2\phi = \frac{n - n_i}{n_0}, \tag{2.24b}$$

where potentials are normalized by

$$\boldsymbol{a} = \frac{e\boldsymbol{A}}{m_e c^2}, \tag{2.25a}$$

$$\phi = \frac{e\Phi}{m_e c^2}, \tag{2.25b}$$

and $\boldsymbol{u} = \gamma\boldsymbol{\beta} = \boldsymbol{p}/m_e c$ is the normalized electron plasma fluid momentum, $\gamma = (1+u^2)^{1/2}$ is the relativistic Lorentz factor, n is the plasma electron density, n_i is the initial density profile prior to the passage of laser pulse, $n_0 = n_i(r=0)$ with $r=0$ corresponding to the direction of propagation. In the cold plasma limit, the electron current is given by $\boldsymbol{j} = -n\boldsymbol{u}/\gamma$. Unless clarified, here and in the following, length is normalized by the plasma wavenumber as $\boldsymbol{x} = k_p\boldsymbol{x}'$, time by the plasma frequency as $t = \omega_p t'$, where $\boldsymbol{x}'$ and t' are these values in CGS unit. By decomposing the vector field and momentum into longitudinal and transverse components, $\boldsymbol{a} = a_l + \mathrm{a}_\perp$ and $\boldsymbol{u} = u_l + \boldsymbol{u}_t$, and with the condition $\nabla\cdot\boldsymbol{u}_t = 0$ [63], the wave equation in Eqs. (2.24a) arrives at

$$\left(\nabla^2 - \frac{\partial^2}{\partial t^2}\right)\boldsymbol{a}_\perp = \frac{n}{n_0}\frac{\boldsymbol{u}_t}{\gamma}, \tag{2.26a}$$

$$\frac{\partial}{\partial t}\nabla\phi = \frac{n}{n_0}\frac{\boldsymbol{u}_l}{\gamma}. \tag{2.26b}$$

It is seen that the transverse current responds to the laser pulse evolution. From transverse momentum equation in Eq. (2.15) by the neglecting magnetic field which

will be discussed later,

$$\frac{\partial \boldsymbol{u}_t}{\partial t} = -\frac{\boldsymbol{E}_\perp}{\gamma} = \frac{\partial \boldsymbol{a}_\perp}{\gamma \partial t}, \tag{2.27}$$

the equation in Eq. (2.26a) becomes

$$\left(\nabla^2 - \frac{\partial^2}{\partial t^2} - \frac{1}{\gamma}\right)\boldsymbol{a}_\perp = \frac{\delta n}{\gamma n_0}\boldsymbol{a}_\perp, \tag{2.28}$$

where $\nabla^2 = \nabla_\perp^2 + \partial_z^2$, the electric field is normalized by $\boldsymbol{E} = e\boldsymbol{E}'/(m_e c\omega_p)$, and the density perturbation is defined as $\delta n = n - n_0$. The wave equation can be simplified by being recast into the light coordinate with independent variables $\zeta = z - t$ and $\tau = t$, where

$$\frac{\partial}{\partial z} = \frac{\partial \zeta}{\partial z}\frac{\partial}{\partial \zeta} + \frac{\partial \tau}{\partial z}\frac{\partial}{\partial \tau} = \frac{\partial}{\partial \zeta}, \tag{2.29a}$$

$$\frac{\partial}{\partial t} = \frac{\partial \zeta}{\partial t}\frac{\partial}{\partial \zeta} + \frac{\partial \tau}{\partial t}\frac{\partial}{\partial \tau} = -\frac{\partial}{\partial \zeta} + \frac{\partial}{\partial \tau}, \tag{2.29b}$$

and then substituting them into wave equation in Eq. (2.28),

$$\left(\nabla_\perp^2 + 2\frac{\partial^2}{\partial \zeta \partial \tau} - \frac{\partial^2}{\partial \tau^2} - \frac{1}{\gamma}\right)\boldsymbol{a}_\perp = \frac{\delta n}{\gamma n_0}\boldsymbol{a}_\perp. \tag{2.30}$$

Considering a linearly polarized laser field with a transverse component of the form

$$\boldsymbol{a}_\perp = \frac{\hat{z}}{2}\tilde{a}(r, \zeta, \tau)\exp(iM_p\zeta) + c.c., \tag{2.31}$$

where $M_p = k_z/k_p$, k_z is the wave number of laser pulse in the propagation direction, $k_p = \omega_p/c$ is the plasma wave number, and $\tilde{a}(r, \zeta, \tau)$ presents the envelope profile of the laser pulse. By inserting the following relations

$$\frac{\partial^2 \boldsymbol{a}_\perp}{\partial \zeta \partial \tau} = \frac{\hat{z}}{2}\exp(iM_p\zeta)\cdot\left(iM_p + \frac{\partial}{\partial \zeta}\right)\frac{\partial \tilde{a}}{\partial \tau} + c.c., \tag{2.32}$$

and

$$\frac{\partial^2 \boldsymbol{a}_\perp}{\partial \tau^2} = \frac{\hat{z}}{2} \exp(iM_p\zeta) \cdot \frac{\partial^2 \tilde{a}}{\partial \tau^2} + c.c., \tag{2.33}$$

into Eq. (2.30), it becomes

$$\left(\nabla_\perp^2 + 2iM_p \frac{\partial}{\partial \tau} + 2\frac{\partial^2}{\partial \zeta \partial \tau} - \frac{\partial^2}{\partial \tau^2} - \frac{1}{\gamma}\right)\tilde{a} = \frac{\delta n}{\gamma n_0}\tilde{a}. \tag{2.34}$$

Note that, in study of forward going waves, e.g. plasma wakefield excitation, the term $\partial^2/\partial\tau^2$ is small and can be neglected, but is important for backward going waves, e.g., Raman backward scattering (RBS). Now, assuming that the laser pulse envelope varies very slowly compared to the laser frequency which is typically true especially in the region of laser wakefield acceleration [49, 107, 23, 46], it allows the so-called *paraxial approximation* (PA),

$$\left|2iM_p \frac{\partial \tilde{a}}{\partial \tau}\right| \gg \left|\frac{\partial^2 \tilde{a}}{\partial \zeta \partial \tau}\right|. \tag{2.35}$$

As a result, the dispersive cross term in Eq. (2.34) can be neglected and it arrives at the so-called paraxial wave equation as

$$\left(\nabla_\perp^2 + 2iM_p \frac{\partial}{\partial \tau} - \frac{\partial^2}{\partial \tau^2} - \frac{1}{\gamma}\right)\tilde{a} = \frac{\delta n}{\gamma n_0}\tilde{a}. \tag{2.36}$$

In Eq. (2.36), each ζ slice of the laser pulse propagates at the same velocity c, and the power in each ζ slice is conserved. Solutions to the Eq. (2.36) in vacuum describe laser pulse diffraction. More details on how a laser pulse evolves with PA in a parabolic plasma channel are given in Sec. 3.1 and Sec. 5.1.

Another useful simplification is introduced in the study of laser plasma interaction when a short duration of laser pulse τ_L is considered. Here, if the laser pulse is

sufficiently short to only allow little transition time for a plasma electron, τ_e, [108]

$$\tau_L \ll \tau_e = 2\gamma M_p \left| \frac{n_0}{n} \right| \sim Z_R, \tag{2.37}$$

where $M_p \gg 1$ and Z_R is the Rayleigh length of the laser pulse, ∂/∂_τ derivatives are neglected in Eq. (2.34) that determine the plasma response to the laser pulse. This approximation is the so-called *quasistatic approximation* (QSA) and allows the laser-plasma interaction to be solved analytically for both linear and nonlinear cases. It is seen that a plasma can modify the propagation of laser pulse due to nonlinear and relativistic effects [108, 24, 118]. Motivated by the LPAs or laser fusion experiments, a laser pulse guiding in a fully ionized plasma should be seriously studied to avoid diffraction and to maintain high accelerating gradients for many Rayleigh lengths [46, 55]. The widely considered solutions for laser pulse guiding through an underdense plasma include (relativistic) optical and tailored plasma density channel guiding. Please see more details in Appendix. A.2 and A.3.

2.3 Plasma wakefield excitation

As discussed in Sec. 2.1.2, a plasma can support waves which are actually the density fluctuations at characteristic frequencies corresponding to each species, as described in Eqs. (2.21) and (2.22). Since plasma ions are massive and immobile in comparison with electrons and then the characteristic frequency in Eq. (2.22) is much lower than Eq. (2.21), the plasma electron wave (called plasma wave in following context) is usually studied without consideration of ion acoustic wave, especially in the linear region of laser-plasma accelerations where the strength of the laser pulse a_0 is less than unity, $a_0 < 1$. A straightforward way to drive a plasma wave is to use the nonlinear ponderomotive force exerted by a short laser pulse, which pushes the charged particles away from the region of high field pressure due to the inhomogeneity of

the electromagnetic field [75, 19, 95]. For a laser pulse, the 3D ponderomotive force experienced by an electron is expressed in the linear limit ($a_0 \ll 1$) as [46],

$$\boldsymbol{F}_p = -m_e c^2 \nabla \left(\frac{aa^*}{2} \right), \tag{2.38}$$

and proportional to the gradient in the amplitude of the laser field $\boldsymbol{a}_\perp$, where $|a| = |\boldsymbol{a}_\perp|$ and a^* is the complex conjugate of a. Note that a fully coherent driving laser pulse is not mandatory. Both ions and electrons experience the same ponderomotive force which is independent of the sign of the charge. The ponderomotive force on accelerated electrons should be corrected by $1/\gamma$, where γ is the Lorentz factor of these electrons.

Plasma wave excitation (or plasma wakefield excitation) is a collective plasma behavior and described by Vlasov equation in Eq. (2.17) and Maxwell equation in Eqs. (2.2a)-(2.2d). The solution varies dramatically for different laser pulse strength. As shown in Fig. 2.1, the wakefield and plasma density perturbations are calculated by a numerical method of cold fluid model [107]. When the laser pulse is weak, $a_0 < 1$, the plasma wave is a simple sinusoidal oscillation. However, once the laser pulse becomes much intense, $a_0 > 1$, for example $a_0 = 2$, the electron density is periodically peaked and forms a series of "vacuum" regions of plasma electrons which is the so-called blow-out region. As a result, the electric field is significantly sharpened. Unfortunately, a fully general solution for the plasma wave excitation does not exist so far. The possible solutions only exist in cases of 3D linear ($a_0 \ll 1$) and 1D nonlinear ($a_0 > 1$) regime. Otherwise, the numerical method is required. Several possible numerical models now are available including nonlinear quasistatic fluid models [107, 49] or particle simulation models [93, 28, 120]. In the following, available analytical theories of 3D linear and 1D nonlinear wakefield are discussed to laying a base for further work in this thesis by using the source-dependent-expansion (SDE)

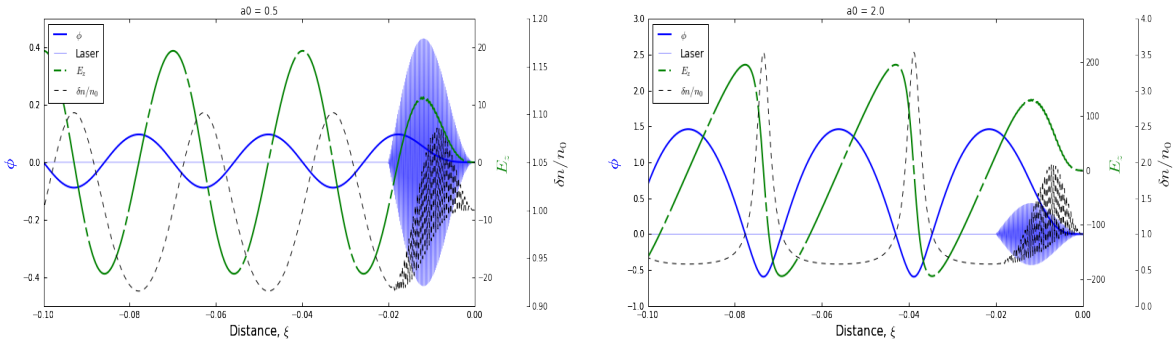

Figure 2.1: Wakefield excitation by a single Gaussian laser pulse of different strengths, left: $a_0 = 0.5$ and right: $a_0 = 2.0$ (indicated by blue spot on the right in each plot). Blue solid line presents the wakefield potential ϕ; Green dashed line presents the longitudinal electric field E_z; black dashed line presents the plasma density perturbation.

technique [111, 48]. Of course, there also are the other possible methods, for example, variational [6, 26, 45] and moment methods [77].

2.3.1 Linear plasma wave

For a weak laser pulse, $a_0 \ll 1$, the plasma electron fluid can be assumed to be cold where the relativistic gamma factor of plasma fluid in Eq. (A.12) is approximately equal to unity, $\gamma \simeq 1 + O(a_0^2)$. Therefore, the plasma wave excitation can be described by the cold fluid equations of an electron including the linearized equation of motion, continuity equation and the cold Poisson equation for nonrelativistic background plasma. In the linear limit $a_0 \ll 1$, the 3D plasma wave is described by [46]

$$\left(\frac{\partial^2}{\partial\zeta^2} + 1\right)\frac{\delta n}{n_0} = \nabla^2\left(\frac{aa^*}{2}\right), \tag{2.39}$$

and

$$\left(\frac{\partial^2}{\partial\zeta^2} + 1\right)\phi = \frac{aa^*}{2}, \tag{2.40}$$

where $\delta n/n_0 = (n-n_0)/n_0$ is the normalized plasma density perturbation and ϕ is the electrostatic wake. The solutions for Eq. (2.39) and Eq. (2.40) are given respectively by

$$\frac{\delta n}{n_0} = \int_{-\infty}^{\zeta} d\zeta' \sin(\zeta - \zeta') \nabla^2 \left(\frac{a(\zeta') a^*(\zeta')}{2} \right), \tag{2.41}$$

and

$$\phi = \int_{-\infty}^{\zeta} d\zeta' \sin(\zeta - \zeta') \frac{a(\zeta') a^*(\zeta')}{2}. \tag{2.42}$$

The electric field is calculated by $\boldsymbol{E} = -\nabla\phi \sim O(a_0^2)$. The peak field amplitude is estimated from Gauss's law in Eq. (2.2a) by assuming that all plasma electrons are oscillating with the same frequency ω_p, and given by

$$E_0 = \frac{m_e c \omega_p}{e}, \tag{2.43}$$

which is also known as the cold non-relativistic wave breaking field [39]. The magnetic field can be obtained by applying a higher-order perturbation expansion of a in the fluid equations. With QSA, $\boldsymbol{B}$ is scaled as $\sim O(a_0^4)$ and is usually neglected [59]. It is seen from Eqs. (2.41) and (2.42) that the excitation of wakefield is most efficient if the duration of laser pulse is scaled in order of plasma wavelength $\lambda_p = \omega_p/c$. For example, by considering a linearly polarized Gaussian laser pulse in Eq. (2.31) propagating in the initially uniform plasma, the electric field is given as

$$E_z = a_0^2 \, C \, \exp\left(-\frac{2\mathbf{r}^2}{w_0^2} \right) \cos\zeta, \tag{2.44}$$

$$\mathbf{E_r} = -\frac{4 a_0^2 \, C}{w_0^2} \mathbf{r} \exp\left(-\frac{2\mathbf{r}^2}{w_0^2} \right) \sin\zeta, \tag{2.45}$$

where w_0 is the initial laser spot size. Coefficient C defined in Eq. (3.19) in Chapter 3 depends on the laser pulse duration τ_L'. It is maximized $C_{\max} \simeq 0.38$ at $c\tau_L' = \lambda_p/\pi$. E_z is longitudinal electric field. The transverse electric field $\boldsymbol{E}_r$ is zero on axis.

An electron beam can experience both accelerating and focusing force in the phase $-\pi < \zeta < -\pi/2$.

2.3.2 Nonlinear plasma wave

The linear theory discussed in Sec. 2.3.1 does not work anymore once a more intense laser pulse is considered, for example $a_0 > 1$, but the 1D self-consistent model is still possible with the QSA assumed. Using the Coulomb gauge, the fully nonlinear wakefield equations are given by [108]

$$\left(2\frac{\partial^2}{\partial\zeta\partial\tau} - \frac{\partial^2}{\partial\tau^2}\right)\boldsymbol{a} = \frac{\boldsymbol{a}}{1+\phi}, \tag{2.46}$$

and

$$\frac{\partial^2\phi}{\partial\zeta^2} = \frac{1}{2}\left[\frac{1+a^2}{(1+\phi)^2} - 1\right], \tag{2.47}$$

where the cold plasma quantities of density n, the normalized longitudinal plasma velocity β_z and the relativistic mass factor γ are

$$\frac{n}{n_0} = 1 + \frac{1}{2}\left[\frac{1+a^2}{(1+\phi)^2} - 1\right], \tag{2.48}$$

$$\gamma = \frac{1+a^2+(1+\phi)^2}{2(1+\phi)}, \tag{2.49}$$

and

$$\beta_z = \frac{1+a^2-(1+\phi)^2}{1+a^2+(1+\phi)^2}. \tag{2.50}$$

The maximum amplitude of a nonlinear plasma wave is estimated as [50]

$$E_{\mathrm{WB}} = \sqrt{2(\gamma_p - 1)}E_0, \tag{2.51}$$

where E_0 is the cold non-relativistic wave breaking field in Eq. (2.43) and $\gamma_p = (1 - v_p^2/c^2)^{-1/2}$ associated with the phase velocity v_p of the plasma wave.

The plasma wave breaks when the maximum electric field exceeds the wave-breaking threshold $E_{\rm WB}$, which can be achieved by increasing the strength of laser pulse a_0, for example, $a_0 = 10$ and $n_0 = 10^{19}$ cm^{-3} [94]. A prominent feature of wave-breaking is that it provides a larger field volume and a higher accelerating gradient, and thus promises the efficient trapping and acceleration of electrons. Such an scheme is the so-called "plasma bubble accelerator".

2.3.3 Electron injection and trapping

An electron can be injected/trapped inside a plasma wave of the amplitude [104]

$$E_m = \gamma_p \sqrt{2\bigg(1 + \phi_{\rm min} - \gamma_\perp + \beta_p(\beta_p\gamma_\perp - [(1+\phi_{\rm min})^2 - \gamma_\perp^2/\gamma_p^2]^{1/2})\bigg)}, \tag{2.52}$$

if the momentum of the electron exceeds

$$u_t = \gamma_p\beta_p(\gamma_\perp - \gamma_p\phi_{\rm min}) - \gamma_p[(\gamma_\perp - \gamma_p\phi_{\rm min})^2 - 1]^{1/2}, \tag{2.53}$$

where $\phi_{\rm min}$ is the minima of the plasma wave potential and $\gamma_\perp = \sqrt{1 + a^2/2 + u_{\perp 0}^2}$ for a linearly polarized laser pulse and the electron with an initial transverse momentum $u_{\perp 0}$.

Generally, the controlled synchronised injection/trapping of electrons into a wakefield can occur through internal (self-injection) and external schemes. The internal injection is trapping of the electrons from the background plasma in a proper phase and is common in many experiments. Several self-injection schemes have been proposed in recent years including wave-breaking injection [87], tunnel-ionized injection [88], down-ramp injection [61], optical injection [48, 54]. However, several difficulties are

encountered, such as, poor stability and large shot-to-shot fluctuations, which leads to serious electron beam diffraction and large energy spread.

External electron injection schemes are widely considered in the linear wakefield regime and promise a control over the parameters of the injected electron beam, such as injection position and angle, energy spread and emittance. Typically, there are two categories for external injection of the electrons: behind [44] and in front of the laser pulse [7, 70, 69]. By applying a chirped laser pulse, the in-front-injection schemes give good control over the trapping process of injecting the electron beam into an suitable position with right initial momentum [51], which is one of the basic requirements for our current work of plasma channel undulator discussed in Chapter 3-6. To be clear, we only consider the external injection throughout this thesis for PIC simulations, since the theoretical work mainly focuses on the linear regime of plasma wakefield.

2.3.4 Dephasing and phase lock

The laser group velocity approximately equals to the phase velocity of wakefield [46]. The phase velocity of wakefield can be given as

$$\beta_{ph} = \sqrt{1 - \frac{1}{M_p^2} - \frac{4}{M_p^2 w_0^2}}, \tag{2.54}$$

and is smaller than the velocity of an injected electron which is close to the speed of light. This difference leads to the phase slippage or dephasing of the injected electron inside the plasma wakefield. As a result, an injected electron will slip out from the initial injected phase. That is detrimental for the work presented in this thesis.

Inside a plasma wakefield, the dephasing length is given with the maximum phase slippage π by [46]

$$L_D = \frac{\pi}{1 - \beta_{ph}}. \tag{2.55}$$

In the case of low plasma density and tightly focused electron beam considered, the dephasing effect could be neglected for a short propagation distance $L_{\text{propagation}}$ by comparing to the dephasing length, $L_D \gg L_{\text{propagation}}$ and then $u_z \approx u_{z0}$ in the phase $\zeta = -3\pi/2$. Otherwise, the special technologies should be considered to eliminate this effect. For example, in a plasma channel undulator as discussed in Chapter 3 with the on-axis density $1 \times 10^{18}\text{cm}^{-3}$ or $M_p = 33$ with respect to a laser pulse of 1μm wavelength and initially matched laser spot size $r'_m = 7\mu$m, the dephasing length is $L_d \simeq 2000$ and the undulator oscillation wavelength is $\lambda_u = 190$. For a case of 30 oscillation periods where the propagation distance is $L_{\text{propagation}} = 5700$, the longitudinal plasma density ramp should be considered to lock the electron around the initial phase by [96],

$$\frac{d\tilde{n}}{dz} = \frac{\tilde{n}^2}{|\xi_0|}\left(\frac{2}{M_p w_0^2} + \frac{M_p}{2}\tilde{n}^2\right), \tag{2.56}$$

where $\tilde{n} = \sqrt{n_0(z)/n_c}$ and $M_p = k_0/k_p$, k_0 is the wavenumber of laser pulse.

2.4 Radiation from moving charged particles

Radiation emitted by a single charged particle q undergoing an arbitrary motion can be calculated though the Lienard-Wiechert potentials [63]. Please see more details for the general derivation in Appendix. A.4. For a single relativistic electron undergoing the transverse sinusoidal oscillation which is usually the case in a conventional insertion device, e.g. undulator or wiggler, the short-wave radiation is generated with well-controlled parameters. The on-axis radiation intensity of m-th harmonic for the

sinusoidal oscillation can be calculated by using Eq. (A.37) as [103]

$$\frac{d^2 I_m}{d\omega d\Omega} = \frac{e^2 \gamma_0^2 a_u^2}{c(1 + a_u^2/2)^2} \cdot m^2 \cdot S_m(\omega) \cdot |JJ_m|^2, \quad \text{(linear)} \tag{2.57}$$

$$\frac{d^2 I_m}{d\omega d\Omega} = \frac{2e^2 \gamma_0^2 a_u^2}{c(1 + a_u^2)^2} \cdot m^2 \cdot S_m(\omega), \quad \text{(circular)} \tag{2.58}$$

where the emission shape function $S_m(\omega)$ for m-th harmonic is given by

$$S_m(\omega) = \frac{\sin^2\left(\pi N_u \frac{\omega - \omega_m}{\omega_m}\right)}{\sin^2\left(\pi \frac{\omega - \omega_m}{\omega_m}\right)}, \tag{2.59}$$

and

$$JJ_m = J_{\frac{m-1}{2}}(m\chi) - J_{\frac{m+1}{2}}(m\chi), \tag{2.60}$$

where N_u is the oscillation number and J_n denotes the Bessel function of the n-th order, $\chi = a_u^2/[4(1 + a_u^2/2)]$. The important parameter defined here is the so-called undulator strength a_u which is actually the normalized transverse momentum of the electron in the case of a periodic transverse sinusoidal oscillation. For $a_u < 1$, it is said to be in the undulator region where the radiation is confined in a small forward cone with respective to the propagation direction and the energy is mainly contained in the fundamental harmonic as shown in the first plot of Fig. 2.2 where $a_u = 0.8$. Such radiation is usually characterized by a central frequency defined in Eqs. (2.64) and (2.65) as below. The term 'wiggler' is used instead of 'undulator', usually for undulators with a small number of periods, but large $a_u \gg 1$. Then, the radiation spectrum becomes similar to the synchrotron radiation spectrum as shown in the second and third plots of Fig. (2.2) where $a_u = 2$ and $a_u = 3$ respectively. The fields of radiation from different points do not interfere in some sense [121]. Such radiation is also characterized by a critical frequency same as Eq. (A.39). Here, a

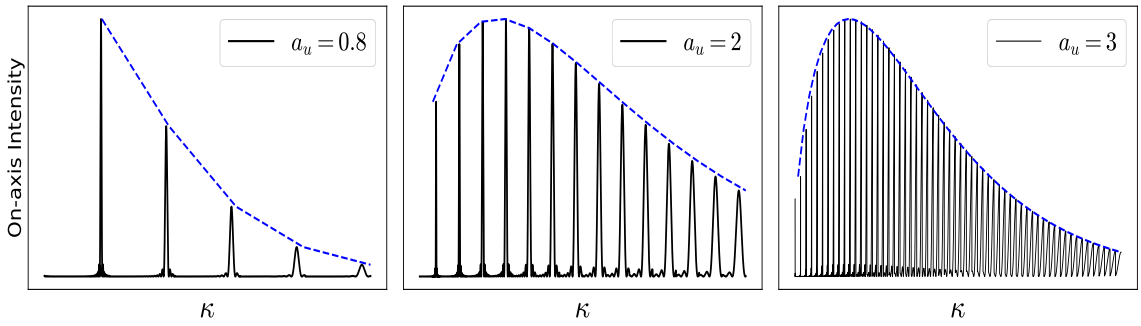

Figure 2.2: Radition spectrum for different undulator strength: $a_u = 0.8$, 2, 3.

defined variable κ presents the normalized frequency of emitted photon as

$$\kappa = \frac{\omega}{2\gamma_0^2 \omega_u}. \tag{2.61}$$

Using Eq. (2.59) one finds that the natural bandwidth of m-th harmonic is $\Delta\omega/\omega = 1/(mN_u)$. The fundamental radiation spectrum is shown in Fig. 2.3 where the upper-plot is calculated with the 80 oscillation periods and lower-plot is with 10 periods. The on-axis radiation intensity is shown in Fig. 2.4 with the numerical and analytical results in Eq. (2.57) for linearly polarized case. It is seen that the spectrum is much narrower if more oscillation periods are implemented. A collimation angle of the emitted radiation is then required up to

$$\theta_m = \frac{1}{\gamma_0}\sqrt{\frac{1 + a_u^2/2}{mN_u}}, \quad \text{(linear)} \tag{2.62}$$

$$\theta_m = \frac{1}{\gamma_0}\sqrt{\frac{1 + a_u^2}{mN_u}}, \quad \text{(circular)} \tag{2.63}$$

to achieve such natural bandwidth, as shown the dashed horizontal white lines in Fig. (2.3) for the fundamental harmonic. The central frequency for fundamental

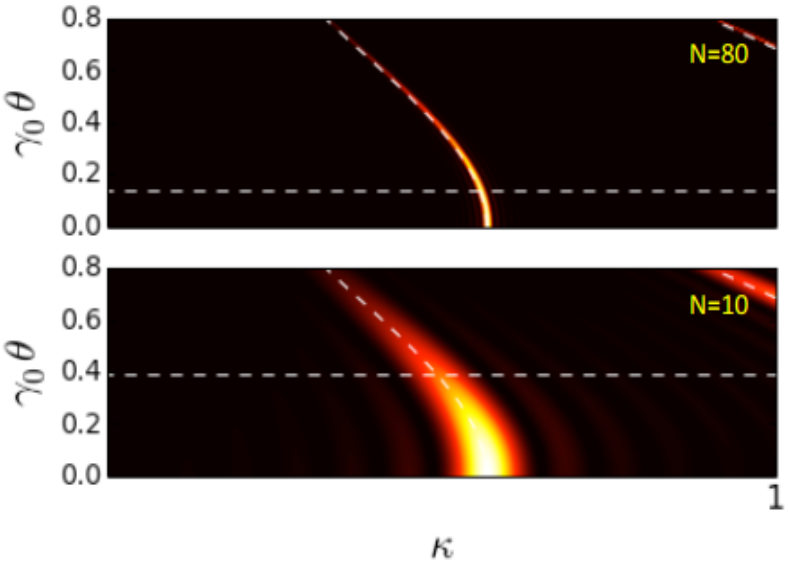

Figure 2.3: VDSR [99] simulation result of the radiation spectrum from an undulator oscillation. Upper-plot is calculated with the 80 oscillation periods; lower-plot is calculated with 10 periods, for linear polarized case. The horizontal dashed white lines show the position collimation angle.

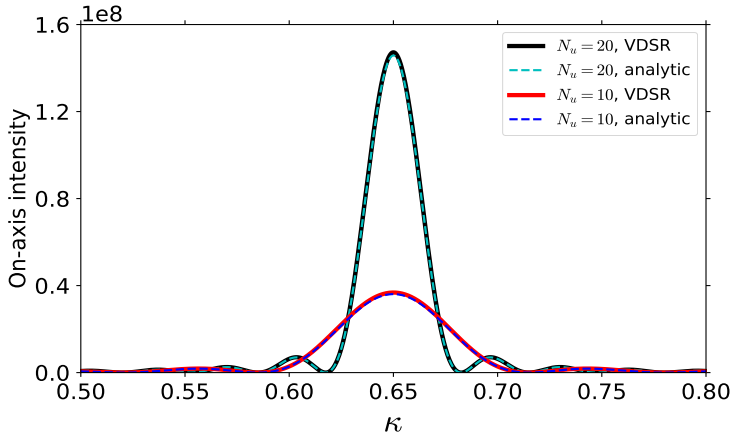

Figure 2.4: The analytical and numerical results of on-axis radiation intensity for different oscillation periods in the linear polarized case.

$(m = 1)$ harmonic is given as

$$\omega_1 = \frac{2\gamma_0^2 \omega_u}{1 + a_u^2/2}, \quad \text{(linear)} \tag{2.64}$$

$$\omega_1 = \frac{2\gamma_0^2 \omega_u}{1 + a_u^2}, \quad \text{(circular)} \tag{2.65}$$

where ω_u is the undulator oscillation frequency of the electron. Thus, the central frequency for m-th harmonic is given by $\omega_m = m\omega_1$. The number of photons inside the harmonics can be calculated from Eqs. (2.57) and (2.58). For the fundamental harmonic in the range of total azimuth angle 2π and bandwidth $\Delta\omega$, the energy intensity in Eq. (A.37) can be estimated as

$$\frac{d^2 I_1}{d\Omega d\omega} = (2\pi\Delta\omega)^{-1} \frac{dI_1}{\theta d\theta}, \tag{2.66}$$

and together with the on-axis radiation intensity in Eqs. (2.57) and (2.58) for the fundamental harmonic and collimation angle in Eqs. (2.62) and (2.63), one could find the number of photons in the fundamental natural bandwidth,

$$N_{ph} = \frac{dI_1}{\hbar\omega_1} = \pi\alpha \frac{a_u^2}{1 + \frac{a_u^2}{2}} \cdot |JJ|^2, \quad \text{(linear)} \tag{2.67}$$

$$N_{ph} = \frac{dI_1}{\hbar\omega_1} = 2\pi\alpha \frac{a_u^2}{1 + a_u^2}, \quad \text{(circular)} \tag{2.68}$$

where $\alpha = e^2/(\hbar c)$ is the fine structure constant. As shown in Fig. 2.5, the circularly polarized oscillation produces two times more photons than the linear case for the same a_u.

The radiation spectrum from an electron beam is broadened in comparison with the case of an single electron. The main contributions considered in the thesis include the spread of beam energy $\Delta\gamma$, undulator strength Δa_u, and transverse angular of

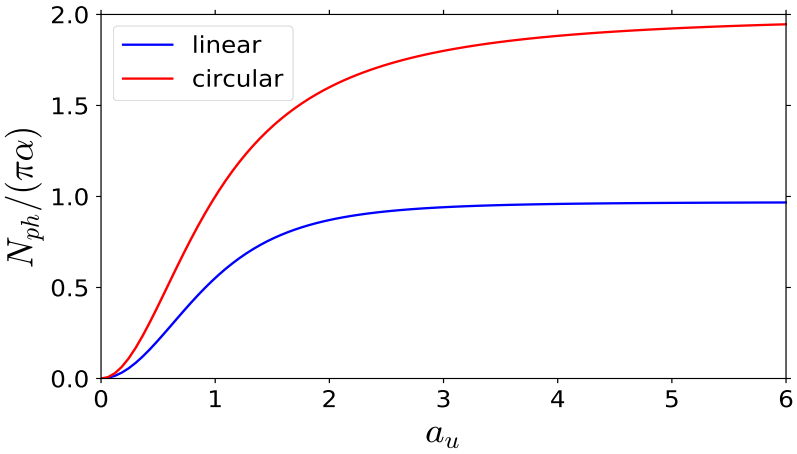

Figure 2.5: Normalized number of photons in the fundamental harmonic.

the electron beam $\Delta\theta$ [102, 100], and can be expressed as

$$\left[\frac{\Delta\omega}{\omega}\right]_{FWHM} \approx \sqrt{\left(\frac{1}{N_u}\right)^2 + \left(\frac{2\Delta\gamma}{\gamma_0}\right)^2 + \left(\frac{\Delta a_u}{4\gamma_0}\right)^2 + \left(\frac{\gamma_0\Delta\theta}{4}\right)^4}. \tag{2.69}$$

Additional spectral broadening may also appear due to the other errors, e.g injection errors, but is neglected in this thesis.

Chapter 3

X-ray radiation from plasma-based undulator

An undulator field may be generated by the plasma wakefield excited by an intense laser pulse undergoing centroid oscillation in a plasma channel. In this chapter, the basic theory of the plasma channel undulator is presented. In Sec. 3.1, the theory of guiding a Gaussian laser pulse in a parabolic plasma channel is described. The undulator field generated by the laser pulse with centroid oscillation is presented in Sec. 3.2. The dynamics of an electron (as well as an electron beam) inside such a wakefield are discussed in Sec. 3.3 and 3.4. The narrow X-ray radiation spectrum is calculated, and the possible controllability and optimisation is then provided in Sec. 3.5. In Sec. 3.6, the conclusion of this chapter is provided.

3.1 Laser pulse propagation in a parabolic plasma channel

A laser pulse guiding inside the parabolic plasma channels [46, 55], for example created by capillary discharges, is routinely performed in LPA experiments [80, 58] in order

to avoid the laser pulse diffraction and, thus, maintain a high accelerating gradient (1GeV/cm) for several centimeters. Consider a plasma channel with the transverse electron density profile given by

$$n(r) = n_0\left(1 + \frac{\Delta n}{n_0}\frac{r^2}{w_0^2}\right), \tag{3.1}$$

where $r = \sqrt{x^2 + y^2}$ is the radial coordinate, x and y are the transverse coordinates, n_0 is the on-axis plasma density, w_0 is the laser spot size at waist, and Δn is the channel depth. By considering a short laser pulse, with the power satisfying $P < P_c$, where $P_c[GW] \simeq 17M_p^2$ is the so-called the critical power and $M_p = k_l/k_p$, the envelope $\tilde{a}_\perp(\tau, r)$ can be assumed to vary very slowly. The normalized vector potential of the laser pulse can be expressed as

$$a_\perp(\tau, r, \zeta) = \frac{eA_\perp}{m_e c^2} = \frac{1}{2}\tilde{a}_\perp(\tau, r)g(\zeta)e^{iM_p\zeta} + c.c., \tag{3.2}$$

where $A_\perp$ is the laser pulse vector potential in Gaussian units, $g(\zeta)$ is the laser pulse temporal envelope (normalized to 1), and satisfies QSA, $|\partial_\zeta \tilde{a}_\perp| \ll |M_p\tilde{a}_\perp|$. The equation for laser envelope reads from Eq. (2.34)

$$\left(\nabla_\perp^2 + 2\frac{\partial^2}{\partial\zeta\partial\tau} + 2iM_p\frac{\partial}{\partial\tau} - \frac{\partial^2}{\partial\tau^2}\right)\tilde{a}_\perp = \left(1 + \frac{r^2}{R^2}\right)\tilde{a}_\perp, \tag{3.3}$$

where $R = r_m^2/2$ is the dimensionless channel radius and $r_m^2 = k_p^2/(\pi r_e^{'}\Delta n)$ with $r_e^{'}$ is the classical electron radius in CGS unit.

With PA for the short laser pulse in Eq. (2.35), dynamics of the pulse envelope $\tilde{a}_\perp$ is described by the simple Schrödinger wave equation for a harmonic oscillator

$$i\frac{\partial\tilde{a}_\perp}{\partial\tau} = \left[\frac{\hat{p}^2}{2M_p} + V(r)\right]\tilde{a}_\perp = \hat{H}\tilde{a}_\perp, \tag{3.4}$$

where $\hat{p} = -i\nabla_{\perp}$ is the momentum operator and the potential is

$$V(r) = \left(\frac{1}{2M_P} + \frac{M_p\Omega^2 r^2}{2}\right), \tag{3.5}$$

with the eigen frequency

$$\Omega = (M_p R)^{-1}. \tag{3.6}$$

From Ehrenfest's theorem, the centroid position of laser pulse in x-direction is given in the form of harmonic oscillator (please see more details in Appendix. B.1)

$$\frac{d^2\langle x\rangle}{d\tau^2} + \Omega^2\langle x\rangle = 0, \tag{3.7}$$

where $\langle x\rangle$ is the expectation value of position operator. The equation is the same in y-direction due to the transversely geometric symmetry. The solution for Eq. (3.7) is then given as

$$\langle x\rangle = \langle x\rangle_0 \cos\Omega\tau + \frac{\langle\hat{p}_x\rangle_0}{M_p\Omega}\sin\Omega\tau. \tag{3.8}$$

Here, subscript 0 denotes the expectation value of an operator taken at the initial time, $\tau = 0$. Therefore, $\langle x\rangle_0$ is the initial centroid displacement with respect to the channel axis, and $\langle\hat{p}_x\rangle_0$ is the initial expectation value of the momentum operator $\hat{p}_x = -i\partial_x$, which is related to the angle of injection of the laser pulse into the channel. One can see that the center of the laser pulse oscillates with the characteristic frequency Ω. The evolution of the dispersion $\sigma_x = \langle x^2\rangle - \langle x\rangle^2$ of laser pulse is connected to the

transverse laser spot size and can also be found from Ehrenfest's theorem as

$$\begin{aligned}\sigma_x =&\frac{\sigma_{x0}}{2} + \frac{\sigma_{p_x,0}}{2M_p^2\Omega^2} + \left(\frac{\sigma_{x0}}{2} - \frac{\sigma_{p_x,0}}{2M_p^2\Omega^2}\right)\cos 2\Omega\tau + \\ &\frac{1}{M_p\Omega}\left(\frac{\langle x\hat{p}_x + \hat{p}_x x\rangle_0}{2} - \langle x\rangle_0 \langle \hat{p}_x\rangle_0\right)\sin 2\Omega\tau,\end{aligned} \tag{3.9}$$

where the dispersion of the operator $\hat{p}_x$ is denoted as $\sigma_{p_x,0} = \langle \hat{p}_x^2\rangle_0 - \langle \hat{p}_x\rangle_0^2$. Please see more details of the derivation in Appendix. B.1. It is seen that dynamics of the laser pulse in the plasma channel can be described by Eqs. (3.7) and (3.9) together with initial conditions.

For example, considering a spatially Gaussian laser pulse with initial transverse displacement $\langle x\rangle_0 = x_0$ and injection angle θ_{x0},

$$\tilde{a}_\perp(\tau = 0, x) = a_0 \exp\left(-\frac{(x - x_0)^2}{w_0^2} + iM_p\theta_{x0}x\right), \tag{3.10}$$

where w_0 is the initial laser spot size. The transverse laser spot size in Eq. (3.9) then becomes

$$\sigma_x = \frac{w_0^2}{8} + \frac{R^2}{2w_0^2} + \left(\frac{w_0^2}{8} - \frac{R^2}{2w_0^2}\right)\cos 2\Omega\tau. \tag{3.11}$$

As seen from Eq. (3.11), the laser spot size $w_x = 2\sqrt{\sigma_x}$ can keep constant along the propagation if the initial laser spot size is matched to the transverse plasma channel dimension as $w_0 = r_m$. The envelope of the laser pulse keeps constant for a quit long propagation distance in the matched case (solid orange line) as shown in Fig. 3.1.

The frequency of centroid oscillation of the laser pulse in Eq. (3.7) becomes $\Omega = 1/(M_pR) = 1/Z_R$, where $Z_R = M_pw_0^2/2$ is the normalized initial Rayleigh length of the laser pulse. Considering a matched Gaussian laser pulse of wavelength $\lambda_l = 1.0\ \mu$m with initial transverse off-set $\langle x\rangle_0 = 0.19$ in x-direction and a parabolic plasma channel of dimension $r_m = 1.3$, the on-axis electron density $n_0 = 1.0 \times 10^{18}$ cm^{-3}

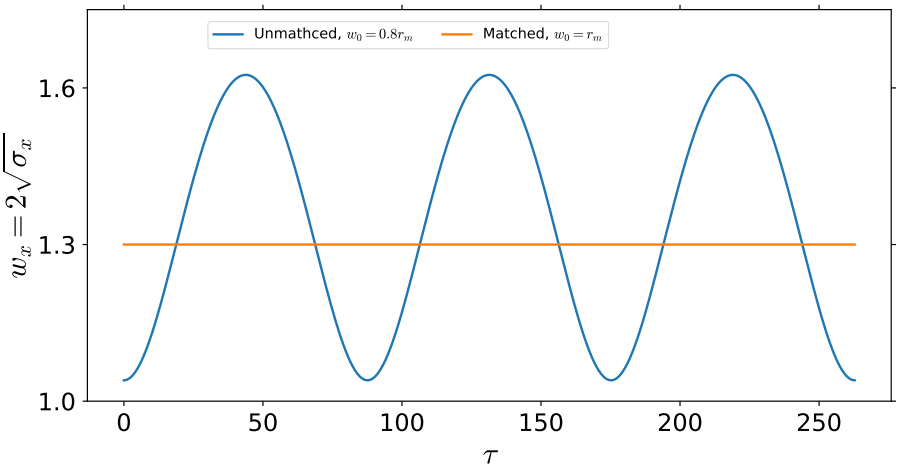

Figure 3.1: The evolution of laser pulse spot size in a plasma channel for the matched and unmatched cases.

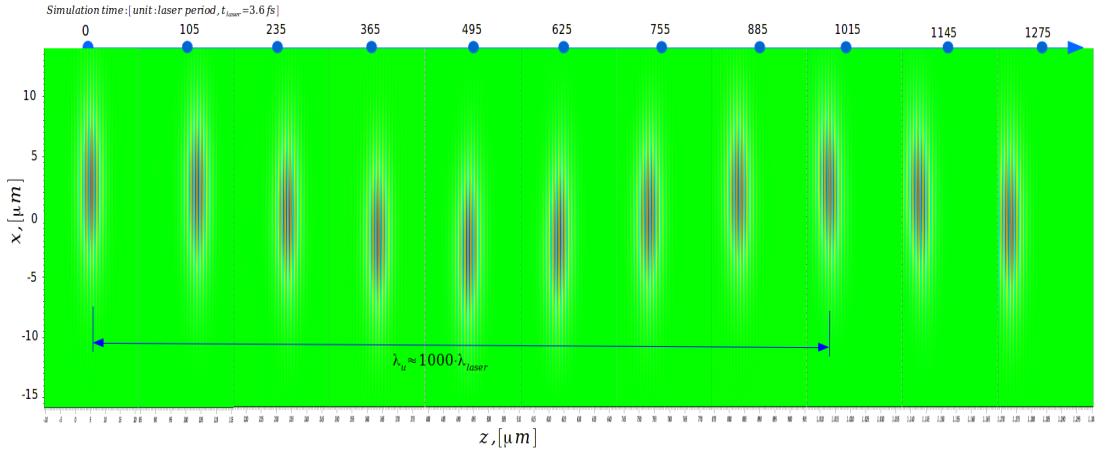

Figure 3.2: The centroid oscillation of a matched laser pulse in a parabolic plasma channel obtained from a PIC simulation by PIConGPU [27].

gives $M_p \simeq 33$. The evolution of laser spot size and centroid oscillation is shown in Fig. 3.2 where the envelope keeps constant and the center oscillates around the axis with the oscillation wavelength $\lambda_u = 2\pi Z_R \simeq 1000\lambda_l$.

By introducing an initial injection angle, the center of laser pulse can also oscillate in the same way. The dynamics of laser pulse in y-direction can be treated similarly as that in x-direction. Therefore, if the initial displacement and the injection angle are introduced both in x- and y-direction as $\langle x \rangle_0 = x_0, \langle \theta_x \rangle = 0$ and $\langle y \rangle_0 = 0, \langle \theta_y \rangle = \Omega x_0$,

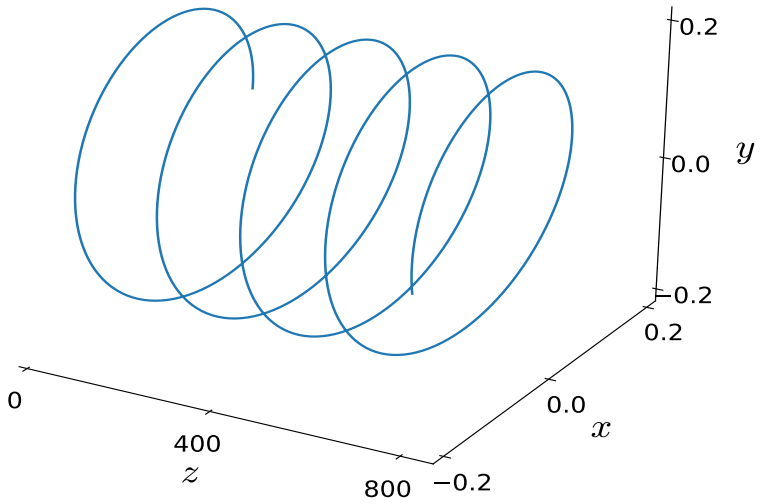

Figure 3.3: The centroid oscillation of a matched laser pulse in 3D case. The laser pulse undergoes a helical motion.

the center of laser pulse undergoes a helical motion around the longitudinal axis. Of course, symmetrically, the case with transverse displacement $\langle y \rangle_0 = y_0$ in y-direction and injection angle $\langle \theta_x \rangle = \Omega y_0$ in x-direction also works. For example, by considering the following injection conditions,

x-direction:

$$\langle x \rangle_0 = 0.19, \ \langle \theta_x \rangle = 0, \tag{3.12}$$

y-direction:

$$\langle y \rangle_0 = 0, \ \langle \theta_y \rangle = \Omega \langle x \rangle_0 = 0.0068, \tag{3.13}$$

the centroid oscillation of the laser pulse in the 3D space is shown in Fig. 3.3.

A more elegant way can be used to describe the dynamics of the laser pulse center in

3D as

$$\mathbf{r}_c(\tau) = \frac{1}{2} r_{c0} \boldsymbol{\epsilon} e^{i\Omega\tau+\phi} + c.c., \tag{3.14}$$

where $\boldsymbol{\epsilon}$ is a defined complex parameter describing the polarization of centroid oscillation of the laser pulse. For example, for the circularly polarized oscillation, $\boldsymbol{\epsilon} = (1, \pm i)$ and $\boldsymbol{\epsilon} = (1, 0)$ for linear case. $r_{c0} = \sqrt{x_{c0}^2 + y_{c0}^2}$ is the radial injection off-set with

$$x_{c0} = \sqrt{\langle x \rangle_0^2 + \left(\frac{\langle \hat{p}_x \rangle_0}{M_p \Omega} \right)^2}, \tag{3.15}$$

and

$$y_{c0} = \sqrt{\langle y \rangle_0^2 + \left(\frac{\langle \hat{p}_y \rangle_0}{M_p \Omega} \right)^2}. \tag{3.16}$$

Such laser pulse can excite a plasma wakefield oscillating with the same frequency which will be discussed in the following Sec. 3.2.

3.2 Undulator field generation

It is straightforward to calculate the plasma wakefield excited by the laser pulse given in Eq. (3.2). In the linear 3D region where $a_0 < 1$, with the assumptions: 1) broad plasma channel ($r_m \gg 1$) where the plasma density can be approximately treated as initially uniform around the propagation axis; 2) effect of channel curvature on the wakefield only has a little effect as discussed below and then is neglected; 3) the laser pulse propagates near the speed of light, the plasma wave could be examined by using the cold fluid equations in Eqs. (2.40) and (2.39). The solution for normalized scalar potential of the wakefield is given in Eq. (2.42) which depends on the intensity structure of the laser pulse [46]. With the linearly polarized laser pulse of spatial

Gaussian envelope in Eq. (3.10), the intensity can be written as

$$I = \tilde{a}_\perp \tilde{a}_\perp^* = a_0 \exp\left(-\frac{2(\mathbf{r} - \mathbf{r}_c(\tau))^2}{r_m^2}\right) g^2(\zeta), \tag{3.17}$$

where $\mathbf{r} = (x, y)$ are the transverse coordinates and $\mathbf{r}_c(\tau)) = (x_c, y_c)$ are the transverse center of laser pulse given in Eq. (3.14). $g(\zeta)$ is the temporal profile of the laser pulse. Considering a Gaussian temporal profile $g(\zeta) = \exp(-\zeta^2/w_z^2)$, the solution is then given by

$$\phi(\zeta, x, y) = -\frac{a_0^2}{4}\sqrt{\frac{\pi}{2}}\, w_z \exp\left(-\frac{w_z^2}{8}\right) \exp\left(-\frac{2(\mathbf{r} - \mathbf{r}_c(\tau))^2}{r_m^2}\right) \sin\zeta, \tag{3.18}$$

where w_z is the pulse length and

$$C = \sqrt{\frac{\pi}{2}}\frac{w_z}{4} \exp\left(-\frac{w_z^2}{8}\right). \tag{3.19}$$

It is seen that the amplitude of the wakefield reaches the maximum at $w_z = 2$ where $C \simeq 0.38$ for the linearly polarized laser pulse, and $C \simeq 0.76$ for the circular case. Magnetic field is neglected in the linear case as discussed in Sec. 2.3.1, and the electric fields are given by $\mathbf{E}(\zeta, x, y) = -\nabla\phi(\zeta, x, y)$. Assuming that k_p is constant for an ultra-short laser pulse with QSA [46], the wakefield is given by

$$E_z = a_0^2\, C \exp\left(-\frac{2\left(\mathbf{r} - \mathbf{r_c}(\tau)\right)^2}{r_m^2}\right) \cos\zeta, \tag{3.20}$$

$$\mathbf{E_r} = -\frac{4a_0^2\, C}{r_m^2}\left(\mathbf{r} - \mathbf{r_c}(\tau)\right) \exp\left(-\frac{2\left(\mathbf{r} - \mathbf{r_c}(\tau)\right)^2}{r_m^2}\right) \sin\zeta, \tag{3.21}$$

where $\mathbf{E_r} = (E_x, E_y)$ presents the transverse field components. The transverse field $\mathbf{E_r}$ in Eq. (3.21) creates the undulator field for the injected electrons. For an electron, E_z is the longitudinal electric field of acceleration in the phase $-(2n + 3/2)\pi < \zeta < -(2n + 1/2)\pi$ and of deceleration in the phase $-(2n + 1/2)\pi < \zeta < (2n - 1/2)\pi$, n is

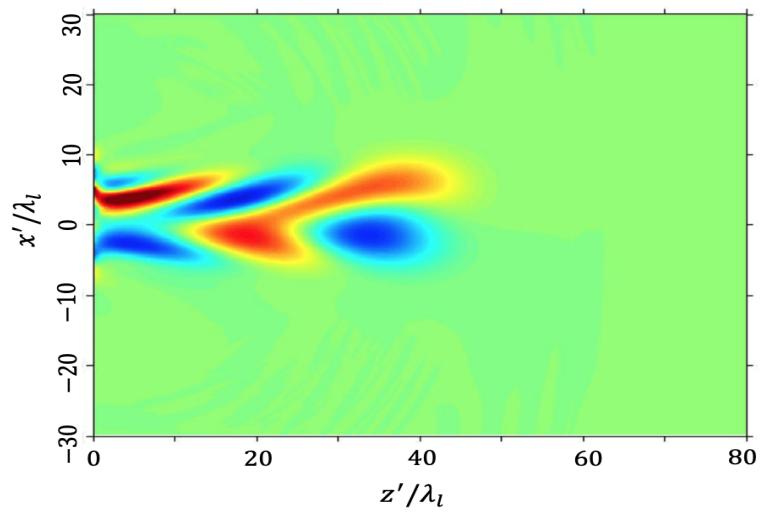

Figure 3.4: Transverse wakefield E_y excited by a laser pulse injected off-axis into a plasma channel.

the non-negative integer. At the point $\zeta = -(2n+1/2)\pi$, there is not ac/deceleration but only the transverse field. It is seen that the centroid oscillation of the laser pulse $r_c(\tau)$ introduces the oscillation of wakefield. For a wide laser pulse by comparing to the amplitude of centroid oscillation $r_m \gg |\mathbf{r} - \mathbf{r_c}(\tau)|$, the exp-terms in Eqs. (3.20) and (3.21) can be approximated as $\exp\left(-2\left(\mathbf{r} - \mathbf{r_c}(\tau)\right)^2/r_m^2\right) \simeq 1$. As a result, the transverse fields become linear. As shown in Fig. 3.4, the transverse wakefield E_x in xz-plane is obtained from PIC simulation after the laser pulse propagating some distance in the plasma channel. It shows that the oscillation of this wakefield can be well controlled by manipulating the dynamics of a laser pulse, and then generates a flexible undulator field to drive the harmonic oscillation of the injected electrons as discussed in Sec. 3.3.

3.3 Dynamics of a single electron

Dynamics of a charged particle in EM field is dominated by the Lorentz force equation in Eq. (2.1). By neglecting the magnetic field and using the electric field in Eqs. (3.20)

and (3.21), the equation of motion for a single electron can be expressed as

$$\frac{d^2\mathbf{r}_\perp}{d\tau^2} - \frac{E_z}{\gamma(\tau)}\frac{d\mathbf{r}_\perp}{d\tau} + \frac{\mathbf{E}_\mathbf{r}}{\gamma(\tau)} = 0, \tag{3.22}$$

where $\mathbf{r}_\perp = (x, y)$ and the Lorentz factor of the electron depends on time due to acceleration as

$$\gamma(\tau) = \gamma_0 - \int_{\tau_0}^{\tau} E_z(\tau')d\tau', \tag{3.23}$$

and $\gamma_0 = \gamma(\tau = 0)$ presents the initial energy of the electron. τ_0 presents the injection time of the electron. Since a monochromatic relativistic oscillation is required to generate a narrow radiation spectrum, it is better to choose a initial injection phase where E_z is so small that the change of $\gamma(\tau)$ is negligible. Therefore, with the following initial conditions: 1) relativistic electron, $\gamma_0 \gg 1$; 2) transversely broad laser pulse, $r_m \gg |\mathbf{r}-\mathbf{r_c}(\tau)|$; 3) initial injection phase at $\zeta_0 = -5\pi/2$ where $E_z = 0$ and $\gamma(\tau) = \gamma_0$; 4) no phase slippage considered in theory (as verified by the PIC simulations that these assumptions are reasonable for our case as shown in Fig. 3.8), Eq. (3.22) becomes a driven harmonic oscillator as

$$\frac{d^2\mathbf{r}_\perp}{d\tau^2} + \Omega_\beta^2\mathbf{r}_\perp = \Omega_\beta^2\mathbf{r}_c(\tau), \tag{3.24}$$

where the betatron frequency is defined as

$$\Omega_\beta = \frac{2a_0}{r_m}\sqrt{\frac{C}{\gamma_0}}. \tag{3.25}$$

Using the laser pulse centroid trajectory given in Eq. (3.14), the solution is given as (please see the details in Appedix. B.2)

$$\begin{aligned}\frac{d\mathbf{r}_\perp}{\gamma_0 d\tau} = \mathbf{u}_\perp = &-\left[\frac{a_u\Omega_\beta}{\Omega}\left(\frac{\boldsymbol{\epsilon}+\boldsymbol{\epsilon}^*}{2}\right)+\gamma_0\Omega_\beta\mathbf{r}_{\perp,\mathbf{0}}\right]\sin\Omega_\beta\tau\\ &+\left[\mathbf{u}_{\perp,0}+a_u\left(\frac{i\boldsymbol{\epsilon}-i\boldsymbol{\epsilon}^*}{2}\right)\right]\cos\Omega_\beta\tau\\ &-a_u\left[\frac{i\boldsymbol{\epsilon}e^{i\Omega\tau}-i\boldsymbol{\epsilon}^*e^{-i\Omega\tau}}{2}\right],\end{aligned} \tag{3.26}$$

where $\mathbf{r}_{\perp,\mathbf{0}} = (x_0, y_0)$ and $\mathbf{u}_{\perp,0} = (u_{x,0}, u_{y,0})$ are the vectors of initial electron transverse coordinates and momenta components, respectively, and

$$a_u = \frac{\gamma_0\Omega\Omega_\beta^2 r_{c,0}}{\Omega^2-\Omega_\beta^2}, \tag{3.27}$$

is the undulator strength of the electron. It is seen from Eq. (3.26) that this oscillation couples the intrinsic betatron oscillation of frequency Ω_β with the undulator oscillation of frequency Ω driven by the centroid oscillation of laser pulse. As shown in Fig. 3.5, the 3D trajectory is shown by the blue line and projections on xz- and yz-plane are shown by the green lines. As a result, such coupled oscillation gives two narrow peaks in the radiation spectrum, one of which comes from the betatron oscillation and another from the undulator oscillation as discussed in Sec. 3.5.

As seen from Eq. (3.26), by matching the following conditions

$$\begin{aligned}&\frac{a_u\Omega_\beta}{\Omega}\left(\frac{\boldsymbol{\epsilon}+\boldsymbol{\epsilon}^*}{2}\right)+\gamma_0\Omega_\beta\mathbf{r}_{\perp,\mathbf{0}}=0,\\ &\mathbf{u}_{\perp,0}+a_u\left(\frac{i\boldsymbol{\epsilon}-i\boldsymbol{\epsilon}^*}{2}\right)=0,\end{aligned} \tag{3.28}$$

the oscillation of the injected electron becomes monochromatic

$$\frac{d\mathbf{r}_\perp}{\gamma_0 d\tau} = \mathbf{u}_\perp = -\frac{a_u}{2}(i\boldsymbol{\epsilon}e^{i\Omega\tau}+c.c.), \tag{3.29}$$

and will only give one single peak in the undulator radiation spectrum. For example,

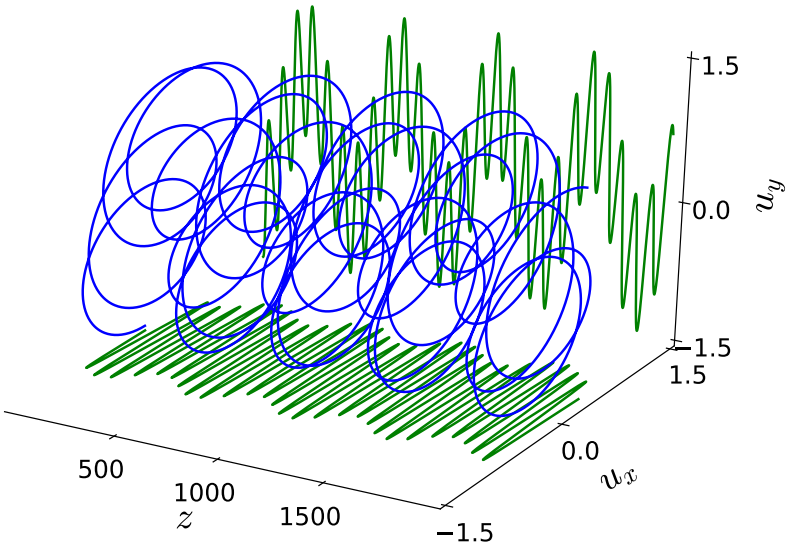

Figure 3.5: The trajectory of an single electron inside the plasma undulator field. Blue solid line: the trajectory in 3D space; green solid lines: projections of the trajectory on xz- and yz-plane.

by considering an optimized injection of electron

$$\mathbf{r}_{\perp,0} = \left(-\frac{a_u}{\gamma_0 \Omega}, 0\right) \quad \text{and} \quad \mathbf{u}_{\perp,0} = (0, -a_u), \tag{3.30}$$

which satisfies the conditions in Eq. (3.28), the matched trajectory is shown in Fig. 3.6 where is only the undulator oscillation.

Now, effect of the exponential term $\exp\left(-2\left(\mathbf{r} - \mathbf{r_c}(\tau)\right)^2 / r_m^2\right)$ in the wakefield Eq. (3.21) can be evaluated by comparing the fully numerical solution directly obtained by solving the Lorentz equation in Eq. (2.1) with the analytical solution in Eq. (3.29) as shown in Fig. 3.6, where $r_{c0} = 0.18 \ll r_m = 2$. It is seen that the exponential term in the wakefield Eq. (3.21) only slightly lowers the amplitude of oscillation and then is not important in our case. This effect on an electron

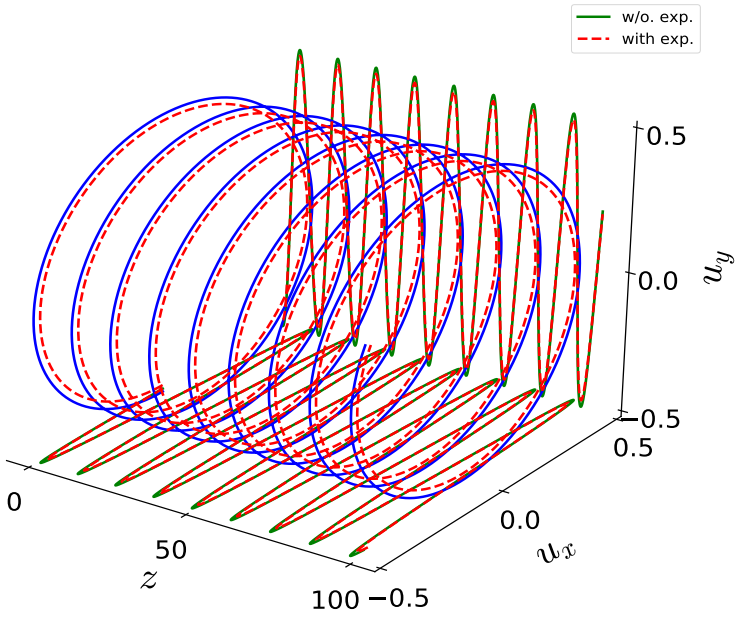

Figure 3.6: The trajectory of a single electron with the matching conditions in Eq. (3.28) inside the plasma undulator field. Blue solid line: the trajectory without considering the exp. term in the wakefield Eq. (3.21) in 3D space; green solid lines: projections of the trajectory on xz- and yz-plane; red dashed lines are the fully numerical trajectory with considering the exp. term in 3D space and its projections.

beam is discussed in Sec. 3.4 and shows that it is also negligible for properly chosen parameters of the electron beam and laser pulse.

Another considerable issue here is the dephasing of an electron with respect to the plasma wave and should be alleviated by implementing a longitudinal plasma density ramp as discussed in Sec. 2.3.4. As shown in Fig. 3.7 is the result from a PIC simulation where an electron (denoted by a black star) is initially injected into the phase $\zeta_0 = -5\pi/2$ of the wakefield. The length of the laser pulse is $\lambda_p/2$ and the strength is $a_0 = 0.3$. The on-axis plasma density of parabolic channel is $1.0 \times 10^{18}\mathrm{cm}^{-3}$. A longitudinal plasma density ramp has been implemented according Eq. (2.56). It is seen that the electron is locked to its initial phase so well even

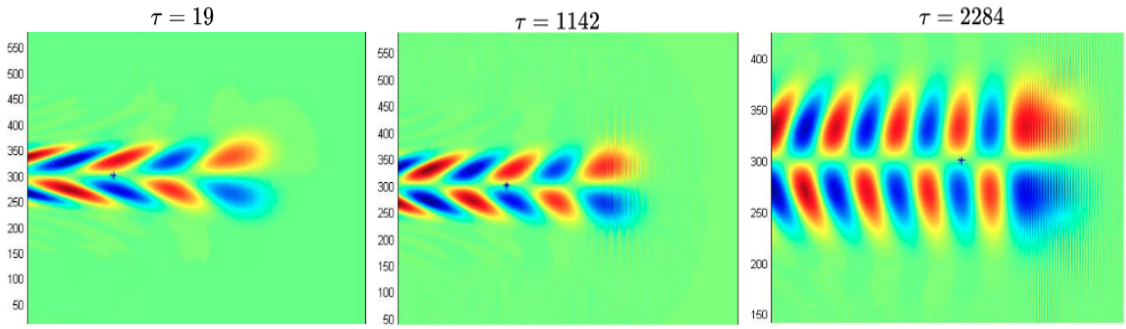

Figure 3.7: The phase position of an single electron inside a wakefield after propagation: 1) $\tau = 19$; 2) $\tau = 1142$; 3) $\tau = 2284$. The electron is seen as the back star and initially injected at the phase $\zeta = -5\pi/2$.

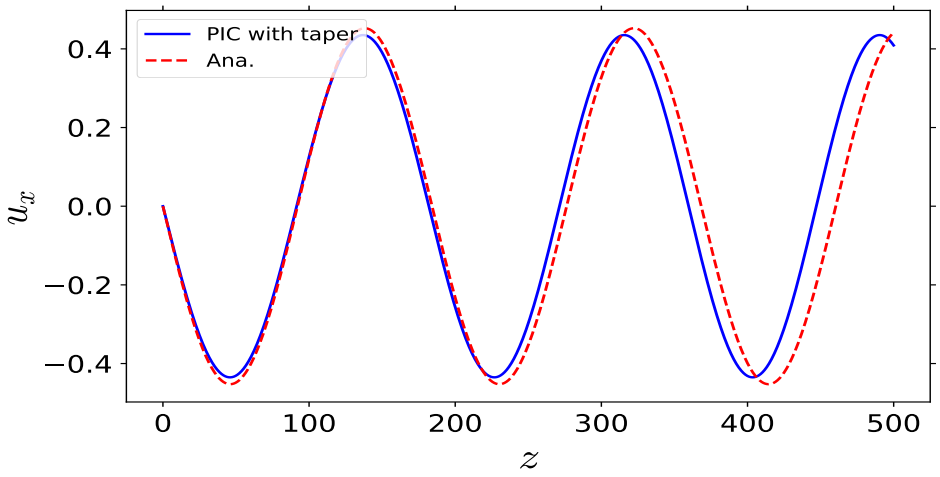

Figure 3.8: Trajectories of the electron inside the wakefield as shown in Fig. (3.7). 1) blue solid line: PIC simulation with plasma density taper; 2) red dashed line: analytical solution from Eq. (3.29).

after quite long propagation distance. Therefore, as shown in Fig. 3.8, its oscillation dynamics will not be significantly affected by the acceleration. The frequency is increased due to the density up-ramp, but is still within the scope of consideration. Therefore, the dephasing issue can be neglected here.

3.4 Evolution of an electron beam

An electron beam inside the plasma wakefield also undergoes the envelope and centroid oscillation that is quite similar to a laser pulse as discussed in Sec. 3.2. As shown in Fig. B.1, dynamics of an electron beam is obtained from a 2D VDSR simulation (please see more details about this simulation in Appendix. B.3). Fig. B.2 shows the evolution of its transverse root-mean-square (RMS) spot size $\sigma_{b,x} = \sqrt{\langle x^2 \rangle - \langle x \rangle^2}$, where the electron beam has the spatial Gaussian distribution and its center is optimized with the injection condition in Eq. (3.30) to alleviate the betatron oscillation. The condition for a single electron in Eq. (3.30) actually works quite well for a narrow electron beam $r_m \ll r_u$, where r_u is the amplitude of undulator oscillation. Dynamics of the electron beam is dominated by the undulator oscillation as shown in Figs. B.1 and B.3. Therefore, the centroid oscillation is largely driven by the undulator field with the frequency Ω. Envelope oscillation comes from the finite distribution of the phase space as seen in Figs. B.1 and B.2. By using 2D equation of motion for a single electron inside the plasma channel undulator field in Eq. (3.24), the envelope equation is given as (see the details in Appendix. (B.3))

$$\frac{\mathrm{d}^2 \sigma_{b,x}}{\mathrm{d}\tau^2} + \Omega_\beta^2 \sigma_{b,x} - \frac{\epsilon_{b,x,n}^2}{\gamma^2 \sigma_{b,x}^3} = 0, \tag{3.31}$$

where $\epsilon_{b,x,n} = \gamma\beta\sqrt{\sigma_{b,x}^2 \sigma_{b,\dot{x}}^2 - \sigma_{b,x,\dot{x}}^2}$ is the normalized transverse emittance of the electron beam [83], $\sigma_{b,x}^2 = \langle x^2 \rangle - \langle x \rangle^2$ is the RMS beam radius and $\sigma_{b,\dot{x}}^2 = \langle \dot{x}^2 \rangle - \langle \dot{x} \rangle^2$ is is the divergence in $\hat{x}$ direction and $\sigma_{b,x,\dot{x}} = \langle (x - \langle x \rangle)(\dot{x} - \langle \dot{x} \rangle) \rangle$. It is seen from Eq. (3.31) that the envelope equation is same as the case of only the betatron oscillation [47]. Therefore, the undulator driven force actually does not effect the envelope oscillation because this force is of independence on the transverse position within the approximation of a broad laser pulse. This feature will be very beneficial to another

proposed scheme as discussed in Chapter 5. By considering an electron beam without energy spread, then $\sigma_{b,x,\dot{x}} = 0$ and $\epsilon_{b,x,n} = \sigma_{b,x}\sigma_{b,\dot{x}}$ and solution of Eq. (3.31) reads as,

$$\sigma_{b,x}^2 = \frac{1}{2}(\sigma_{b,x,0}^2 + \frac{\sigma_{b,x,m}^4}{\sigma_{b,x,0}^2}) + \frac{1}{2}(\sigma_{b,x,0}^2 - \frac{\sigma_{b,x,m}^4}{\sigma_{b,x,0}^2})\sin 2\Omega_\beta \tau, \tag{3.32}$$

where $\sigma_{b,x,0}$ is the initial transverse beam size, and $\sigma_{b,x,m} = \sqrt{\epsilon_{b,x,n}/(\gamma_0\Omega_\beta)}$ is the matched beam size. The RMS betatron oscillation strength is obtained from Eq. (3.26) as

$$\begin{aligned}\langle a_{\beta,x}^2 \rangle = \gamma_0^2\Omega_\beta^2\sigma_{b,x,0}^2 + \sigma_{b,\dot{x},0}^2 \\ + \left[\gamma_0\Omega_\beta \langle x_{b,x,0}\rangle + \frac{a_u\Omega_\beta}{\Omega}\left(\frac{\epsilon_i + \epsilon_i^*}{2}\right)\right]^2 \\ + \left[\langle u_{x,0}\rangle + a_u\left(\frac{i\epsilon_i - i\epsilon_i^*}{2}\right)\right]^2.\end{aligned} \tag{3.33}$$

For example, with the simulation parameters summarized in Table.(B.1), the undulator strength is approximately $\langle a_u \rangle = 1.02$ and the RMS betatron strength is $\langle a_{\beta,x}^2 \rangle \simeq 0.55$. A general evolution of the beam envelope is shown in Fig. (B.2) and agrees with the analytical solution in Eq. (3.32). The envelope oscillates with a frequency $2\Omega_\beta$. In order to keep the envelope of a electron beam constant as

$$\frac{d^2\sigma_{b,x}}{d^2\tau} = 0, \tag{3.34}$$

the beam size should be initially matched by $\sigma_{b,x,0} = \sigma_{b,x,m}$ as seen from Eq. (3.32). With this condition, the envelope keeps almost constant during the centroid oscillation (shown by the white line) as shown in Figs. B.3 and B.4. The very slight variation of the envelope is caused by the finite longitudinal distribution of the electron beam. The situation is same in $\hat{y}$-direction. In 3D case, the initial matching condition becomes

$\sigma_{b,0} = \sigma_{bm}$ where

$$\begin{aligned} \sigma_{b,0} &= \sqrt{\sigma_{b,x,0}^2 + \sigma_{b,y,0}^2}, \\ \sigma_{bm} &= \sqrt{\sigma_{b,x,m}^2 + \sigma_{b,y,m}^2}. \end{aligned} \tag{3.35}$$

With this dynamics, the electron beam is capable of generating the radiation with very narrow bandwidth.

3.5 X-ray radiation of narrow bandwidth spectrum

Radiation emitted from an oscillating electron inside the plasma undulator field in Eq. (3.21) can be numerically calculated from Eq. (A.37) with the transverse trajectory in Eq. (3.26). For a single electron without the matching condition in Eq. (3.28), the radiation spectrum is generated by the mixture of betatron and undulator oscillation as shown by the red dashed line in Fig. 3.9. The peak between $0.2 < \kappa < 0.3$ is generated by the betatron oscillation and another one around $\kappa = 0.5$ by the undulator oscillation. In comparison, the radiation spectrum from a pure undulator oscillation with the trajectory in Eq. (3.29) only has one higher peak around $\kappa = 0.5$ shown by the solid blue line, where most of radiation energy resides in the major emission line.

2D Numerical simulations are performed by VDSR with a parabolic plasma channel of on-axis density 1×10^{18} cm^{-3} [102]. A linearly polarized Gaussian laser pulse of strength $a_0 = 0.2$ and spot size $r_m = 1.4$ which matches the condition in Eq. (3.12). The electron beam is of charge $1pC$, energy $\gamma_0 = 1000$ and energy spread $\Delta\gamma/\gamma_0 = 2.0\%$. Four different beam configurations are summarized in Tab. 3.1 including: a) electron beam is matched with condition in Eq. (3.34) and optimally injected

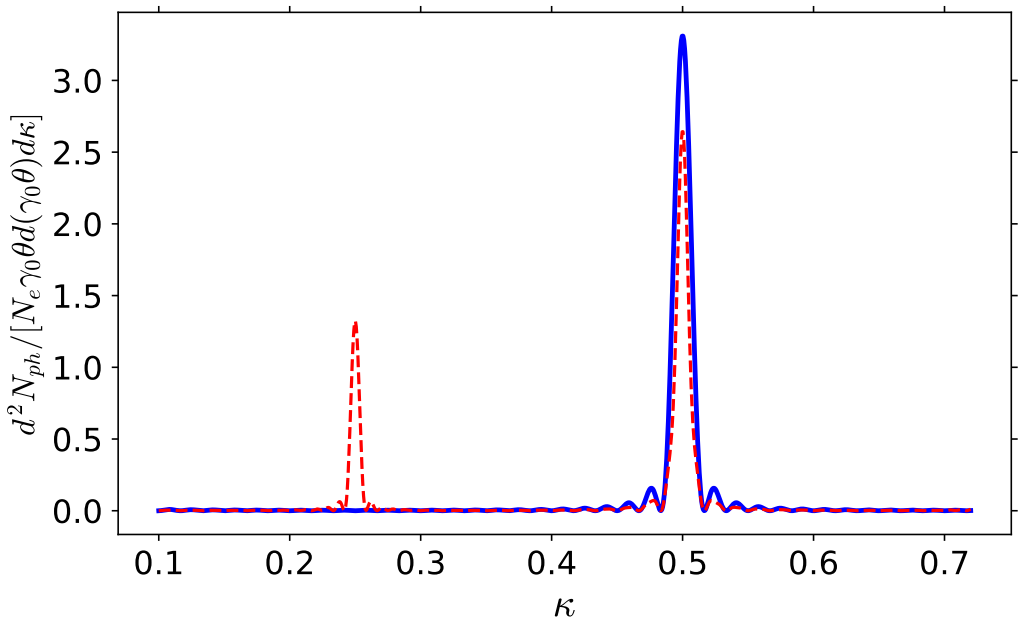

Figure 3.9: On-axis radiation spectrum from an single electron undergoes, blue solid line: only undulator oscillation; dashed red line: mixture of betatron and undulator oscillation.

	(a)	(b)	(c)	(d)
Injection position x_0	0.04	0.0	0.04	0.04
Injection momentum,$u_{x,0}$	0	0	0	0
Initial divergence, $\sigma_{b,\dot{x},0}$	0.398	0.398	0.398	0.398
Initial beam size, $\sigma_{b,x,0}$	0.0477	0.0477	0.0295	0.0477
Normalized Emittance	0.019	0.019	0.0118	0.019

Table 3.1: Electron beam parameters for VDSR simulations to calculate radiation spectrum for four different cases corresponding to the plots (a),(b,)(c) and (d) in Fig. (3.10). The oscillation number is $N_u = 30$.

into the plasma undulator with condition in Eq. (3.28) without the exponential term in Eq. (3.21); b) configuration is the same as case (a), except to match the injection condition in Eq. (3.28); c) configuration is the same as case (a), except to match the beam condition in Eq. (3.34); d)configuration is the same as case (a) except to match the beam condition in Eq. (3.34), except with exponential term in Eq. (3.21).

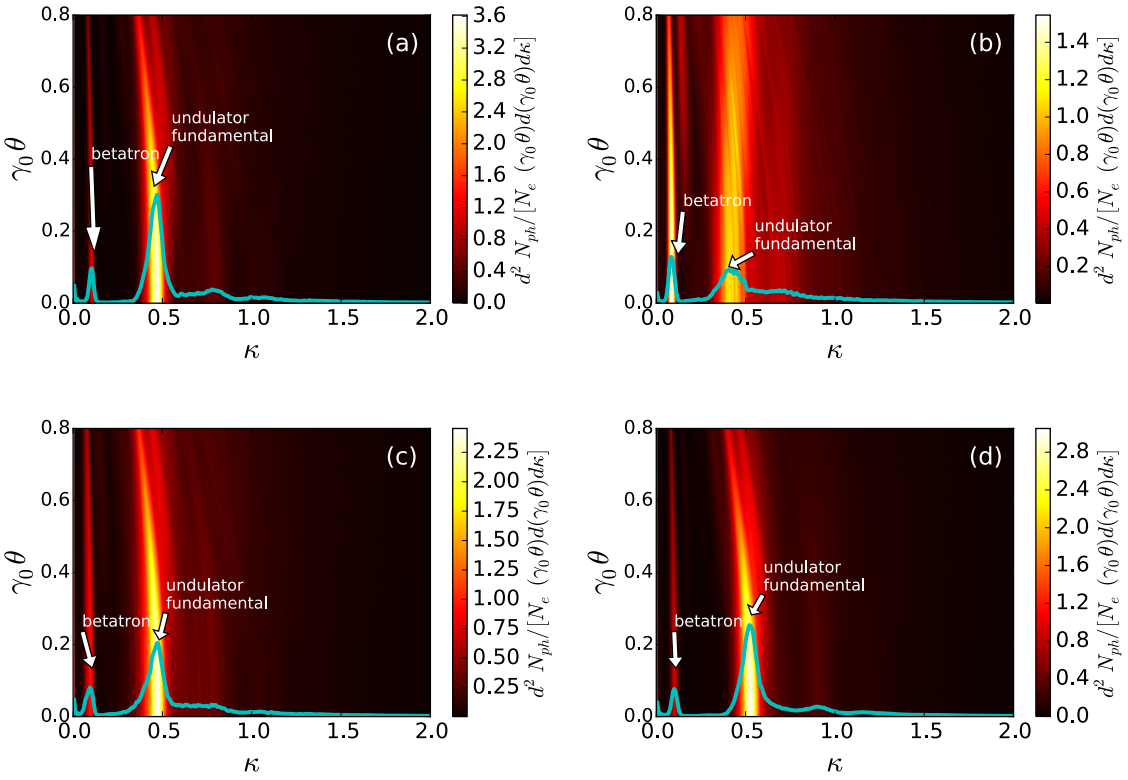

Figure 3.10: Radiation spectrum of electron beam for four cases corresponding to the configurations a), b), c) and d) in Table.(B.1), respectively.

Since the injection condition in Eq. (3.28) depends on the local injection phase, the betatron emission line can not be completely removed due the longitudinal dimension of the beam, but can only be compressed. This compression will, in turn, increase the intensity of undulator radiation as seen by comparing Fig. 3.10.a) with 3.10.b). The envelope oscillation of an electron beam leads to the momentum and energy spread which broadens the radiation spectrum and then decreases the intensity as described by Eq. (2.69). This effect can be seen by comparing Fig.(3.10.a) with (c). As a result, the beam matching condition in Eq. (3.34) is very necessary. The effect of exponential term in the field Eq. (3.21) on the radiation spectrum can be seen by comparing Fig. 3.10.a) with 3.10.d). It is slight and not important in current configurations.

As discussed in Sec. 2.4, a radiation spectrum will be broadened due to the finite

dimension of electron beam which introduces the energy and momentum spread. The acceleration can also introduce the energy chirp inside wakefield. However, the energy chirp due to the acceleration can be neglected if the phase lock is implemented and the electron beam only has a small transverse size, $\sigma_{b,x,0} \ll 1$. From Eq. (2.69), the spectrum width becomes

$$\left[\frac{\Delta\omega}{\omega}\right]_{FWHM} \approx \sqrt{\left(\frac{1}{N_u}\right)^2 + \left(\frac{2\Delta\gamma_0}{\gamma_0}\right)^2 + \left(\frac{\gamma_0\Delta\theta_0}{4}\right)^4}. \tag{3.36}$$

For example, considering an electron beam with $\Delta\theta_0 = 1$mrad and $\Delta\gamma_0/\gamma_0 = 0.02$, the bandwidth is 7% for an oscillation of 30 periods.

3.6 Conclusion

The plasma channel undulator is presented in this chapter to generate the x-ray radiation with a narrow-bandwidth spectrum. A controllable undulator field is produced by injecting a short laser pulse into the parabolic plasma channel with a small offset, or an angle with respect to the axis. Such a field provides an undulator strength for the injected electron smaller than unity, $a_u < 1$, and is very beneficial in generating x-ray radiation with very narrow bandwidth. By matching the injection conditions of an electron beam to eliminate the envelope oscillation, the quality of the emitted photon beam can be further improved.

Chapter 4

Gamma-ray radiation from plasma-based resonant wiggler

In this chapter, a plasma-based resonant wiggler is proposed to generate the flexible γ-ray radiation as shown in Fig. 4.1. It is demonstrated that the radiation energy can be largely increased in comparison with the previously proposed scheme in Chapter 3. The basic theory is presented in Sec. 4.1 in order to achieve the plasma wiggler by

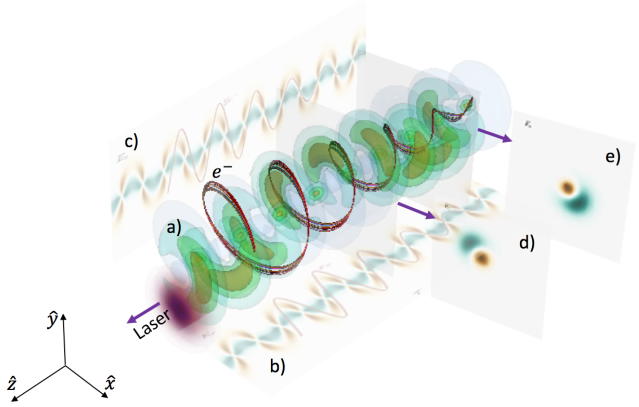

Figure 4.1: Demonstration of resonant plasma wiggler. a): 3D helical plasma wakefield is shown in colored surface and short laser pulse as purple spot on the left. They oscillate in a period of laser pulse Rayleigh length around z axis. Electron trajectories of resonance is shown as red lines. They linearly increase with time; b) and c): projection of electric field and electron trajectory on $\hat{x}\hat{z}$ and $\hat{y}\hat{z}$ plane; d) and e): slices of electric field at two different longitudinal position, z.

inducing centroid oscillations of a short laser pulse in a parabolic plasma channel. In Sec. 4.2, the evolution of a single electron and an electron beam in such a wiggler field is discussed to achieve a better quality of radiation spectrum. The γ-ray radiation of synchrotron-like broad spectrum is calculated in Sec. 4.3. Tunability of the radiation is then discussed. In Sec. 4.4, the conclusion for this chapter is presented.

4.1 Resonant oscillation of an electron inside a parabolic plasma channel

A laser pulse can be guided in a tailored plasma channel to suppress the pulse diffraction and to sustain a large accelerating gradient for a long distance, as discussed in Chapter 3. Trajectory of a laser pulse with a small angle or off-set with respect to the axis is given in Eq. (3.14) for the parabolic plasma channel. The polarization of the laser centroid oscillation can be controlled by choosing the initial transverse injection positions and angles, for example, in Eqs. (3.12) and (3.13). For simplification, we only focus on the linearly polarized case of $\hat{x}$-direction in this chapter. Other cases, e.g. $\hat{y}$ and circular polarization, could be treated in the same way. To consider the case where a laser pulse enters the plasma channel off-axis in $\hat{x}\hat{z}$-plane, the initial injection parameters are chosen as $y_{c0} = 0,$ and $\theta_{y0} = 0,\ \theta_{x0} = 0$ in Eq. (3.14). Then, the linearly polarized laser centroid oscillation is given as

$$x_c(\tau) = x_{c0} \cos \Omega\tau \quad \text{and} \quad y_c(\tau) = 0. \tag{4.1}$$

Considering a linearly $\hat{y}$-polarized ($a_x = 0$) Gaussian laser pulse with a moderate strength $a_y = a_0 \exp(-\xi^2/w_z^2) \exp[-(x - x_c(\tau))^2/r_m^2]$, where $a_0 < 1$, w_z is the initial pulse length, $\xi = z - \tau$ is the co-moving variable, and $r_m = k_p/\sqrt{\pi r_e' \Delta n}$ is the matched

initial pulse spot size [46], the generated wakefield is then given by Eqs. (3.20) and (3.21) in Sec. 3.2. An electron experiences transverse focusing/undulating force and longitudinal accelerating force inside the acceleration phase $-\pi < \xi < -\pi/2$. Similar to Chapter. 3, 2D case is considered now. For a wide laser pulse ($|r_m| \gg |x - x_c|$), the exponential $\exp(-2(x - x_c)^2/r_m^2) \approx 1$ is neglected especially in the early interaction stage. Therefore, the wakefield in Eqs. (3.20) and (3.21) become harmonic,

$$E_z = a_0^2\, C\, \cos\xi, \tag{4.2}$$

$$E_x = -\frac{4a_0^2\, C}{r_m^2}\,[x - x_c(\tau)]\sin\xi. \tag{4.3}$$

By assuming that the dynamic of electron is dominated by the longitudinal motion, $\beta_x \ll \beta_z \approx 1$, where $\beta_x = dx/d\tau$ and $\beta_z = dz/d\tau$, then it is reasonable to neglect the $(dx/dt)^2$ term in the momentum equation of electron Eq. (C.1), one can get the equation of transverse motion of an electron in this wakefield as

$$\frac{d^2x}{d\tau^2} + \frac{R_\delta}{1 + R_\delta\tau}\frac{dx}{d\tau} + \frac{\Omega^2}{\mu(1 + R_\delta\tau)}\, x = \frac{x_{c0}\Omega^2\cos(\Omega\tau)}{\mu(1 + R_\delta\tau)}, \tag{4.4}$$

where $\mu = -\mu_0/\sin\xi$, $\mu_0 = \Omega^2/\Omega_\beta^2$ and Ω_β is the betatron frequency defined in Eq. (3.25). Eq. (4.4) is a 2D time-dependent driven damped oscillator in $\hat{x}\hat{z}$ plane. The second term gives the time-dependent damping effect and the third corresponds to the time-dependent betatron oscillation. The term on the right-hand side (RHS) is the extra force which drives a stable oscillation if the amplitude is properly small. Otherwise, it may lead to a chaotic motion which goes to destroy the electron beam as shown in Fig. 4.6.

The main energy gain occurs in the longitudinal direction due to the field component

E_z in Eq. (4.2) as

$$\delta = -\int_0^\tau (\beta_x E_x + E_z) d\tau' \simeq R_\delta \tau, \tag{4.5}$$

where R_δ is defined as the energy gain rate of the electron in the wakefield

$$R_\delta = -\frac{r_m^2 \Omega_\beta^2 \cos\xi}{4}. \tag{4.6}$$

It is easily noticed that the oscillation occurs in phase range -$\pi \leq \xi \leq -\pi/2$. The phase of injected electron could be approximately locked to a fixed position in the wakefield, e.g. $\xi \simeq \xi_0 = const.$, ξ_0 is the initial injection phase of the electron into the plasma channel. This can be achieved by longitudinally applying a plasma density ramp as discussed in Sec. 2.3.4. By defining a new variable, $s = (2Q_f/\mu)\sqrt{1 + \Omega\tau/Q_f}$, where $Q_f = \Omega/R_\delta$ is the initial quality factor of the oscillation, equation of motion Eq. (4.4) becomes

$$\frac{d^2x}{ds^2} + \frac{1}{s}\,\frac{dx}{ds} + x = g(s), \tag{4.7}$$

where $g(s) = x_{c0}\cos(\frac{\mu}{4Q_f}s^2 - Q_f)$. The solution is given by

$$x(s) = \big[c_1 + \nu_1(s)\big]J_0(s) + \big[c_2 + \nu_2(s)\big]Y_0(s), \tag{4.8}$$

where c_1 and c_2 are constants determined by initial conditions. $\nu_1(s)$ and $\nu_2(s)$ are variable coefficients. Please see more details of the derivation in Appendix.C.

The dependence of the maximum oscillation amplitude on the parameters μ_0 and ξ_0 during an interacting time $\tau = 4000$ is shown in Fig. 4.2. The color is scaled by the parameter of maximum oscillation strength of the electron, K, which is also the maximum transverse momentum of the electron normalized with $m_e c$. It reaches the peak at its primary resonant state as seen the ridge of the surface, where $\mu = -\mu_0/\sin\xi_0 = 1$. This is the state where betatron oscillation of electron is resonant

with the laser centroid oscillation. This means if the condition $\mu = 1$ is satisfied, the electron can undergo a resonant oscillation which can be used to increase the oscillation amplitude. It is also seen that the resonance dies out when $\mu \neq 1$. This can be achieved by the energy gain or loss of the electron, as indicated by the $R_\delta \tau$ term in Eq. (4.4). For the typical laser-plasma and electron beam configurations, R_δ is very small, for example, in our case $R_\delta \sim 10^{-4}$. As a result, the small R_δ leads to a relatively long resonant process duration $\Delta\tau$, which is determined by the acceleration phase of electron in the wakefield, $\Delta\tau \propto 1/|\xi_0 + \pi/2|$. As a result, the initial resonant process can persist for a duration of a few oscillation periods sufficient to increase the oscillation amplitude. A semi-steady oscillating pattern with a large amplitude will be formed subsequently after the resonance is totally broken where μ is far away from 1. It should be mentioned that the initial injection phase $\xi_0 = -\pi/2$ should be avoided because there is no acceleration and then the resonance is undamped. This leads to the continuous growth of the electron transverse amplitude till the electron escapes from the plasma wakefield transversely and is, hence, lost. The solution $x(s)$ is plotted for $\mu = 1$ and $\xi_0 = -1.25\pi/2$ as seen the dashed red line in Fig. 4.3. It is seen that the oscillation amplitude is increased during the initial resonance section, $\tau < 5000$, by comparing to the non-resonant case as seen the green solid line with $\mu \simeq 1.5$ which gives the oscillating strength less than unity, $K < 1$. The semi-steady oscillating pattern with the large amplitude is then formed after the resonance gradually dies out, $\tau > 5000$, where $K > 1$. The exponential term in the equations of wakefield Eq. (3.21) and (3.20) inhibits the semi-steady oscillation and then decreases the oscillation amplitude and frequency by comparing the blue solid and red dashed line in Fig. 4.3 (a) and (b), or even destroy the beam as shown in Fig. 4.6. Therefore, it is better to initially keep x_{c0}/r_m small to avoid too strong effects from exponential term. Anyway, it is also seen that this effect is negligible in the early section $\tau < 10000$ due to the strong resonance.

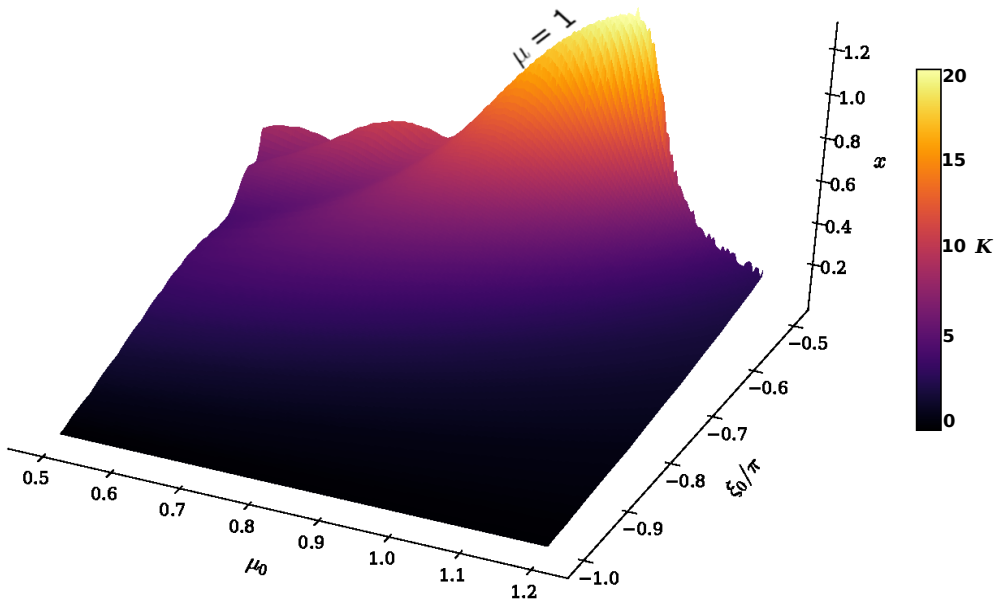

Figure 4.2: The dependence of oscillation amplitude and strength on the parameters μ_0 and ξ_0 from analytical solution $x(s)$. Color is scaled by the value of the strength parameter K.

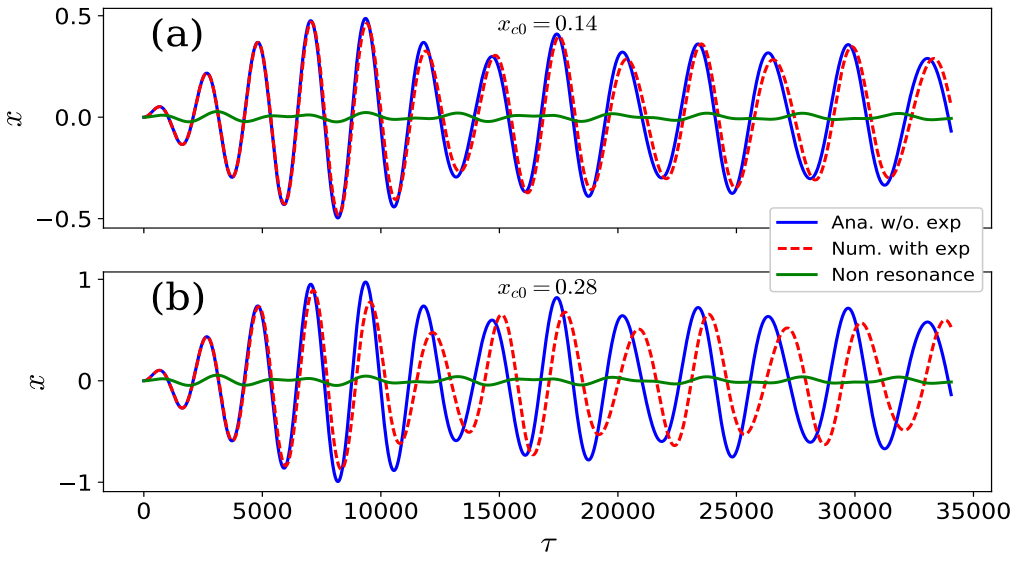

Figure 4.3: Electron trajectory in plasma wakefield-based wiggler. Blue solid: full numerical resonance solution from momentum equation with the 2D electric field of Eq. (3.21) and (3.20); red dashed: analytical resonance solution of Eq. (4.8) with $\mu \simeq 1.0$; Green solid: analytical non-resonance solution of Eq. (4.8) with $\mu \simeq 1.5$, with different initial laser pulse displacements, (a) $x_{c0} = 0.14$; (b)$x_{c0} = 0.28$.

Stronger oscillation strength K requires the larger initial centroid displacement of laser pulse, x_{c0}, since $g(s) \propto x_{c0}$ in Eq. (4.7). In the other hand, larger x_{c0} leads to the faster frequency damping as seen by the red dashed line in Fig. 4.3 (b). This feature limits the radiation spectrum to be further extended to the high energy region and will be discussed later in Sec. 4.3. For this reason, nonlinear plasma wakefield should be considered.

4.2 Electron beam evolution in a plasma wiggler

Dynamics of one electron inside a beam can be treated in the same way as one single free electron in Sec. 4.1. The collective dynamics of the electron beam concerned here is the transverse envelope oscillation, the equation of which is directly obtained from Eq. (4.4) as

$$\frac{d^2\sigma_x}{d\tau^2} - \frac{R_\delta}{1+R_\delta\tau}\frac{d\sigma_x}{d\tau} + \frac{\Omega^2}{\mu(1+R_\delta\tau)}\sigma_x - \frac{\varepsilon_x^2}{\sigma_x^3} = 0, \tag{4.9}$$

where $\sigma_x = \sqrt{< x^2 > - < x >^2}$ is the transverse beam size in $\hat{x}\hat{z}$ plane. Since the energy gain rate is usually very small in the case concerned, $R_\delta \ll 1$, the energy gain in the early interaction stage can be neglected. Then, dynamics of transverse beam envelope becomes similar to the situation in Sec. 3.4. As a result, the beam size can approximately keep constant if the initial beam size is matched as

$$\sigma_{b,x,m} = \sqrt{\frac{\mu\varepsilon_{n,x}}{\gamma_0\Omega}}, \tag{4.10}$$

where $\varepsilon_{n,x}$ is the dimensionless normalized RMS beam emittance. Thus, the beam divergence is given as

$$\sigma_{\theta,x,m} = \frac{\varepsilon_{n,x}}{\sigma_{b,x,m}} \tag{4.11}$$

2D VDSR simulations have been carried out to check the evolution of the spot size of

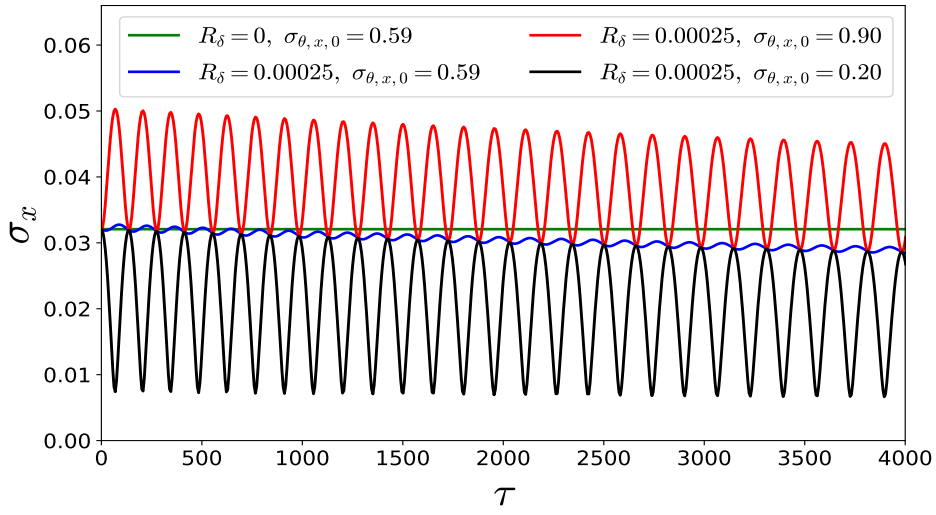

Figure 4.4: The evolution of transverse beam size evolution in plasma wakefield. Green: $R_\delta = 0$ and initial beam size is matched by $\sigma_{\theta,x,0} = 0.59$; Blue: $R_\delta \neq 0$ and initial beam size is matched by $\sigma_{\theta,x,0} = 0.59$; Red: $R_\delta \neq 0$ and initial beam size is not matched by $\sigma_{\theta,x,0} = 0.90$; Black: $R_\delta \neq 0$ and initial beam size is not matched by $\sigma_{\theta,x,0} = 0.2$.

a Gaussian electron beam. The matched parameters for the simulation are as follows: total charge $1pC$, $\varepsilon_{n,x} = 0.1\mu$m, initial central Lorentz factor $\gamma_0 = 800$, laser spot size $r_m = 1.6$, the matched RMS beam size $\sigma_{b,x,0} = 0.032$, and the corresponding RMS divergence $\sigma_{\theta,x,0} = \varepsilon_{n,x}/\sigma_{b,x,0} = 0.59$. The result is shown by the blue line in Fig. 4.4. The oscillation of transverse size of the matched beam is much weaker than the unmatched beam which is shown by the red and black lines. By comparing with the green line for the case of $R_\delta = 0$, one can conclude that the oscillation and reduction of the beam size is caused by the slow energy gain in the wakefield. Therefore, dynamics of an electron beam with a moderate transverse beam size can also be described by Eq. (4.4) in the same way as a single electron. As shown in Fig. 4.5, the trajectory of an electron beam (blue solid lines) agrees well with the analytical solution of a single electron (red dashed line).

To further verify the theory, 2D PIC simulations have been performed for the initially resonant case with the 2D/3D PIC code LAPINE [127] on JURECA [74] at Jülich

Supercomputing Center. The resonant condition $\mu = 1$ is initially matched at the phase $\xi_0 = -1.25\pi/2$. A y-polarized Gaussian laser pulse with a wavelength of 1 μm propagates into a parabolic plasma channel with an offset $x_{c0} = 0.05$ (or $x'_{c0} = 0.3$ μm) with respect to the z-axis. The normalized laser intensity is $a_0 = 0.9$ with a spot size of $w_0 = 1.6$ (or $w'_0 = 8.5$ μm) and a pulse duration FWHM (full width at half maximum) of $w_\tau = 10.2$ (or $w'_\tau = 40$ fs). The initial on-axis plasma density along the propagation axis z is $n_{0,i} = 0.001 n_c$, where n_c is the plasma critical density. A longitudinal plasma density ramp is implemented as discussed in Eq. (2.56). An electron beam with a Gaussian transverse profile $n_b(x) = n_{b0} \exp(-x^2/2\sigma_x^2)$ with $n_{b0} = 0.01 n_{0,i}$ and $\sigma_x = 0.42$ (or $\sigma'_x = 0.5$ μm), corresponding to normalized emittance $\varepsilon_{n,x} = 0.025$ μm, is injected into the plasma channel. The beam profile in the longitudinal direction is uniform. The length of the beam is 1.8 μm, spanning over the phase range $-\pi < \xi_0 < -\pi/2$. The RMS energy spread of the electron beam is $\sigma_\gamma/\gamma_0 = 1\%$ with $\gamma_0 = 800$. Part of trajectories of the electrons inside the beam are shown by the solid lines in Fig. 4.5 and the color is scaled by the RMS Lorentz factor of the electron beam. The dashed black line is for the trajectory of the electron initially residing around the matched phase $\xi_0 = -1.25\pi/2$. An analytical solution for an electron with the same phase position is also presented by the green dashed line. It shows that the electron dynamics is weakly dependent on ξ_0 especially during the resonant stage $\tau < 1500$ due to the small energy gain rate R_δ. Therefore, the initial resonant process can be used to efficiently enhance the oscillation amplitude of electron beam without severely increasing the beam divergence. The resonance dies out after $\tau > 1500$ where $\gamma > 1200$.

However, the electron beam will be destroyed if a large initial laser pulse off-set x_{c0} is applied as shown in Fig. 4.6, where $x_{c0} = 0.2\pi$ (or $x'_{c0} = 3\mu m$). After propagation of $z = 160\pi$, the oscillation gets unstable and then starts the chaotic motion after $z = 560\pi$. The reason is that the significant nonlinear effect of high-order terms is

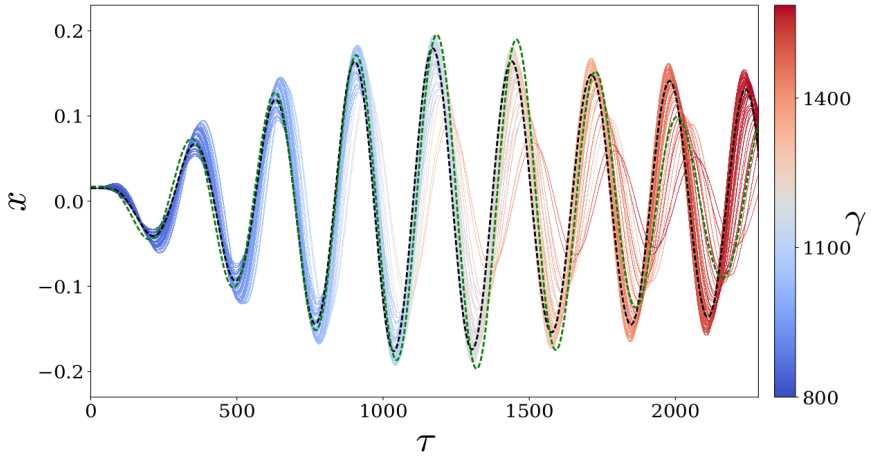

Figure 4.5: Solid lines: trajectories of electrons from PIC simulation. The color map indicates gamma factor of electrons; dashed black line: trajectory of one electron from PIC simulation initially at $\xi_0 = -1.25\pi/2$; dashed green line: trajectory of an single electron from analytical solution with $\xi_0 = -1.25\pi/2$.

introduced into the equation of motion from the exp-term in the wakefield Eqs. (3.20) and (3.21),

$$e^{-2(x-x_c)^2/r_m^2} \simeq 1 - \frac{2(x-x_c)^2}{r_m^2} + \cdots . \tag{4.12}$$

For example, the second-order term leads to a Duffing oscillator [73].

In order to further increase the oscillation strength and then to extend the radiation spectrum to higher energy region, this limitation imposed by the initial off-set x_{c0} should be overcome. Here, a nonlinear wakefield excitation is considered where $a_0 > 1$. A 2D PIC simulation for the nonlinear case is then done with the laser pulse of $a_0 = 3.0$, and $x'_{c0} = 1.5$ μm. It shows that our theory of resonant oscillation can still works for a self-trapped electron especially in the early propagation section. The trajectory of an self-trapped electron is traced from the PIC simulation and shown in Fig. 4.7. The color map is scaled by its Lorentz factor. It shows the similar resonant and semi-steady oscillation to the linear case.

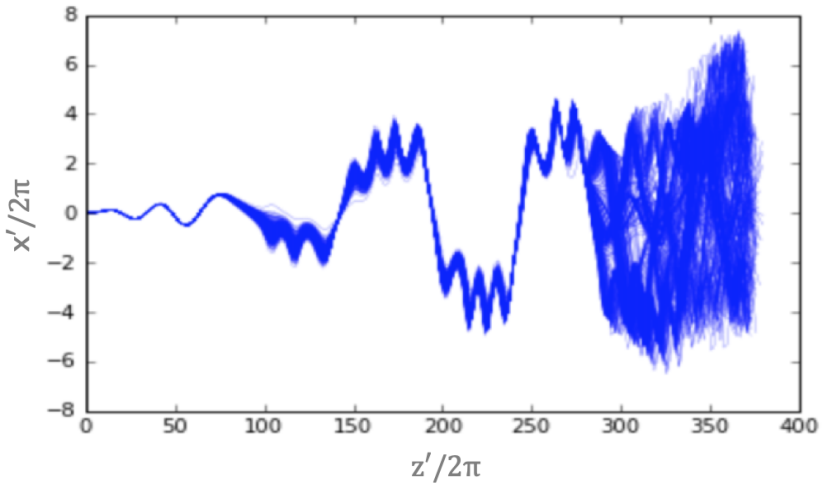

Figure 4.6: VDSR simulation of electron beam dynamics with large initial laser pulse off-set, $x_{c0} = 0.2\pi$.

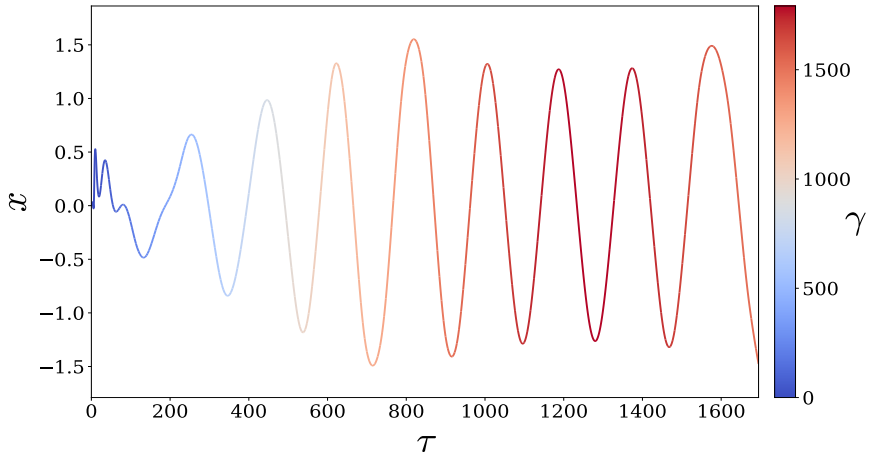

Figure 4.7: Trajectory of an self-trapped electron undergoing the initial resonant oscillation in the nonlinear wakefield. The color map is scaled by its Lorentz factor of the electron.

4.3 γ-ray radiation of synchrotron-like broad spectrum

The radiation is calculated from the Lienard-Wiechert potentials as discussed in Sec. 2.4. For a Gaussian laser pulse in the resonant case, the critical frequency is

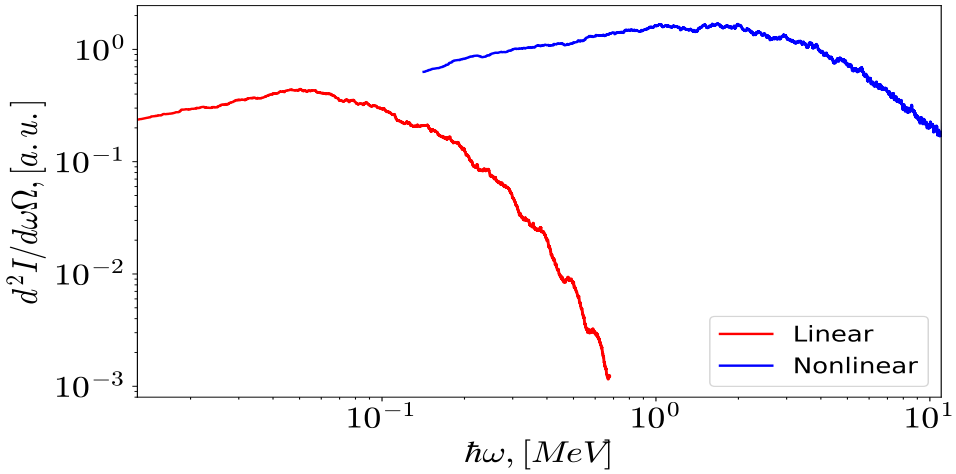

Figure 4.8: On-axis radiation spectrum of a single electron in the laser plasma wakefield. Red: linear case; Blue: nonlinear case.

then estimated as $\omega_c \simeq (-4\gamma^2 a_0^2 C x_0 \sin\xi_0)/w_m^2$. The spectrum of the on-axis radiation of a single electron is presented in Fig. 4.8 which uses the trajectory from PIC simulation shown by the black line in Fig. 4.5, where $K \simeq 15$. The estimated peak frequency $\omega_{peak} = 0.3\omega_c \simeq 0.12$MeV agrees with the numerical calculation in Fig. 4.8. Higher critical frequency requires a large oscillation strength of the electron K and then a larger initial laser pulse displacement x_{c0}. For a fixed spot size of laser pulse r_m, increasing of x_{c0} is limited by the exponential term in the linear wakefield as discussed in Sec. 4.2. As a result, it is impossible to limitlessly increase the radiation spectrum to higher energy region. For the linear case, the energy of emitted photon is limited to less than 1MeV. However, a nonlinear laser-plasma wakefield can be considered to further increase the energy, namely, $\hbar\omega_c >$ 1MeV. With the trajectory of a single electron in a nonlinear wakefield as shown in Fig. 4.7, the on-axis radiation spectrum is largely extended, as seen the blue line in Fig. 4.8, where the peak is around 2MeV.

4.4 Conclusion

In conclusion, a compact laser-plasma-based wiggler is proposed to generate γ-ray radiation. Such a wiggler is able to work in the linear laser-plasma wakefield regime, in which the electron oscillation amplitude is enhanced by the resonance of betatron oscillation and centroid oscillation introduced by laser pulse. This potentially provides approximately two orders of magnitude higher photon energy than the betatron radiation generated directly from the plasma bubble [98, 71], and about one order of magnitude higher energy than the recently proposed plasma-based γ-ray source [33]. The limitation of the linear wakefield can be overcome by considering the nonlinear case, to extend the energy frontier further, in which case the self-trapped electrons are resonantly oscillated and the energy of emitted photons can be enhanced to the strong γ-rays range with increased brightness. This flexible and compact scheme may provide a wide range of applications in scientific research, medicine, and industry.

Chapter 5

Plasma channel undulator/wiggler by using higher-order laser modes

A plasma undulator/wiggler may be created through the plasma wakefield excited by beating several different HG modes co-propagating in a plasma channel. In this chapter, the concept of a plasma channel undulator/wiggler using higher-order laser modes is demonstrated. In Sec. 5.1, the basic theory for guiding the high-order modes in a parabolic plasma channel is discussed. In Sec. 5.2, the undulator field will be generated and controlled by tuning the mode parameters, such as number of modes, colour, amplitude, and phase. In Sec. 5.3, the dynamics of a single electron and an electron beam in such a wakefield will be presented. The spectrum of generated radiation is calculated in Sec. 5.4. In Sec.5.5, the conclusion for this chapter is presented.

5.1 High-order modes guiding inside a parabolic plasma channel

The equation governing the dynamics of the slowly-varying envelope $\tilde{a}_\perp(\tau, x, y)$ of a laser pulse inside the parabolic plasma channel is given in Eq. (3.4) with the PA. If a dimensionless laser pulse vector potential is then given by $a_\perp(\tau, \rho, \zeta) = eA_\perp/m_e c^2 = 1/2\,\tilde{a}_\perp(\tau, \rho)g(\zeta)\exp(iM_p\zeta) + c.c.$, where $A_\perp$ is the laser pulse vector potential in CGS, $g(\zeta)$ is the laser pulse temporal envelope (normalized to 1), the general solutions of the Schrödinger equation in Eq. (3.4) for the 2-dimensional harmonic oscillator in Cartesian geometry are well-known [78]. A propagating, linearly polarized laser pulse can be written as a Hermite-Gaussian mode of order m and n as follows

$$\tilde{a}_\perp(\tau, x, y) = \frac{a}{2}\eta\chi(x, y)e^{-i\theta\tau + i\varphi}, \tag{5.1}$$

where a is the amplitude of the mode and φ is its phase. $M_{p,(m,n)}$ is introduced to take into account that modes can have different wavelengths, where m and n are numbers of mode in $\hat{x}$ and $\hat{y}$ directions respectively. $\eta = 1/\sqrt{2^{m+n}m!n!}$ is the normalization coefficient. $\chi(x, y) = H_m(x/\sqrt{R})H_n(y/\sqrt{R})\exp\{-(x^2 + y^2)/2R\}$, $\theta = (1/2M_{p,(m,n)} + (m + n + 1)/M_{p,(m,n)}R)$, where $H_n(x)$ is a Hermite polynomial of n-th order. Please see Appendix. D.1 for more details of derivation.

Mode given by Eq. (5.1) represents the stationary state and propagates along the channel with constant centroid position and spotsize. Dynamics of any laser pulse, propagating along the channel, can be represented as the superposition of such different Hermite-Gaussian modes

$$a_\perp(\tau, x, y, \zeta) = \sum_\nu a_{\perp,\nu}(\tau, x, y, \zeta), \tag{5.2}$$

where $a_{\perp,\nu}(\tau, x, y, \zeta)$ represents the νth mode. As discussed in [38], it is beneficial to use a superposition of different Hermite-Gaussian modes for controlling the focusing force of the plasma wakefields, which might help to reduce electron beam divergence. In the case of the superposition of various Hermite-Gaussian modes, due to the difference in the phase velocity, the intensity profile

$$I = a_\perp(\tau, x, y, \zeta) a_\perp(\tau, x, y, \zeta)^*, \tag{5.3}$$

will contain interference terms and can lead to the oscillatory structure which is dependent on the mode numbers. The oscillation frequency induced by two pulse of different modes, denoted by ν and λ, is $\Omega_{\nu,\lambda} = \Delta\theta_{\nu,\lambda} = \theta_\nu - \theta_\lambda$. With n laser pulses, the oscillation amplitude is increased by $n!/2$ in the resonant case if $\Omega_{\nu,\lambda} = \Omega$ is the same for every set of two different modes. Please see Appendix. D.2 for more details of the intensity oscillation.

5.2 Wiggler/undulator field structure

Undulator field structure, i.e. the structure of the excited plasma wakefield, can be calculated from the propagation of the laser pulse (here and further, by the laser pulse a mixture of several higher-order Hermite-Gaussian modes is understood). The equation for the dimensionless scalar potential of a wakefield $\phi = e\Phi/m_e c^2$ is given in Eq. (2.40). With these assumptions stated in Sec. 3.2, the solution is given in Eq. (2.42) which depends on the intensity structure of the laser pulse.

By considering a laser pulse representing the beating of several different modes as

$$a_\perp(\zeta') = \sum_\nu \tilde{a}_{\perp,\nu}(\tau, x, y) g_\nu(\zeta') \exp(iM_{p,\nu}\zeta'), \tag{5.4}$$

where $\tilde{a}_{\perp,\nu}$ represents the vector potential of the ν^{th} mode with mode numbers m_ν and n_ν and $M_{p,\nu}$ represents its "mass", the RHS in Eq. (2.42) can be written as

$$\frac{a_\perp a_\perp^*}{2} = \frac{1}{4}\sum_\nu \left|\tilde{a}_{\perp,\nu}\right|^2 g_\nu^2 + \frac{1}{2}\sum_{\nu\neq\lambda} \mathrm{Re}\{\tilde{a}_{\perp,\nu}\tilde{a}_{\perp,\lambda}^*\} g_\nu g_\lambda, \tag{5.5}$$

The second term, interference between every set of two different modes is nonzero if the modes have parallel polarization [38].

Assuming beating of N laser pulses with the different modes and the same longitudinal size, $w_{z,\nu} = w_z$, and then $g_\nu^2(\zeta) = e^{-2\zeta^2/w_z^2}$, for the solution of ϕ, one can write

$$\begin{aligned}\phi(\zeta,x,y) =& C_\beta \sin\zeta \sum_{\nu=1}^{N} a_\nu^2 \eta_\nu^2 \chi_\nu^2 \\ &+ \sin\zeta \sum_{\nu\neq\lambda}^{N} C_{u,\nu,\lambda} a_\nu a_\lambda \eta_\nu \eta_\lambda \chi_\nu \chi_\lambda \cdot \cos(\Omega_{\nu,\lambda}\tau - \Delta\varphi_{\nu.\lambda}),\end{aligned} \tag{5.6}$$

where $C_\beta = \frac{1}{4}\sqrt{\frac{\pi}{2}} w_z e^{-w_z^2/8}$, $C_{u,\nu,\lambda} = C_\beta e^{-\Delta M_{p,\nu,\lambda}^2 w_z^2/8} \cosh\frac{\Delta M_{p,\nu,\lambda} w_z^2}{4}$. $\Delta M_{p,\nu,\lambda} = M_{p,\nu} - M_{p,\lambda}$ describes the possible difference of modes' wavelengths. $\Omega_{\nu,\lambda} = \theta_\nu - \theta_\lambda$ is the term describing the oscillation frequency of a beating wave due to the interference of two different modes and $\Delta\varphi_{\nu,\lambda} = \varphi_\nu - \varphi_\lambda$ describes the phase difference. The first term in Eq. (5.6) drives the betatron oscillation of the electron and the second term is responsible for the oscillatory intensity profile (see Fig. D.1). The amplitude of the wakefield has a maximum at $w_z = 2$, and in this case $C_{\beta,\max} = \frac{1}{2}\sqrt{e^{-1}\pi/2} \approx 0.38$. Note that for the case of a single mode, $\{m = 0, n = 0\}$, where the interference term vanishes, one recovers the usual linear theory solution of the plasma wakefield driven by a Gaussian laser pulse as discussed in Chapter 3 and 4.

Magnetic fields, that are proportional to a_0^4 [59], are neglected in the linear case $a_0 < 1$, and the electric fields are given by $\mathbf{E} = -\nabla\phi(\zeta,x,y)$, where the gradient is taken in (ζ,x,y) coordinates. The electric field is normalized to mc^2k_p/e. Assuming

k_p as constant, the transverse wakefield is given by:

$$\begin{aligned}\boldsymbol{E}(\zeta,\boldsymbol{r},\tau) = 2C_\beta \sin\zeta \sum_\nu a_\nu^2 \eta_\nu^2 \chi_\nu \boldsymbol{\kappa_\nu} \\ + \sin\zeta \sum_{\nu\neq\lambda} C_{u,\nu,\lambda} a_\nu a_\lambda \eta_\nu \eta_\lambda (\chi_\nu \boldsymbol{\kappa_\lambda} + \chi_\lambda \boldsymbol{\kappa_\nu}) \cdot \cos(\Omega_{\nu,\lambda}\tau - \Delta\varphi_{\nu.\lambda}),\end{aligned} \tag{5.7}$$

where $\boldsymbol{\kappa_i} = (\kappa_{x,i}, \kappa_{y,i})$ with $i = (\nu, \lambda)$, and

$$\begin{aligned}\kappa_{x,i} = -\partial\chi_i/\partial x = &\frac{H_{n_i}(y/\sqrt{R})}{\sqrt{R}}\Bigg(H_{m_i+1}(x/\sqrt{R}) \\ &- \frac{x}{\sqrt{R}} H_{m_i}(x/\sqrt{R})\Bigg) e^{-\frac{x^2+y^2}{2R}},\end{aligned} \tag{5.8}$$

$$\begin{aligned}\kappa_{y,i} = -\partial\chi_i/\partial x = &\frac{H_{m_i}(x/\sqrt{R})}{\sqrt{R}}\Bigg(H_{n_i+1}(y/\sqrt{R}) \\ &- \frac{y}{\sqrt{R}} H_{n_i}(y/\sqrt{R})\Bigg) e^{-\frac{x^2+y^2}{2R}},\end{aligned} \tag{5.9}$$

The exponential terms in Eqs. (5.8) and (5.9) decrease the amplitude of the field in transverse directions and can be neglected near the $\hat{z}$ axis or for a wide laser pulse. Then, the field in Eq. (5.7) becomes approximately harmonic if the two beating modes have different parity, e.g. even and odd modes. The polarization of oscillation of the wakefield can be controlled by the laser pulse amplitude ratio and the phase. For example, the simple cases of linear and circular polarization are discussed as following.

5.2.1 Linear oscillation of transverse wakefield

Considering two modes, $\{m = 0, n = 0, a = a_0\}$ and $\{m = 1, n = 0, a = a_1\}$ with the same initial phase, $\Delta\varphi = 0$, the near-axis wakefield is obtained from Eq. (5.7) by

$$
\begin{aligned}
E_x(\zeta,x,\tau) \simeq & \frac{2C_\beta}{R}(a_0^2-2a_1^2)\sin\zeta\cdot x \\
& - C_\beta\sqrt{\frac{2}{R}}a_0a_1\sin\zeta\cdot\cos(\Omega\tau), \\
E_y(\zeta,y,\tau) \simeq & \frac{2C_\beta}{R}a_0^2\sin\zeta\cdot y, \\
E_z(\zeta,y,\tau) \simeq & -C_\beta(a_0^2+\frac{2x^2}{R}a_1^2)\cos\zeta \\
& - C_\beta\sqrt{\frac{2}{R}}a_0a_1\cos\zeta\cdot x\cdot\cos(\Omega\tau),
\end{aligned}
\tag{5.10}
$$

where the exponential and higher-order of $x/\sqrt{R}$ are neglected by the assumption of a wide laser pulse, $x^2+y^2 \ll R$, and $\Omega=\Omega_{0,1}$. One can see that the oscillation of the transverse wakefield is linearly polarized in $\hat{x}\hat{z}$ plane.

5.2.2 Circular oscillation of transverse wakefield

Considering three modes, $\{m=0,n=0,a=a_0,\varphi=0\}$, $\{m=1,n=0,a=a_1,\varphi=0\}$ and $\{m=0,p=1,a=a_2,\varphi=\pi/2\}$, the near-axis wakefield is then given with the same assumptions above as:

$$
\begin{aligned}
E_x(\zeta,x,\tau) \simeq & \frac{2C_\beta}{R}(a_0^2-2a_1^2)\sin\zeta\cdot x \\
& - C_\beta\sqrt{\frac{2}{R}}a_0a_1\sin\zeta\cdot\cos(\Omega\tau), \\
E_y(\zeta,y,\tau) \simeq & \frac{2C_\beta}{R}(a_0^2-2a_2^2)\sin\zeta\cdot y \\
& - C_\beta\sqrt{\frac{2}{R}}a_0a_2\sin\zeta\cdot\sin(\Omega\tau), \\
E_z(\zeta,y,\tau) \simeq & -C_\beta\left[a_0^2+\frac{2}{R}(a_1^2x^2+a_2^2y^2)\right]\cos\zeta \\
& - C_\beta\left[\sqrt{\frac{2}{R}}a_0a_1\cdot x\cdot\cos\Omega\tau\right. \\
& \left.+\left(\frac{2}{R}a_1a_2\cdot xy+\sqrt{\frac{2}{R}}a_0a_2\cdot y\right)\cdot\sin\Omega\tau\right]\cos\zeta.
\end{aligned}
\tag{5.11}
$$

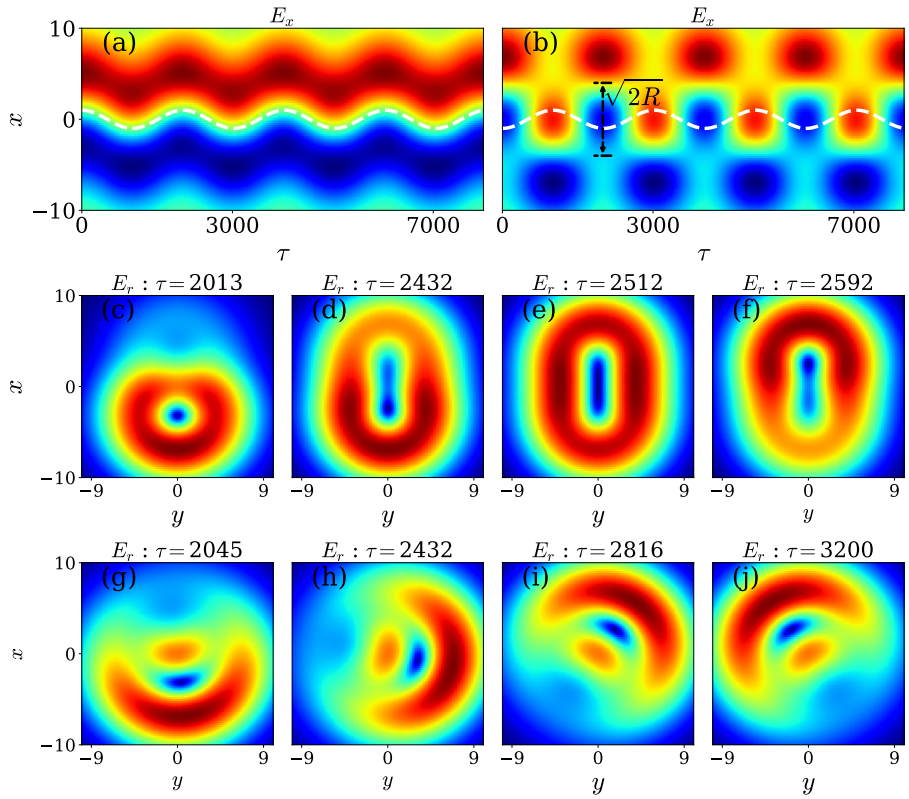

Figure 5.1: (a), (b) Projection of the transverse wakefield E_x, generated by two different modes without and with the condition in Eq. (5.12), as a function of time τ on $\hat{x}\hat{z}$ plane. The dashed white lines show the trajectories of an electron in the wakefield; (c), (d), (e), (f) Slices of the transverse wakefield E_r, generated by two different modes with the condition in Eq. (5.12), on $\hat{x}\hat{y}$ plane at four different propagation positions, $\tau = 2429, 2432, 2512, 2592$, respectively; (g), (h), (i), (j) Slices of transverse wakefield E_r, generated by three different modes with the condition in Eq. (5.12), at four different propagation positions, $\tau = 2045, 2432, 2816, 3200$, respectively.

One can see that ellipticity of the oscillation can be controlled by the difference of the laser strength, a_0, a_1 and a_2. For example, the oscillation of transverse wakefield is circularly polarized in the transverse plane if $a_1 = a_2$ near the axis of the plasma channel.

As seen from Eqs. (5.10) and (5.11), if the condition:

$$a_0^2 - 2a_1^2 = 0 \quad \text{or/and} \quad a_0^2 - 2a_2^2 = 0, \tag{5.12}$$

is satisfied, the electric field is independent of the spatial coordinates and becomes uniform near the propagation axis $|x| < \sqrt{R/2}$. Therefore, there is no betatron focusing force experienced by an injected electron. As shown in Fig. 5.1.a), the projection of the transverse wakefield on the $\hat{x}\hat{z}$ plane, E_x, is generated by two different modes without the condition (5.12). An electron in such a wakefield undergoes both betatron and undulator oscillations and can be treated in the same way as in the previous Chapter 3 and 4, where an electron beam principally undergoes an envelope oscillation due to the betatron focusing force. Such oscillation will give rise to the spread of momentum and energy of the electron beam, and subsequently broaden the radiation spectrum as discussed later. In order to alleviate this limit, matching demands are made on the injection conditions of the electron beam as given in Eqs. (3.28) and (3.35) which, unfortunately, are currently difficult to realize in some experiments. However, through application of the matching conditions in Eq. (5.12), the transverse wakefield becomes harmonic near the $\hat{z}$ axis, $|x| < \sqrt{R/2}$ as shown in Fig. 5.1.b), which releases the requirements of the initial injection conditions to compress envelope oscillation introduced by the betatron focusing force inside the plasma wakefield. As a result, the electron beam maintains good quality during propagation inside such a wakefield as discussed in Sec. 3.4. This is very beneficial for the generation of a narrow-band radiation spectrum for electron beam experiments. Note that significant inaccuracy in the real experimental conditions, such as errors on a_0, may cause the condition (5.12) to be unfulfilled. Therefore, as seen from Eqs. (5.10) and (5.11), the matching condition given by Eq. (5.12) required for restriction in this regime demands that the variation δa_0 from laser field strength parameters $a_0' = a_0 + \delta a_0$ is limited by $\delta a_0 \ll C_u a_{(1,2)}/(\sqrt{2}C_\beta)$, where $a_{(1,2)}$ denotes strength parameter of second or third mode, and a_0 satisfies the condition in Eq. (5.12). However, in this thesis, such experimental uncertainty is neglected purely for an illustrative purpose.

The slices of the transverse wakefield $E_r = \sqrt{E_x^2 + E_y^2}$ generated by two and three

modes at four different propagation positions with the matching condition (5.12) are shown in Fig. 5.1.(c)-(f) and (g)-(j) respectively. For the case of two modes, the wakefield linearly oscillates only in $\hat{x}$ direction and is normal in $\hat{y}$ direction. For the case of three modes, the wakefield rotates around the propagation $\hat{z}$ axis. As a result, the electron injected into such a wakefield undergoes an oscillation with the same polarization of the oscillation of wakefield.

5.3 Electron dynamics

For simplicity, the 2D wakefield with the linear oscillation in $\hat{x}\hat{z}$ plane is considered and the circular case can be treated in the same way. Without the condition in Eq. (5.12), the dynamics of electron is the same as discussed in Chapter 3 and 4. Now, by considering the condition in Eq. (5.12), the transverse electric field generated by beating two different modes at a fixed phase, for example, two modes: $\{m = 0, n = 0, a = a_0\}$ and $\{m = 1, n = 0, a = a_1\}$ at $\zeta = -3\pi/2$, becomes purely periodic as

$$E_x(x, \tau) = E_0 \cos(\Omega\tau), \tag{5.13}$$

where $E_z = 0$ and $E_0 = C_u a_0 a_1 \sqrt{2/R}$ is the amplitude of the wakefield. It is the same as the field in a conventional undulator without introducing the betatron oscillation of electron beam caused by the focusing force [124]. For a relativistic electron injected with Lorentz factor $\gamma_0 \gg 1$, the transverse motion is simply described by a linear harmonically driven oscillator equation:

$$\frac{du_x}{d\tau} = -E_0 \cos(\Omega\tau). \tag{5.14}$$

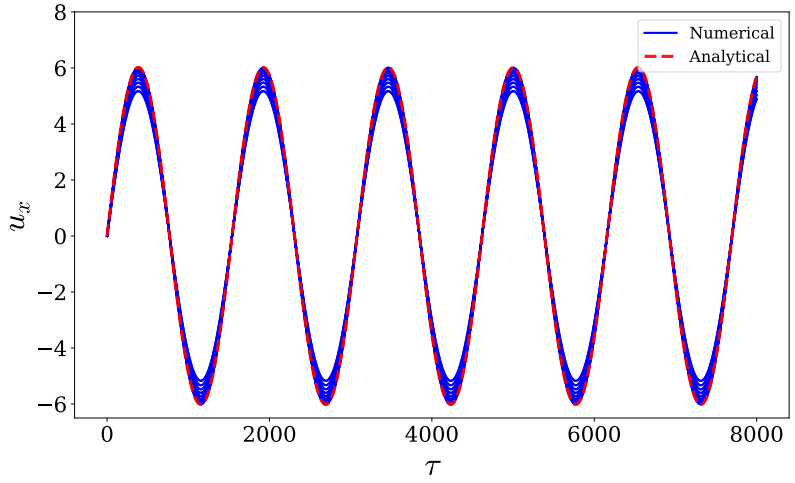

Figure 5.2: The normalized momentum u_x in $\hat{x}$ direction. Red dashed line: analytical result from Eq. (5.15); Blue solid lines: numerical results obtained for an electron beam by solving the transverse momentum equation with the electric field in Eq. (5.7).

By assuming that the electron is initially injected along longitudinal direction without a transverse momentum, $u_x(\tau = 0) = 0$, the solution is given by:

$$u_x = -a_u \sin(\Omega\tau), \tag{5.15}$$

where $u_x = p_x/m_e c$ is the normalized transverse momentum in $\hat{x}$ direction and $a_u = E_0/\Omega$ is the oscillation strength.

Note that the Eq. (5.15) is the exact solution for an electron propagating on the $\hat{z}$ axis and is capable of describing an electron beam, because there is no betatron oscillation in such a wakefield. In Fig. 5.2, the blue solid lines are numerical results obtained by a VDSR simulation for an electron beam of spot size $\sigma_b = 4.0$ and $\sigma_\theta = 0$, and the red dashed line is the analytical result from Eq. (5.15). The wakefield is generated by beating two linear polarized laser pulses, $\{m = 0,\ n = 0,\ a = 0.56,\ r_m{=}6,\ \varphi = 0\}$ and $\{m = 1,\ n = 0,\ a = 0.4,\ r_m{=}6,\ \varphi = 0\}$. The on-axis ($x = 0$) numerical result of u_x agrees exactly with the analytical result in Eq. (5.15) with very weak betatron oscillation. The decreasing of off-axis results is caused by the

exponential term in Eq. (5.7). For a wide laser pulse, this decrement is slight in comparison with the result in Fig. 4.5. This feature promises the small momentum and energy divergence of the electron beam while propagating inside this wakefield, and then a narrow undulator radiation spectrum as shown in Eq. (2.69). Another considerable issue is the phase slippage which may leads to the ac/deceleration. But it is not important if the parameters are properly chosen. Please see more details in Appendix. D.3.

5.4 Radiation generation

The oscillation strength a_u is in a broad range, $0 < a_u < \gamma_0\Omega\sqrt{2R}$. As a result, it is capable of generating a narrow x-ray radiation spectrum for a small $a_u < 1$, as well as the synchrotron-like x/γ-ray radiation for the large $a_u > 1$.

5.4.1 Radiation spectrum with narrow bandwidth

The radiation spectrum of an single electron can be numerically calculated from Lienard-Wiechert potentials in Eq. (A.37) by using the transverse trajectory in Eq. (5.15). In a plasma channel of on-axis density $n_0 = 10^{18}$ cm^{-3}, a spatially and temporally Gaussian electron beam is used with the parameters as $\zeta = -3\pi/2$, total charge $Q = 1$ pC, transverse radius in $\hat{x}$ direction $x_b = 0.1$, temporal length $\Delta\tau_b = 0.2$, energy $\gamma_0 = 1000$ and energy spread $\sigma_\gamma/\gamma_0 = 1\%$. The radiation is calculated by VDSR simulation. Fig. 5.3.a) shows the narrow x-ray radiation spectrum $d^2N_{ph}/[N_e(\gamma_0\theta)d(\gamma_0\theta)d\kappa]$ generated by two beating laser pulses $\{m = 0,\ n = 0,\ a = 0.21,\ r_m$=1.14, $\varphi = 0\}$ and $\{m = 1,\ p = 0,\ a = 0.15,\ r_m$=1.14, $\varphi = 0\}$ after $n_u = 30$ periods of oscillations, where the total oscillation length is much smaller than the dephasing length $L_d \approx 7000$. N_{ph} is the number of emitted photons and N_e is the number of electrons inside the beam. The azimuthal angle is normalized as

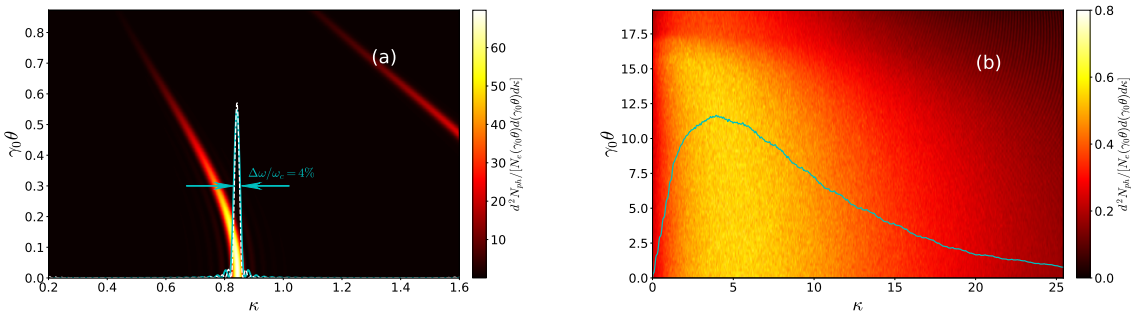

Figure 5.3: Radiation spectrum from plasma-based undulator/wiggler with (a) $a_u \simeq 0.62$ and (b) $a_u \simeq 16$. Dashed white line is the theoretical on-axis solution and solid cyan lines in both plots are for the numerical on-axis radiation with $\gamma_0\theta = 0$.

$\gamma_0\theta$ and the frequency is $\kappa = \omega/(2\gamma_0^2\Omega)$. The oscillation strength is $a_u \simeq 0.62$. The solid cyan line shows the numerical on-axis radiation spectrum of the electron beam at $\gamma_0\theta = 0$. The central frequency is $\kappa = 0.83$ ($\hbar\omega_{ce} = 2.93$ keV) with a FWHM bandwidth of $\Delta\omega/\omega = 4\%$. It mainly benefits from the elimination of the betatron oscillation of the electron beam.

Here, the broadening of radiation spectrum considered includes: a) spread of beam energy $\Delta\gamma$ due to initial energy spread and energy chirp caused by the acceleration; b) transverse momentum spread Δa_u due to structure of longitudinal electric field in Eq. (D.26), but spread from the phase slippage is not considered as in Sec. 5.3. Therefore, the broadening of the radiation spectrum with respect to the theoretical natural bandwidth of an single electron could be estimated from Eq. (2.69) as

$$\left[\frac{\Delta\omega}{\omega}\right]_{FWHM} \approx \sqrt{\left(\frac{1}{N_u}\right)^2 + \left(\frac{2\Delta\gamma}{\gamma_0}\right)^2 + \left(\frac{\Delta a_u}{4\gamma_0}\right)^2}, \tag{5.16}$$

where $\Delta\gamma$ is from the initial energy spread as well as the energy chirp caused by the finite duration of electron beam and contributes extra 0.5% broadening in our case. Δa_u mainly comes from the phase slippage of electrons and the finite duration of electron beam, and contributes extra 0.2%.

5.4.2 Synchrotron-like broad radiation spectrum

For large $a_u > 1$, this scheme is also capable to generate a synchrotron-like spectrum with the critical frequency of $\omega_{cr} = (3/2)\gamma_0^2 E_0 = (3/2)\gamma_0^2 c_u a_0 a_1 / r_m$. Fig. 5.3(b) shows the synchrotron-like hard x-ray radiation spectrum generated by two beating laser pulses $\{m = 0,\ n = 0,\ a = 0.84,\ r_m$=1.14, $\varphi = 0\}$ and $\{m = 1,\ n = 0,\ a = 0.6,\ r_m$=1.14, $\varphi = 0\}$. The oscillation strength is $a_u \simeq 16$. The critical frequency is $\kappa = 5.45$ ($\hbar\omega_p = 19$ keV).

5.5 Conclusion

In this chapter, the scheme of plasma undulator/wiggler produced by beating several HG laser pulses with different mode numbers in a parabolic plasma channel is theoretically discussed. The oscillation of the excited plasma wakefield is caused by the interference between each set of two different modes. The oscillation frequency is then determined by the difference of parameters of the modes, $\Omega_{\nu,\lambda} = \theta_\nu - \theta_\lambda$. From the non-paraxial wave equation of laser pulse and linear laser-plasma wakefield theory, the undulator field is derived using Cartesian geometry. The polarisation of the field is also discussed for the special case. An initial matching condition of pulse strength is given to produce a harmonic field, where the focusing force is totally removed near the propagation axis. As a result, there is no betatron oscillation for an electron beam and the quality of the emitted photon beam is largely improved. The dynamics of an injected electron are studied in the linearly polarised wakefield. The oscillation strength $a_u = E_0/\Omega \propto a_0 a_1 r_m$ occurs within a wide range, and is capable of producing a plasma-based undulator field for a narrow x-ray source or a wiggler field for a broad synchrotron-like x/γ-ray source. The current scheme is much easier

to implement in experiments by comparing with the schemes proposed in Chapter 3 and 4, where the oscillation strength is determined by the offset of initial injection positions and angles of a laser pulse.

Chapter 6

OAM-radiation from plasma-based undulator/wiggler

A helical motion of an electron can generate high-order harmonic radiation carrying the well-defined OAM. In this chapter, the capability of a plasma-based undulator/wiggler for generating radiation carrying OAM (or so-called OAM-radiation) is presented. In Sec. 6.1, the basic theory of OAM-light is introduced. In Sec. 6.2, the tunability of the plasma-based undulator/wiggler proposed in Chapter. 3, 4 and 5 is discussed for the generation of OAM-radiation. Then, the OAM-radiation directly obtained from an electron undergoing the helical motion is theoretically and numerically calculated. In Sec. 6.3, the conclusion for this chapter is presented.

6.1 Light carrying OAM

A photon beam with the twisted phasefront can carry OAM [4, 17] and is capable of interacting with the particular atomic orbitals which are defined by the angular momentum in atoms [5], molecules [13], solid state systems [66] and plasma [84]. Radiation sources with known OAM enable the probing of the specific atomic structures. Applications of X-ray beams with internal OAM include probing quantum

optics [128], optical spanners[106], and crystalline structures [97].

It is known, that the angular momentum of a light beam is a vector quantity that demonstrates the rotation nature of the light and can be expressed as [63]

$$\boldsymbol{J} = \frac{1}{4\pi c}\int \boldsymbol{r} \times (\boldsymbol{E} \times \boldsymbol{B}) d^3\boldsymbol{r}, \tag{6.1}$$

where $\boldsymbol{r}$ is the position vector, $\boldsymbol{E}$ and $\boldsymbol{B}$ are electric and magnetic field respectively. Taking the definition of vector potential in Eq. (2.4) and Coulomb gauge in Eq. (2.10), the angular momentum can be re-written as [35]

$$\boldsymbol{J} = \frac{1}{4\pi c}\int (\boldsymbol{E} \times \boldsymbol{A}) d^3\boldsymbol{r} + \frac{1}{4\pi c}\int \sum_{j=x,y,z} E_j(\boldsymbol{r} \times \nabla) A_j d^3\boldsymbol{r}. \tag{6.2}$$

It can be seen that the angular momentum has been decomposed into two components. The first term on RHS of Eq. (6.2) is the spin angular momentum (SAM) which presents the rotation of $\boldsymbol{E}$ and $\boldsymbol{B}$ around the propagation direction and associates with its quantum spin and elliptical polarization. It is an intrinsic property of the light beam since it is independent of definition of coordinates system. Light with circular polarization carries $\sigma\hbar$ SAM per photon in a quantum mechanical picture where only two possible values for σ are $\sigma = -1$ and $\sigma = +1$ corresponding to left and right handed circular polarization around the propagation axis, respectively. The second term is the OAM which presents the spatial rotation of intensity and phase of the light beam around the axis of coordinate system. Therefore, a light beam with helical phasefront carries OAM, $l\hbar$ per photon where $l = 0, 1, 2, ...$, for example, Laguerre-Gaussian modes.

In quantum electrodynamics, the angular momentum operator $-i\hbar\partial/\partial\phi$ is azimuthally dependent. Now, by considering a short, weak, linearly polarized laser beam propagating in a parabolic plasma channel which is described by wave equation in Eq. (3.4), a general solution can be given in the form of Laguerre polynomials in

cylindrical coordinate (ρ, ϕ, z) as

$$\tilde{a}_{l,p}(\tau, \rho, \phi) = a_0 C_{lp} \left(\frac{\rho}{\sqrt{R}}\right)^{|l|} e^{-\rho^2/2R} L_p^{|l|}\left(\frac{\rho^2}{R}\right) e^{-i\omega\tau} e^{il\phi}, \tag{6.3}$$

where $C_{lp} = \sqrt{p!/[\pi R(p+|l|)!]}$ is the normalization coefficients, l is an integer and p is a non-negative integer and the frequency is $\omega = 1/(2M_{,(l,p)}) + (|l|+2p+1)/(M_{p,(l,p)}R)$. $L_\rho^{|l|}(\rho^2/R)$ is the Laguerre polynomial of p-th order with azimuthal mode index l. This solution presents the so-called Laguerre-Gaussian (LG) modes of the light beam. As seen from Eq. (6.3), LG mode carries the OAM of $l\phi$, presented by the phase term $e^{il\phi}$. This may provide a new possibility to manipulate the structure of the plasma wakefield, for example, twisted wakefield carrying OAM [120]. Note that there is no vertex at $l = 0$ as seen in Eq. (6.3), implying that the fundamental mode does not carry OAM.

It is shown in experiments that the exchanging of SAM and OAM with matter are equivalent in the light-matter interactions [106]. The possible physical evidence to distinguish them depends on whether the OAM and SAM terms are additive or subtractive.

6.2 OAM-radiation from plasma-based undulator

An electron can undergo a helical motion inside a plasma undulator. For example, the transverse oscillation of an electron is circular if both the injection conditions of the laser pulse in Eq. (3.12) and the electron in Eq. (3.28) are both matched as described in Chapter 3. In the case of HG-modes-driven plasma undulator, the circular motion is obtained by beating three different modes with the strength matching condition in Eq. (5.12) as described in Chapter 5. As a result, the normalized momentum of an

electron $\boldsymbol{u} = (u_x, u_x, u_z)$ is given in Cartesian coordinates $(\hat{e}_x, \hat{e}_y, \hat{e}_z)$ as

$$\begin{aligned} u_x =& -a_u \sin(\Omega\tau), \\ u_y =& \quad a_u \cos(\Omega\tau), \\ u_z =& \quad u_{z0}, \end{aligned} \tag{6.4}$$

and the position $\boldsymbol{r} = (x, y, z)$

$$\begin{aligned} x =& \quad \frac{a_u}{\gamma_0 \Omega} \cos\Omega\tau, \\ y =& \quad \frac{a_u}{\gamma_0 \Omega} \sin\Omega\tau, \\ z =& \quad \frac{u_{z0}\tau}{\gamma_0}, \end{aligned} \tag{6.5}$$

where a_u is the undulator strength, γ_0 is the initial Lorentz factor of electron and $u_{z0} = u_z(\tau = 0) = 0$ is the initial longitudinal normalized momentum. To mention that an electron can also undergo similar motion in Eq. (6.4) and (6.5) during the semi-steady stage of plasma resonant wiggler as discussed in Chapter 5.

The radiated field from moving charged particle is described by the Lienard-Wiechert potentials and the radiation intensity in an interaction duration T can be directly derived by Jackson's formula in Eq. (A.37)

$$\begin{aligned} \frac{d^2 I}{d\omega d\Omega} =& M \left| \int_{-T/2}^{T/2} d\tau e^{i\omega(\tau - \mathbf{n}\cdot\mathbf{r})} [\mathbf{n} \times (\mathbf{n} \times \boldsymbol{u})] \right|^2 \\ =& M \left| \boldsymbol{I}_x + \boldsymbol{I}_y + \boldsymbol{I}_z \right|^2, \end{aligned} \tag{6.6}$$

where $M = e^2\omega^2/(4\pi c\gamma_0^2)$ and $\boldsymbol{I}_x, \boldsymbol{I}_y, \boldsymbol{I}_z$ are components of the radition flux field in $\hat{x}, \hat{y}, \hat{z}$ direction respectively.

By transforming the trajectory in Eq. (6.4) and (6.5) into the spherical coordinate

$(\hat{e}_r, \hat{e}_\theta, \hat{e}_\phi)$,

$$\begin{bmatrix} \hat{e}_x \\ \hat{e}_y \\ \hat{e}_z \end{bmatrix} = \begin{pmatrix} \sin\theta\cos\phi & \cos\theta\cos\phi & -\sin\phi \\ \sin\theta\sin\phi & \cos\theta\sin\phi & \cos\phi \\ \cos\theta & -\sin\theta & 0 \end{pmatrix} \begin{bmatrix} \hat{e}_r \\ \hat{e}_\theta \\ \hat{e}_\phi \end{bmatrix},$$

and defining unit vector to observer in the radial direction $\boldsymbol{n} = \hat{e}_r$, it is straightforward to find that

$$\begin{aligned} \mathbf{n} \times (\mathbf{n} \times \boldsymbol{u}) = &- (u_x \cos\theta\cos\phi + u_y \cos\theta\sin\phi - u_z \sin\theta)\hat{e}_\theta \\ &- (-u_x \sin\phi + u_y \cos\phi)\hat{e}_\phi, \end{aligned} \tag{6.7}$$

and

$$\boldsymbol{n} \cdot \boldsymbol{r} = x\sin\theta\cos\phi + y\sin\theta\sin\phi + z\cos\theta. \tag{6.8}$$

Note that the radial component is zero, $\boldsymbol{I}_r = 0$. The phase term becomes

$$\omega(\tau - \mathbf{n}\cdot\mathbf{r}) = \omega\tau(1 - \beta_{z0}\cos\theta) + \alpha\sin\theta\sin(\phi - \Omega\tau - \frac{\pi}{2}), \tag{6.9}$$

where $\alpha = a_u\omega/(\gamma_0\Omega)$. The exponential term in Eq. (A.37) can be written in form of Bessel function as

$$e^{i\omega(\tau - \mathbf{n}\cdot\mathbf{r})} = \sum_{n=-\infty}^{\infty} J_n(\alpha\sin\theta) e^{i[\omega\tau(1-\beta_{z0}\cos\theta) + n(\phi - \Omega\tau - \pi/2)]}. \tag{6.10}$$

After some algebra, the two components $\boldsymbol{I}_\theta$ and $\boldsymbol{I}_\phi$ are calculated with Eqs. (6.7) and (6.10) by

$$
\begin{aligned}
\boldsymbol{I}_\theta = &- \int_{-T/2}^{T/2} d\tau \Big(a_u \cos\theta \sin(\phi - \Omega\tau) - u_{z0} \sin\theta \Big) \\
&\cdot \sum_{n=-\infty}^{\infty} J_n(\alpha \sin\theta) e^{i[\omega\tau(1-\beta_{z0}\cos\theta)+n(\phi-\Omega\tau-\pi/2)]} \\
&= \sum_{n=-\infty}^{\infty} J_n(\alpha \sin\theta) e^{-in\pi/2} \cdot T \\
&\cdot \left[i\frac{a_u}{2} \Big(e^{i(n+1)\phi} S_{n+1} - e^{i(n-1)\phi} S_{n-1} \Big) \cos\theta + u_{z0} S_n \sin\theta \right] \\
&= \sum_{n=-\infty}^{\infty} I_{n,\theta},
\end{aligned}
\tag{6.11}
$$

and

$$
\begin{aligned}
\boldsymbol{I}_\phi = &- \int_{-T/2}^{T/2} d\tau \Big(- u_x \sin\phi + u_y \cos\phi \Big) \\
&\cdot \sum_{n=-\infty}^{\infty} J_n(\alpha \sin\theta) e^{i[\omega\tau(1-\beta_{z0}\cos\theta)+n(\phi-\Omega\tau-\pi/2)]} \\
&= - \sum_{n=-\infty}^{\infty} J_n(\alpha \sin\theta) e^{-in\pi/2} \cdot \frac{a_u}{2} \\
&\cdot \Big(e^{i(n+1)\phi} S_{n+1} + e^{i(n-1)\phi} S_{n-1} \Big) \\
&= \sum_{n=-\infty}^{\infty} I_{n,\phi},
\end{aligned}
\tag{6.12}
$$

by defining the function $S_n = \mathrm{sinc}((\nu - n\Omega)T/2)$ and $\nu = \omega(1 - \beta_{z0}\cos\theta)$. The component for nth harmonic is denoted as $I_{n,\theta}$ and $I_{n,\phi}$. Now, by transforming the flux field $(0, I_\theta, I_\phi)$ into Cartesian coordinate by

$$
\begin{aligned}
I_{n,x} &= I_{n,\theta} \cos\theta \cos\phi - I_{n,\phi} \sin\phi, \\
I_{n,y} &= I_{n,\theta} \cos\theta \sin\phi + I_{n,\phi} \cos\phi, \\
I_{n,z} &= -I_{n,\theta} \sin\theta,
\end{aligned}
\tag{6.13}
$$

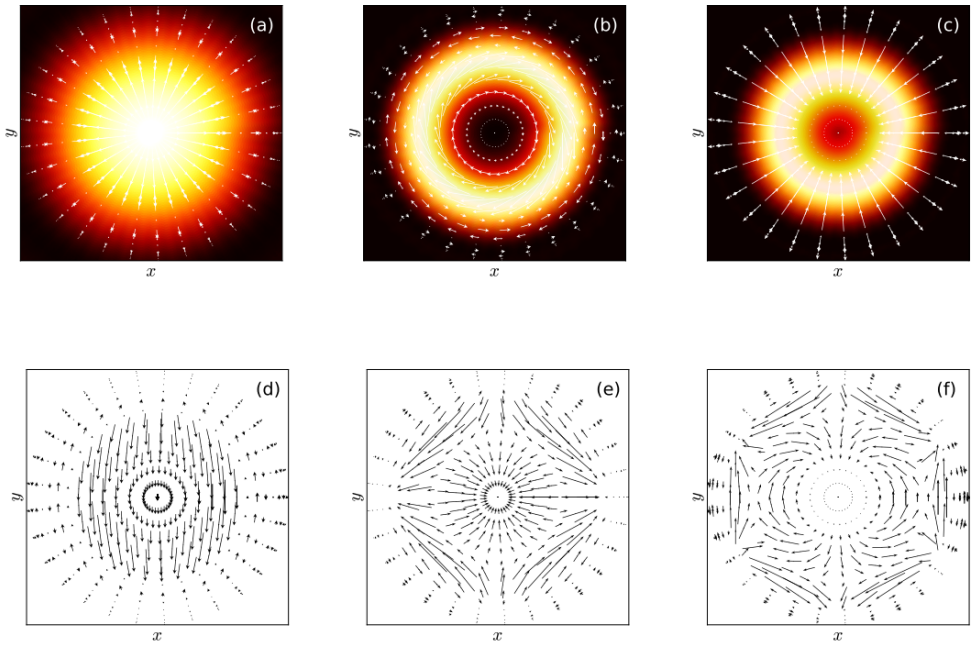

Figure 6.1: (a)-(c) show the intensity and transverse vector field (white arrows, $\vec{I}_\perp = I_{n+}\hat{e}_+ + I_{n-}\hat{e}_-$) of radiation for the fundamental ($n = 0$), second ($n = 1$) and third ($n = 2$) harmonics respectively in Eq. (6.17) and (6.18), viewed along z-axis; (d)-(f) show the corresponding rotation components.

one can easily get the transverse components as

$$\begin{aligned} I_{n,x} =& \frac{a_u}{2} e^{i(n+1)\phi} S_{n+1} \Big(i\cos^2\theta\cos\phi + \sin\phi \Big) \\ &+ \frac{a_u}{2} e^{i(n-1)\phi} S_{n-1} \Big(-i\cos^2\theta\cos\phi + \sin\phi \Big) \\ &+ \frac{u_{z0}}{2} S_n \cos\phi \sin 2\theta, \end{aligned} \tag{6.14}$$

and

$$\begin{aligned} I_{n,y} =& \frac{a_u}{2} e^{i(n+1)\phi} S_{n+1} \Big(i\cos^2\theta\sin\phi - \cos\phi \Big) \\ &+ \frac{a_u}{2} e^{i(n-1)\phi} S_{n-1} \Big(-i\cos^2\theta\sin\phi - \cos\phi \Big) \\ &+ \frac{u_{z0}}{2} S_n \sin\phi \sin 2\theta. \end{aligned} \tag{6.15}$$

For a better review of the vortex nature, one can also transform the transverse field into a rotation coordinate $\hat{e}_{\pm} = (\hat{e}_x \pm i\hat{e}_y)/\sqrt{2}$ along the longitudinal direction, as

$$\vec{I_n} = I_{n+}\hat{e}_+ + I_{n-}\hat{e}_- + I_{nz}\hat{e}_z, \tag{6.16}$$

where

$$\begin{aligned} I_{n+} =& \frac{1}{\sqrt{2}}(I_{n,x} - iI_{n,y}) \\ & \frac{1}{\sqrt{2}}\Big[iKS_{n+1}e^{in\phi}(2-\sin^2\theta) \\ & + iKS_{n-1}e^{i(n-2)\phi}\sin^2\theta + S_n e^{-i\phi}\sin 2\theta\Big], \end{aligned} \tag{6.17}$$

and

$$\begin{aligned} I_{n-} =& \frac{1}{\sqrt{2}}(I_{n,x} + iI_{n,y}) \\ & \frac{1}{\sqrt{2}}\Big[-iKS_{n-1}e^{in\phi}(2-\sin^2\theta) \\ & - iKS_{n+1}e^{i(n+2)\phi}\sin^2\theta + S_n e^{-i\phi}\sin 2\theta\Big]. \end{aligned} \tag{6.18}$$

The first two terms in RHS of Eqs. (6.17) and (6.18) contribute to the vortex field and the last term to the polarization. As shown in Fig. 6.1, the fundamental harmonic, in (a) and (d), does not display a vortex and therefore does not carry any OAM. However, the vorticity is clearly visible in the higher-order harmonics, for example, in (b), (c), (e) and (f), which then carry the OAM. Note that the field does not rotate for the even harmonic orders due to the compensation of last terms in the R.H.S of Eqs. (6.17) and (6.18), as shown in Fig. (6.1)(a) and (c).

6.3 Conclusion

In this chapter, the nature of a beam carrying OAM is discussed to show that angular momentum can be decomposed into two parts: SAM, which comes from electron spin or elliptical polarisation, and OAM, which comes from the vortex nature of intensity and phase distribution. An electron undergoing circular motion can emit OAM radiation. It is demonstrated that our proposed schemes of compact plasma undulators/wigglers can provide great flexibility to tune the polarisation of electron oscillation. This feature allows these schemes to generate well-defined OAM-radiation, and then to provide great potential for advanced applications demanding compact radiation sources, such as quantum communication or image recognition.

Chapter 7

Conclusions

This thesis aims to theoretically and numerically demonstrate the plasma-based compact high-energy radiation sources. They should be enable the generate the high-quality radiation competing with currently available 3^{rd} or even 4^{th} generation light sources. Three new schemes have been developed in the regime of linear and nonlinear plasma wakefields. Unlike the well-known betatron radiation, the proposed schemes are capable of providing a well-controlled radiation spectrum.

The starting point is motivated by the idea that an oscillation of a plasma wakefield can provide an extra driving force for an electron injected into a proper phase. Oscillation of the plasma wakefield is excited by the centroid oscillation of a laser pulse, which is guided inside a parabolic plasma density channel. As a result, an electron can undergo the combined motion of betatron and undulator oscillations in general. It is found that the intrinsic betatron oscillation could be totally removed if the injection conditions of an electron are approximately matched. This feature allows the generation of x-ray radiation with a very narrow bandwidth.

To extend the radiation spectrum to a high-energy region, such as γ-ray, and, at the same time, maintain high brightness, a resonant condition is found between the betatron oscillation of the injected electron and the centroid oscillation of the

laser pulse. This enables the generation of a bright γ-ray radiation even in a linear wakefield regime. The brightness is comparable to the 3^{rd} generation of conventional light sources.

Another scheme of a plasma undulator is also demonstrated, by beating several different HG modes. Surprisingly, a special structure of wakefield is produced, which is similar to the monochromatic sinusoidal field in a conventional undulator/wiggler, which leads to the x-ray radiation spectrum being further narrowed. This scheme is also capable of generating the synchrotron-like spectrum of γ-ray because of the wide tunable range of undulator strength.

An electron with circularly polarised transverse oscillation can generate OAM-radiation. Therefore, the flexible polarisation of the proposed schemes promises the potential of compact, high-energy OAM-radiation sources.

In the regime of a nonlinear wakefield with a more intense laser pulse, a stronger focusing and driving force is possible to accelerate and oscillate a much larger number of electrons. This might then generate a much better photon beam. However, throughout this thesis, attention has been given mainly to the linear wakefield regime, but rarely the nonlinear. In future, the nonlinear theory of plasma undulator will also be seriously considered with the new methods, such as variational methods, if needed.

Conversely, the LG mode carries OAM and can also be well-guided inside the plasma channel. The wakefield excitation shows that it is possible to transform its OAM to generate the structured wakefield. Such a wakefield carries OAM. This feature may benefit the generation of OAM-radiation with much better qualities than before. It is also a direction for future work.

Appendix A

Some basic concepts

A.1 Debye shielding

Due to the high plasma conductivity, an external DC electric field is shielded from the interior of a plasma. It is a dielectric phenomena in which plasma is polarized to prevent the penetration of the external field [53]. For a simple demonstration, we consider a quasi-neutral plasma with an initially uniform electron density n_0 and static ions. Of course, ions can also contribute to shielding but it is reasonable to be neglected due to the fact that ions are too heavy to move in comparison with electrons. Initially, the electrical potential in an equilibrium state is constant. Now, if a charge q is placed in such plasma, for example, at $\boldsymbol{r} = 0$, the perturbed potential $\delta\phi$ is given by Poisson's equation in Eq. (2.7a) with Coulomb gauge as

$$\nabla^2\delta\phi = -4\pi q\delta(\boldsymbol{r}) + 4\pi e(n_e - n_0), \tag{A.1}$$

where n_e is the electron density after perturbation. In the static limit $\boldsymbol{v}_{em} = \boldsymbol{0}$ and with the definition $\boldsymbol{E} = -\nabla\delta\phi$, the force equation in Eq. (2.19) is reduced to [75]

$$n_e e\nabla\delta\phi = -T_e\nabla n_e, \tag{A.2}$$

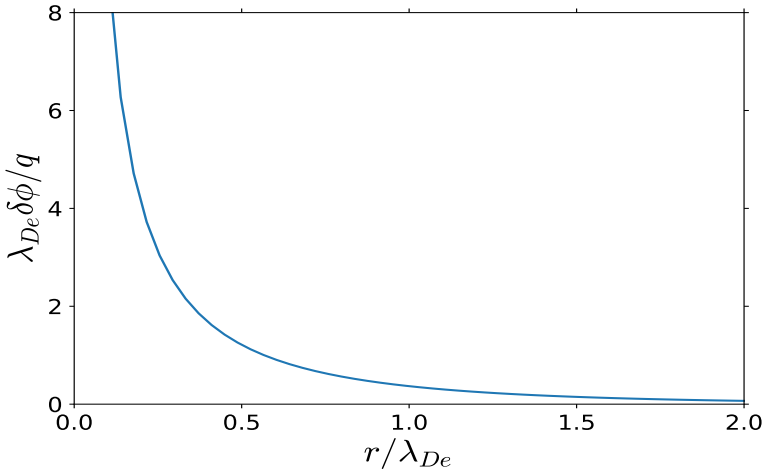

Figure A.1: Perturbed electrical potential due to a charge q placed in a quasi-neutral plasma.

where an isothermal equation of state $p_e = n_e T_e$ has been used. As a result, the electron density is given by

$$n_e = n_0 e^{\frac{e\delta\phi}{T_e}}. \tag{A.3}$$

By noting that $e\delta\phi/T_e \ll 1$, Eq. (A.3) can be expanded as

$$n_e \simeq n_0 \left(1 + \frac{e\delta\phi}{T_e}\right), \tag{A.4}$$

and substituted into Eq. (A.1), we obtain

$$\nabla^2\delta\phi - \frac{\delta\phi}{\lambda_{De}^2} = -4\pi q\delta(\boldsymbol{r}), \tag{A.5}$$

where the electron Debye length is defined as

$$\lambda_{De} = \sqrt{\frac{T_e}{4\pi n_0 e^2}} = 743 \cdot \sqrt{\frac{T_e[eV]}{n_0[cm^{-3}]}}, \tag{A.6}$$

and the solution is given by

$$\delta\phi = \frac{q}{r}\exp\left(\frac{-r}{\lambda_{De}}\right). \tag{A.7}$$

As shown in Fig. A.1, the extra field generated by the charge q is shielded out in a characteristic distance λ_{De}.

A.2 Optical guiding

Optical guiding of a laser pulse is based on the principle of refractive guiding. For example, relativistic optical guiding is achieved via the self-focusing effect of a laser beam [82] to compensate diffraction. The phase velocity of a laser pulse in plasma is given by

$$v_p = \frac{c}{\eta_r}, \tag{A.8}$$

where η_r is the refractive index of the laser pulse in plasma. If

$$\frac{\partial v_p}{\partial r} = -\frac{c}{\eta_r^2}\frac{\partial \eta_r}{\partial r} > 0, \tag{A.9}$$

and the condition

$$\frac{\partial \eta_r}{\partial r} < 0, \tag{A.10}$$

is satisfied, the on-axis phase velocity is less than off-axis which leads to the phase front curved backward and then focused. This is the so-called laser pulse self-guiding (or self-focusing). More precisely, the general expression of the refractive index of a laser pulse in plasma is given by [48]

$$\eta_r(r) \approx 1 - \frac{\omega_{p0}^2}{2\omega^2}\frac{n(r)}{n_0\gamma(r)}, \tag{A.11}$$

where $\gamma(r)$ is the relativistic factor of the plasma fluid, ω_{p0} is the electron plasma frequency evaluated at the ambient plasma density n_0. In the laser field the leading-

order motion of electron is the transverse quiver

$$\gamma \approx \gamma_\perp = (1 + a^2)^{1/2}, \tag{A.12}$$

and then the partial derivative of γ gives

$$\frac{\partial \gamma}{\partial r} = \frac{1}{\gamma_\perp} \frac{\partial a^2}{\partial r} > 0, \tag{A.13}$$

where $|a| = |\boldsymbol{a}_\perp|$. If a laser peaked on axis, e.g., for a transverse Gaussian laser pulse, this leads to the condition in Eq. (A.10) satisfied. Consequently, the laser pulse can be guided if its power P is above a critical power $P_c \simeq 17 M_p$[110]. Unfortunately, relativistic guiding is ineffective in preventing the diffraction of the laser pulse due to a finite transverse dimension of laser pulse.

A.3 Preformed plasma density channel guiding

According to Eq. (A.11), another contribution comes from the density profile, in the case that the minimum density is on axis. For example, considering a density profile in such form,

$$n = n_0 + \Delta n_p + \delta n. \tag{A.14}$$

Two parts of contribution are: 1) Δn_p, a preformed plasma density channel; 2) plasma density wave. In limits, $a^2 \ll 1$, $\Delta n_p / n_0 \ll 1$ and $\delta n / n_0 \ll 1$, the refractive index is given as [46]

$$\eta_r \approx 1 - \frac{\omega_{p0}^2}{2\omega^2} \big(1 - \frac{a^2}{2} + \frac{\Delta n_p}{n_0} + \frac{\delta n}{n_0}\big), \tag{A.15}$$

where three possible contributions include: 1) $-a^2/2$ is for relativistic self-guiding; 2) $\Delta n_p / n_0$ is for plasma density channel guiding; 3) $\delta n / n_0$ is for the self-channeling, plasma wave guiding and self-modulation of a long laser pulse.

One of the widely used tailored plasma profiles in the current experiments is the transverse parabolic plasma channel [107]. Considering a parabolic plasma channel in such form [48]

$$\Delta n_p = \Delta n \frac{r^2}{r_0^2}, \tag{A.16}$$

where r_0 is the laser pulse waist and Δn is the channel depth, then the refractive index of a Gaussian pulse,

$$|\hat{a}|^2 = a_0^2 \left(\frac{r_0}{r_s}\right)^2 e^{-\frac{2r^2}{r_s^2}}, \tag{A.17}$$

in such a channel is given as

$$\eta_r \approx 1 - \frac{\omega_{p0}^2}{2\omega^2}\left(1 + \frac{\Delta n}{n_0}\frac{r^2}{r_0^2}\right), \tag{A.18}$$

where r_s is the transverse spot size and a_0 is the amplitude of laser vector potential. As a result the pulse envelope evolves as

$$\frac{d^2R}{dz^2} = \frac{1}{Z_R^2 R^3}\left(1 - \frac{\Delta n}{\Delta n_c} R^4\right), \tag{A.19}$$

where $R = r_s/r_0$ and Δn_c is the critical plasma channel depth. It is seen from Eq. (A.19) that the laser pulse keeps constant if the condition

$$\Delta n_c = \frac{1}{\pi r_e r_0^2}, \tag{A.20}$$

is matched at the laser pulse waist $R = 1$, where $r_e = e/mc^2$ is the classical electron radius, and it scales as

$$\Delta n_c[cm^{-3}] = \frac{1.13 \times 10^{20}}{r_0^2[\mu m]}. \tag{A.21}$$

For initial conditions $dr_s/dz(z=0)=0$ and $r_s(z=0)=r_i$, a general solution of Eq. (A.19) is given as

$$2\frac{r_s^2}{r_i^2} = 1 + \frac{\Delta n_c r_0^4}{\Delta n r_i^4} + \left(1 - \frac{\Delta n_c r_0^4}{\Delta n r_i^4}\right)\cos(k_e z), \tag{A.22}$$

where $k_e = (2/Z_R)(\Delta n/\Delta n_c)^{1/2}$. The matching condition ($dr_s/dz = 0$) requires

$$\Delta n_c r_0^4 = \Delta n r_i^4. \tag{A.23}$$

For example, for a laser pulse focused at the injection position, $z = 0$, it requires

$$\Delta n_c = \Delta n \quad \text{and} \quad r_0 = r_i. \tag{A.24}$$

Therefore, the plasma channel profile is given as

$$n = n_0 + \Delta n_c \frac{r^2}{r_0^2}. \tag{A.25}$$

Otherwise, the laser pulse oscillates between

$$r_s^2 = r_i^2 \quad \text{and} \quad r_s^2 = \frac{\Delta n_c}{\Delta n}\frac{r_0^4}{r_i^2}. \tag{A.26}$$

A.4 Radiation from a moving charged particle

EM field emitted by a single charged particle q undergoing an arbitrary motion can be directly calculated by the Lienard-Wiechert potentials [63]

$$\Phi(\boldsymbol{r}, t) = \left[\frac{q}{(1 - \boldsymbol{n}\cdot\boldsymbol{\beta})R}\right]_{t_r}, \tag{A.27}$$

and

$$\boldsymbol{A}(\boldsymbol{r},t) = c\left[\frac{q\boldsymbol{\beta}}{(1-\boldsymbol{n}\cdot\boldsymbol{\beta})R}\right]_{t_r}, \tag{A.28}$$

where $\boldsymbol{\beta} = \boldsymbol{v}/c$ is the velocity of the charged particle, $\boldsymbol{n}$ is the unit vector along the relative distance $\boldsymbol{r} - \boldsymbol{r'}$ pointing in the direction of observer with $\boldsymbol{r'}$ is the trajectory of the particle, and $R = |\boldsymbol{r} - \boldsymbol{r'}|$ is the length of distance. The RHS of Eq. (A.27) and (A.28) are evaluated at the so-called retarded time

$$t' = t - \frac{R}{c}, \tag{A.29}$$

presenting the time when the radiation field is actually emitted from the particle. Note that this calculation was already formulated in 1898 before the advent of the special relativity theory. This is because once emitted, the electromagnetic waves propagate at it own spreed $\boldsymbol{v}_{rad}$ irrespective of the velocity of the charged particle $\boldsymbol{\beta}$. What the special relativity demonstrated is that the radiation field propagates in the constant spreed of light $v_{rad} = c$. That means the equations themselves are general. In a non-relativistic region, the radiation power only depends on the acceleration of charged particle, and is sufficient to be given by the Larmor's formula [65]

$$P_{\text{non-rel}} = \frac{2}{3}\frac{q^2}{c}|\dot{\boldsymbol{\beta}}|^2. \tag{A.30}$$

However, radiation power goes to significantly increase as the velocity of particle approaches to c. Then, Larmor's formula should be generalized to be valid for arbitary velocity of paricle and can be given as [63]

$$P = -\frac{2}{3}\frac{e^2}{m^2c^3}\left[\left(\frac{d\boldsymbol{p}}{d\tau}\right)^2 - \beta^2\left(\frac{dp}{d\tau}\right)^2\right] \tag{A.31}$$

where $p = |\boldsymbol{p}|$ is the amplitude of momentum of the particle, $\beta = |\boldsymbol{\beta}|$ and τ is the proper time following the particle trajectory. Therefore, in a linear acceleration,

$$\left(\frac{d\boldsymbol{p}}{d\tau}\right)^2 \simeq 0, \tag{A.32}$$

so,

$$P \simeq \frac{2}{3}\frac{e^2}{m^2c^3}\left(\frac{dp}{d\tau}\right)^2. \tag{A.33}$$

In a circular acceleration,

$$\frac{d\boldsymbol{p}}{d\tau} = \gamma\omega|\boldsymbol{p}| \quad \text{and} \quad \frac{dp}{d\tau} = 0, \tag{A.34}$$

then,

$$P = \frac{2}{3}\frac{e^2c}{\rho^2}\beta^4\gamma^4. \tag{A.35}$$

It is seen that the circular acceleration (or, transverse oscillation) is much more sufficient for the radiation generation. It is also the reason why the circular accelerators for electrons are problematic.

Furthermore, in highly relativistic region, radiation occurs primarily along the direction of velocity $\boldsymbol{\beta}$ within an angular spread of order $\theta = 1/\gamma$ and the radiation frequency is subjected to strong Doppler shift which benefits for generation of high energy radiation, e.g. hard x-ray generation [67]. Since the power radiated by a particle on an surface is the flux of the Poynting vector $\boldsymbol{S} = \boldsymbol{E} \times \boldsymbol{B}$, angular distribution of radiated power is then given as [63]

$$\frac{d^2P}{d\Omega} = (\boldsymbol{S} \cdot \boldsymbol{n})(1 - \boldsymbol{n} \cdot \boldsymbol{\beta})R^2, \tag{A.36}$$

where $\boldsymbol{E}$ and $\boldsymbol{B}$ are the electric and magnetic fields of the radiation from the Lienard-Wiechert potentials in Eq. (A.27) and (A.28). By assuming an observer in the far

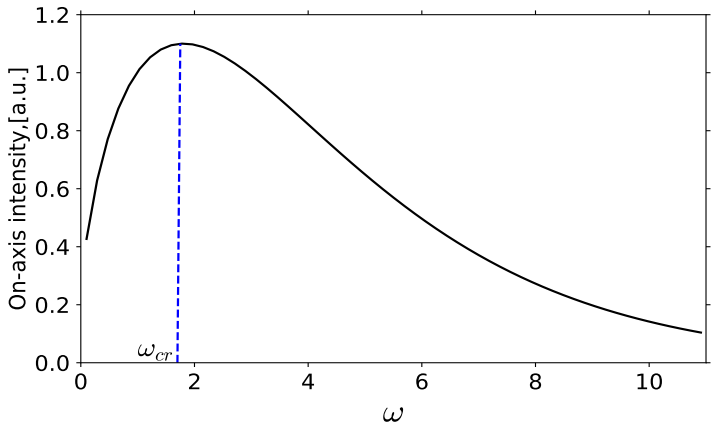

Figure A.2: On-axis intensity of synchrotron radition spectrum. The dash blue line shows the position of critical frequency where the intensity is maiximum.

field, total energy radiated per frequency ω per solid angle Ω, during the interaction time T, is calculated by

$$\frac{d^2I}{d\omega d\Omega} = 2|\boldsymbol{A}(\omega)|^2 = \frac{e^2\omega^2}{4\pi^2 c}\left|\int_{-T/2}^{T/2} dt e^{i\omega(t-\mathbf{n}\cdot\mathbf{r}'/c)}[\mathbf{n}\times(\mathbf{n}\times\boldsymbol{\beta})]\right|^2, \tag{A.37}$$

where $\boldsymbol{A}(\omega)$ is the Fourier transforming from Eq. (A.28) as

$$\boldsymbol{A}(\omega) = \frac{1}{\sqrt{2\pi}}\int_{-\infty}^{+\infty} dt\ e^{i\omega t}\boldsymbol{A}(t) \tag{A.38}$$

It is seen from Eq. (A.37) that the radiation is determined by the electron's trajectory. Considering an single electron undergoing a circular motion which is usually the case in bending magnet of the storage ring, the angular acceleration induces the synchrotron radiation emerging tangentially to the curvature of the beam. The on-axis intensity of synchrotron radition spectrum is shown in Fig. A.2. Such radiation is characterized by a critical frequency

$$\omega_{cr} = \frac{3eB\gamma^2}{2m}, \tag{A.39}$$

where B is the amplitude of the magnetic field, γ is the Lorentz factor of electron and m is the electron mass.

Appendix B

Derivation of dynamics of plasma undulator in a parabolic plasma channel

B.1 Laser pulse guiding

Dynamics of a laser pulse in a plasma channel can be studied by solving the simple Schrödinger wave equation in Eq. (3.4) with assumptions in Sec. 3.1. With the harmonic potential in Eq. (3.5), x-component of the corresponding force can be written as

$$\langle F_x \rangle = -\langle \frac{\partial V}{\partial x} \rangle = -M_p \Omega^2 \langle x \rangle = \frac{d}{d\tau} \langle p_x \rangle , \tag{B.1}$$

where $\langle p_x \rangle$ is the x-component of momentum and $\langle x \rangle$ is the expectation value of position corresponding to the laser pulse center. Generally, an expectation value of an operator $\hat{O}$ is defined as

$$\langle \hat{O} \rangle = \langle \tilde{a}_\perp | \hat{O} | \tilde{a}_\perp \rangle = \frac{\int_{-\infty}^{\infty} \tilde{a}_\perp^* \, \hat{O} \, \tilde{a}_\perp dxdy}{\int_{-\infty}^{\infty} \tilde{a}_\perp^* \, \tilde{a}_\perp dxdy}, \tag{B.2}$$

$\tilde{a}_\perp^*$ presents the complex conjugation of $\tilde{a}_\perp$. With the momentum equation,

$$\frac{d}{d\tau}\langle x\rangle = \frac{1}{m}\langle p_x\rangle\,, \tag{B.3}$$

and its second derivative with respect to time

$$\frac{d^2}{d\tau^2}\langle x\rangle = \frac{1}{m}\frac{d}{d\tau}\langle p_x\rangle = -\frac{1}{m}\langle\frac{\partial V}{\partial x}\rangle = -\Omega^2\langle x\rangle\,, \tag{B.4}$$

dynamic equation of the laser pulse center is

$$\frac{d^2}{d\tau^2}\langle x\rangle + \Omega^2\langle x\rangle = 0. \tag{B.5}$$

Its solution is directly given in Eq. (3.8). The evolution of the laser pulse spot size $\sigma_x = \langle x^2\rangle - \langle x\rangle^2$ can be studied by using Ehrenfest's theorem [16] which is given for the expectation value of an operator $\hat{O}$ as

$$\frac{d}{d\tau}\langle\hat{O}\rangle = \frac{i}{\hbar}\langle[\hat{H},\hat{O}]\rangle + \langle\frac{\partial\hat{O}}{\partial\tau}\rangle\,, \tag{B.6}$$

where $\hat{H}$ is Hamiltonian of the system in Eq. (3.4). Firstly, we consider the operators $\hat{O} = x^2$ and $\hat{O} = xp_x + p_x x$,

$$\frac{d}{d\tau}\langle x^2\rangle = \frac{i}{\hbar}\langle[\hat{H},x^2]\rangle + \langle\frac{\partial x^2}{\partial\tau}\rangle = \frac{1}{2i\hbar M_p}\langle x^2, p_x^2\rangle = \frac{1}{M_p}\langle xp_x + p_x x\rangle\,, \tag{B.7}$$

and

$$\frac{d}{d\tau}\langle xp_x + p_x x\rangle = \frac{i}{\hbar}\langle[\hat{H}, xp_x + p_x x]\rangle = \frac{2}{M_p}\langle p_x^2\rangle - 2M_p\Omega^2\langle x^2\rangle\,. \tag{B.8}$$

Together with Eqs. (B.3), (B.7) and (B.8), the transverse spotsize of the laser pulse is given as

$$\frac{d\sigma_x}{d\tau} = \frac{d}{d\tau}\left\langle x^2\right\rangle - \frac{d}{d\tau}\left\langle x\right\rangle^2 = \frac{1}{M_p}\left\langle xp_x + p_x x\right\rangle - \frac{2}{M_p}\left\langle x\right\rangle\left\langle p_x\right\rangle = \frac{2}{M_p^2}\sigma_{p_x} - 2\Omega^2\sigma_x, \quad \text{(B.9)}$$

where divergence of momentum is defined by $\sigma_{p_x} = \left\langle p_x^2\right\rangle - \left\langle p_x\right\rangle^2$. As a result, the evolution equation of the laser pulse transverse spot size can be written as

$$\frac{d^2\sigma_x}{d\tau^2} + 2\Omega^2\sigma_x = 2\Omega^2\frac{\sigma_{p_x}}{M_p^2\Omega^2}. \quad \text{(B.10)}$$

Similarly, we can also get the equation for σ_{p_x} as

$$\frac{d^2}{d\tau^2}\left(\frac{\sigma_{p_x}}{M_p^2\Omega^2}\right) + 2\Omega^2\frac{\sigma_{p_x}}{M_p^2\Omega^2} = 2\Omega^2\sigma_x. \quad \text{(B.11)}$$

From Eqs. (B.10) and (B.11), one can see that

$$\frac{d^2}{d\tau^2}\left(\sigma_x + \frac{\sigma_{p_x}}{M_p^2\Omega^2}\right) = 0, \quad \text{(B.12)}$$

and give

$$\sigma_x + \frac{\sigma_{p_x}}{M_p^2\Omega^2} = const. = \sigma_{x,0} + \frac{\sigma_{p_x,0}}{M_p^2\Omega^2}, \quad \text{(B.13)}$$

where $\sigma_{x,0} = \sigma_x(\tau = 0)$ and $\sigma_{p_x,0} = \sigma_{p_x}(\tau = 0)$ are initial values of spot size and divergence. From Eqs. (B.10) and (B.11), one can also arrive at

$$\frac{d^2}{d\tau^2}\left(\sigma_x - \frac{\sigma_{p_x}}{M_p^2\Omega^2}\right) + 4\Omega^2\left(\sigma_x - \frac{\sigma_{p_x}}{M_p^2\Omega^2}\right) = 0, \quad \text{(B.14)}$$

which has the solution

$$\sigma_x - \frac{\sigma_{p_x}}{M_p^2\Omega^2} = \left(\sigma_{x,0} - \frac{\sigma_{p_x,0}}{M_p^2\Omega^2}\right)\cos 2\Omega\tau + \frac{1}{M_p\Omega}\left(\left\langle xp_x + p_x x\right\rangle_0 - \left\langle x\right\rangle_0\left\langle p_x\right\rangle_0\right)\sin 2\Omega\tau. \quad \text{(B.15)}$$

From Eqs. (B.13) and (B.15), one can have the solution of transverse spot size and momentum divergence of laser pulse as

$$\begin{aligned}\sigma_x =&\frac{\sigma_{x0}}{2}+\frac{\sigma_{p_x,0}}{2M_p^2\Omega^2}+\left(\frac{\sigma_{x0}}{2}-\frac{\sigma_{p_x,0}}{2M_p^2\Omega^2}\right)\cos 2\Omega\tau \\ &+\frac{1}{M_p\Omega}\left(\frac{\langle xp_x+p_xx\rangle_0}{2}-\langle x\rangle_0\langle p_x\rangle_0\right)\sin 2\Omega\tau,\end{aligned} \tag{B.16}$$

and

$$\begin{aligned}\sigma_{p_x} =&\frac{\sigma_{x0}}{2}+\frac{\sigma_{p_x,0}}{2M_p^2\Omega^2}-\left(\frac{\sigma_{x0}}{2}-\frac{\sigma_{p_x,0}}{2M_p^2\Omega^2}\right)\cos 2\Omega\tau \\ &-\frac{1}{M_p\Omega}\left(\frac{\langle xp_x+p_xx\rangle_0}{2}-\langle x\rangle_0\langle p_x\rangle_0\right)\sin 2\Omega\tau,\end{aligned} \tag{B.17}$$

where $\langle xp_x+p_xx\rangle_0$ and $\langle x\rangle_0\langle p_x\rangle_0$ denote their initial values.

B.2 Dynamics of a single electron

With laser centroid trajectory given in Eq. (3.14) and assumptions declared in Sec. 3.3, the solution for equation of transverse motion for a single electron Eq. (3.24) can be given as [25]

$$\vec{r_e}=\boldsymbol{r}_{e,0}\cos\Omega_\beta\tau+\frac{\boldsymbol{u}_{\perp,0}}{\gamma_0\Omega_\beta}\sin\Omega_\beta\tau+\boldsymbol{r}_{e,s}, \tag{B.18}$$

where $\mathbf{r}_{\perp,\mathbf{0}}=(x_0,y_0)$ and $\mathbf{u}_{\perp,0}=(u_{x,0},u_{y,0})$ are the vectors of initial electron transverse coordinates and momenta components respectively, and $\boldsymbol{r}_{e,s}$ is the special solution for this equation as

$$\boldsymbol{r}_{e,s}=\Omega_\beta\int_0^\tau d\tau'\boldsymbol{r}_c(\tau')\ \sin\Omega_\beta(\tau-\tau'). \tag{B.19}$$

From the momentum equation,

$$\begin{aligned}\boldsymbol{u}_\perp &= -\gamma_0 \frac{d\boldsymbol{r}_e}{d\tau} = \gamma_0 \boldsymbol{r}_{e,0}\Omega_\beta \sin\Omega_\beta\tau + \boldsymbol{u}_{\perp,0}\cos\Omega_\beta\tau + \gamma_0 \frac{d\boldsymbol{r}_{e,s}}{d\tau} \\ &= -\gamma_0 \boldsymbol{r}_{e,0}\Omega_\beta \sin\Omega_\beta\tau + \boldsymbol{u}_{\perp,0}\cos\Omega_\beta\tau + \gamma_0\Omega_\beta^2 \int_0^\tau d\tau' \boldsymbol{r}_c(\tau')\ \cos\Omega_\beta(\tau-\tau'),\end{aligned} \tag{B.20}$$

and after some straightforward algebras, it gives

$$\begin{aligned}\boldsymbol{u}_\perp &= -\gamma_0 \boldsymbol{r}_{e,0}\Omega_\beta \sin\Omega_\beta\tau + \boldsymbol{u}_{\perp,0}\cos\Omega_\beta\tau \\ &- \frac{a_u}{\gamma_0}\frac{\Omega_\beta}{\Omega}\frac{1}{2}(\boldsymbol{\epsilon}+\boldsymbol{\epsilon}^\star)\sin\Omega_\beta\tau + \frac{a_u}{\gamma_0}\frac{i}{2}(\boldsymbol{\epsilon}-\boldsymbol{\epsilon}^\star)\cos\Omega_\beta\tau - \frac{a_u}{\gamma_0}\frac{i}{2}(\boldsymbol{\epsilon}e^{i\Omega\tau} - \boldsymbol{\epsilon}^\star e^{-i\Omega\tau}) \\ &= -\left[\frac{a_u\Omega_\beta}{\Omega}\left(\frac{\boldsymbol{\epsilon}+\boldsymbol{\epsilon}^*}{2}\right) + \gamma_0\Omega_\beta \mathbf{r}_{\perp,\mathbf{0}}\right]\sin\Omega_\beta\tau + \left[\mathbf{u}_{\perp,0} + a_u\left(\frac{i\boldsymbol{\epsilon}-i\boldsymbol{\epsilon}^*}{2}\right)\right]\cos\Omega_\beta\tau \\ &- a_u\left[\frac{i\boldsymbol{\epsilon}e^{i\Omega\tau} - i\boldsymbol{\epsilon}^* e^{-i\Omega\tau}}{2}\right],\end{aligned} \tag{B.21}$$

where undulator strength a_u is defined in Eq. (3.27).

B.3 Evolution of an electron beam

Dynamics of an electron beam can be studied by envelope equation of the beam which can be directly obtained from the equation of motion for a single electron in Eq. (3.24). For a cylindrical-symmetric beam, both situations in $\hat{x}$ and $\hat{y}$ direction are the same. For example, in $\hat{x}$ direction,

$$\ddot{x}x + \Omega_\beta^2 x^2 = \Omega_\beta^2 x_c x, \tag{B.22}$$

where the time-derivative is denoted by up-dot, for example, $d^2x/d\tau^2 = \ddot{x}$, and x_c presents the laser pulse center in $\hat{x}$ direction. Here, with the definition of RMS spread

of transverse beam size and momentum for n particles

$$\sigma_{b,x}^2 = \langle x^2 \rangle - \langle x \rangle^2 = \frac{1}{n} \sum_{i=1}^{n} \Big(x_i - \langle x \rangle \Big)^2, \tag{B.23}$$

and

$$\sigma_{b,\dot{x}}^2 = \langle \dot{x}^2 \rangle - \langle \dot{x} \rangle^2 == \frac{1}{n} \sum_{i=1}^{n} \Big(\dot{x}_i - \langle \dot{x} \rangle \Big)^2, \tag{B.24}$$

and

$$\sigma_{b,x,\dot{x}}^2 = \langle (x - \langle x \rangle)(\dot{x} - \langle \dot{x} \rangle) \rangle \,, \tag{B.25}$$

where x_i and $\dot{x}_i$ present the position and momentum of ith electron inside the beam, it is easily to find the relation

$$\frac{d\sigma_{b,x}}{d\tau} = \frac{d}{d\tau} \sqrt{\frac{1}{n} \sum_{i=1}^{n} \Big(x_i - \langle x \rangle \Big)} = \frac{\sigma_{b,x,\dot{x}}^2}{\sigma_{b,x}}. \tag{B.26}$$

By considering an cylindrical-symmetric on-axis electron beam injected into the plasma channel where

$$\langle x \rangle = \frac{1}{n} \sum_{i=1}^{n} x_i = 0 \text{ and } \langle \dot{x} \rangle = \frac{1}{n} \sum_{i=1}^{n} \dot{x}_i = 0, \tag{B.27}$$

then Eqs. (B.23) and (B.24) become

$$\sigma_{b,x}^2 = \frac{1}{n} \sum_{i=1}^{n} (x_i)^2 = \langle x_i^2 \rangle \,, \tag{B.28}$$

and

$$\sigma_{b,\dot{x}}^2 = \frac{1}{n} \sum_{i=1}^{n} (\dot{x}_i)^2 = \langle \dot{x}_i^2 \rangle \,. \tag{B.29}$$

On the other hand, since

$$\begin{aligned}\frac{d}{d\tau}\langle x\dot{x}\rangle &= \frac{d}{d\tau}\left(\frac{1}{n}\sum_{i=1}^{n} x_i\dot{x}_i\right)\\ &= \frac{1}{n}\sum_{i=1}^{n}(\dot{x}_i^2 + x_i\ddot{x}_i)\\ &= \sigma_{b,\dot{x}}^2 - \Omega_\beta^2\sigma_{b,x}^2 + \Omega_\beta^2\langle x_c x\rangle,\end{aligned} \tag{B.30}$$

and

$$\begin{aligned}\frac{d}{d\tau}\langle x\dot{x}\rangle &= \frac{d}{d\tau}\left(\frac{1}{n}\sum_{i=1}^{n} x_i\dot{x}_i\right)\\ &= \frac{d}{d\tau}\left(\frac{1}{2n}\sum_{i=1}^{n}\frac{dx_i^2}{d\tau}\right)\\ &= \frac{1}{2}\frac{d^2}{d\tau^2}\langle x^2\rangle = \frac{1}{2}\frac{d^2\sigma_{b,x}^2}{d\tau^2}\\ &= \frac{d}{d\tau}\left(\sigma_{b,x}\dot{\sigma}_{b,x}\right)\\ &= \sigma_{b,x}\ddot{\sigma}_{b,x} + \frac{\sigma_{x\dot{x}}^2}{\sigma_{b,x}},\end{aligned} \tag{B.31}$$

where the relation in Eqs. (B.22) and (B.26) has been used. As a result, from Eqs. (B.30) and (B.31), we can obtain the envelope equation of an electron beam inside the plasma undulator as

$$\frac{d^2\sigma_{b,x}}{d\tau} + \Omega_\beta^2\sigma_{b,x} - \frac{\epsilon_{b,x}^2}{\sigma_{b,x}^2} = \frac{1}{\sigma_{b,x}}\left(\Omega_\beta^2\langle x_c x\rangle - \Omega_\beta^2\langle x\rangle^2 + \langle x\rangle\langle\ddot{x}\rangle\right), \tag{B.32}$$

where emittance in $\hat{x}$ direction is defined as

$$\epsilon_{b,x} = \sqrt{\sigma_{b,x}^2\sigma_{b,\dot{x}}^2 - \sigma_{b,x,\dot{x}}^4}. \tag{B.33}$$

By using the trajectory of the laser pulse and electron in $\hat{x}$ direction

$$x = (x_0 + \frac{a_u}{\gamma_0 \Omega_u}) \cos \Omega\tau + \frac{u_{u0}}{\gamma_0 \Omega_\beta} \sin \Omega_\beta \tau + \frac{a_u}{\gamma_0 \Omega_u} \cos \Omega_u \tau, \tag{B.34}$$

and

$$x_c = x_{c0} \cos \Omega_u \tau, \tag{B.35}$$

we get

$$\begin{aligned} &\langle x_c x \rangle = x_c \langle x \rangle , \\ &\langle x \rangle = \left(\langle x_0 \rangle + \frac{a_u}{\gamma_0 \Omega_u} \right) \cos \Omega_\beta \tau + \frac{\langle u_{x0} \rangle}{\gamma_0 \Omega_u} \sin \Omega_\beta \tau - \frac{a_u}{\gamma_0 \Omega_u} \cos \Omega_u \tau, \\ &\langle \ddot{x} \rangle = -\Omega_\beta^2 \langle x \rangle + (\Omega_u^2 - \Omega_\beta^2) \frac{a_u}{\gamma_0 \Omega_u} \cos \Omega_u \tau. \end{aligned} \tag{B.36}$$

By inserting these equations into Eq. (B.32), the RHS term becomes 0. Therefore, envelope equation of the electron beam in $\hat{x}$-direction is given as

$$\frac{d^2 \sigma_{b,x}}{d\tau} + \Omega_\beta^2 \sigma_{b,x} - \frac{\epsilon_{b,x}^2}{\sigma_{b,x}^2} = 0, \tag{B.37}$$

which is the same case as pure betatron oscillation of an electron beam [47]. It means that the undulator driving force does not contribute to the envelope evolution. The envelope equation of an electron beam in $\hat{y}$ direction can be treated exactly in the same way as

$$\frac{d^2 \sigma_{b,y}}{d\tau} + \Omega_\beta^2 \sigma_{b,y} - \frac{\epsilon_{b,y}^2}{\sigma_{b,y}^2} = 0, \tag{B.38}$$

where the emittance in $\hat{y}$ direction is defined as

$$\epsilon_{b,y} = \sqrt{\sigma_{b,y}^2 \sigma_{b,\dot{y}}^2 - \sigma_{b,y,\dot{y}}^4} \, . \tag{B.39}$$

A simulation is profermed with a single Gaussian laser pulse by using VDSR [32].

Laser pulse		
a_0	0.2	
x_{c0}	0.475	
w_0	1.33	
Electron Beam		
	UnMatched	Matched
Q	1.0pC	1.0pC
$x_{\perp,0}$	0.04	0.04
γ_0	1000	1000
$\Delta\gamma_0/\gamma_0$	2.0%	2.0%
$\sigma_{b,x,0}$	0.0295	0.0477
$\varepsilon_{b,x,n}$	0.0118	0.019

Table B.1: VDSR simulation parameters for beam dynamics in plasma undulator

The simulation parameters are summarized in the Table. B.1. The laser pulse is injected with the guiding condition in Eq. (3.12) and the center of a spatial Gaussian electron beam is configured with the conditions in Eq. (3.30).

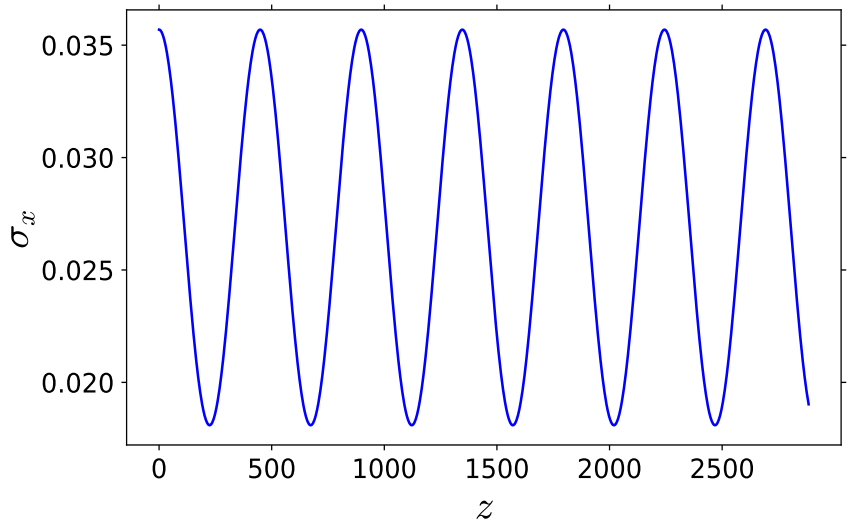

Figure B.2: 2D VDSR simulation result of evolution of transverse RMS spot size of the electron beam in Fig. (B.1).

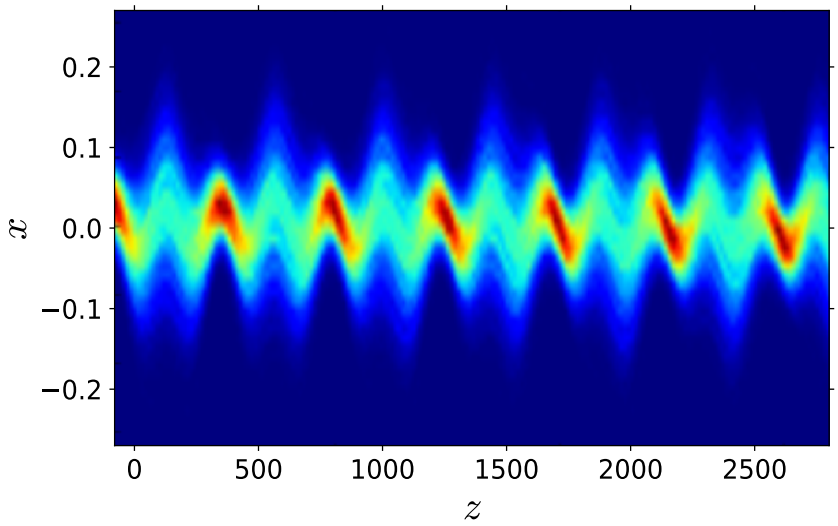

Figure B.1: 2D VDSR simulation result of the general dynamics for an electron beam with the spatial Gaussian distribution as propagating inside the plasma channel undulator field. The color shows the charge density inside the beam. It shows a strong envelope oscillation as shown in Fig. (B.2).

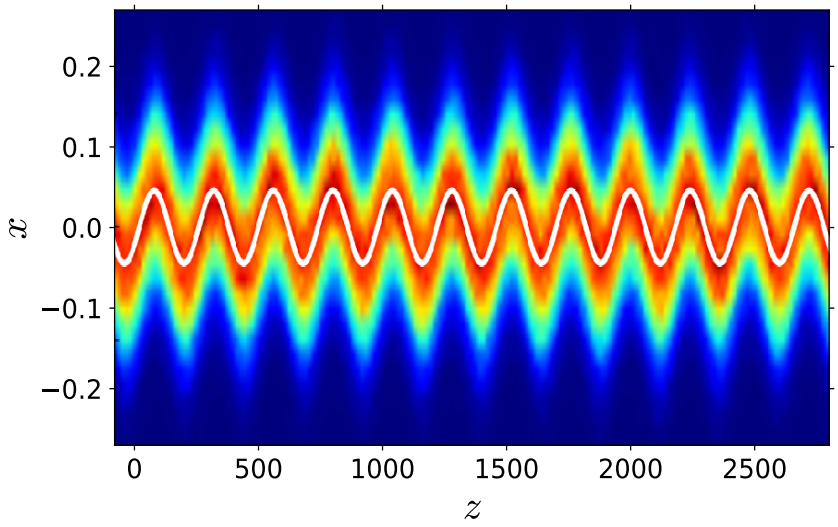

Figure B.3: 2D VDSR simulation result of the dynamics for an electron beam and initial matching condition $\sigma_{b,x,0} = \sigma_{b,x,m}$ as propagating inside the plasma channel undulator field. The color shows the charge density inside the beam. It shows that the envelope keeps constant as shown in Fig. (B.4). The white solid line shows the centroid trajectory of the electron beam agreeing with the solution in Eq. (3.29).

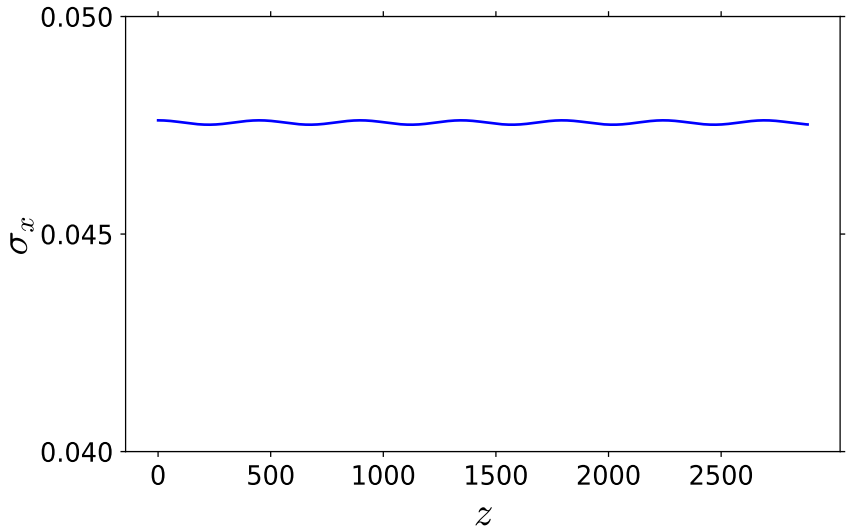

Figure B.4: 2D VDSR simulation result of evolution of transverse RMS spot size of the electron beam in Fig. (B.3).

Appendix C

Derivation of resonant dynamics equation for a single electron in 2D undulator field

The momentum equation is given for a relativistic electron($\gamma_0 \gg 1$) inside an electric field,

$$\frac{d\mathbf{u}}{d\tau} = -\mathbf{E}, \tag{C.1}$$

where the normalized momentum $\mathbf{u} = \mathbf{p}/m_e c = \gamma d\mathbf{r}/d\tau = \gamma\boldsymbol{\beta}$ and $\boldsymbol{\beta} = \boldsymbol{v}/c$ is the normalized velocity of an electron. For 2D case in $\hat{x}\hat{z}$-plane, equation of transverse motion of the electron can be written as

$$\frac{du_x}{d\tau} = \frac{d(\gamma\beta_x)}{d\tau} = \beta_x\frac{d\gamma}{d\tau} + \gamma\frac{d\beta_x}{d\tau} = -E_x, \tag{C.2}$$

With the relation

$$\frac{dx}{d\tau} \equiv \beta_x = \frac{u_x}{\gamma}, \tag{C.3}$$

the second derivative of transverse position is then given as

$$\frac{d^2x}{d\tau^2} = \frac{d}{d\tau}\left(\frac{u_x}{\gamma}\right) = \frac{1}{\gamma}\frac{du_x}{d\tau} - \frac{u_x}{\gamma^2}\frac{d\gamma}{d\tau}. \tag{C.4}$$

The energy gain equation of an electron in the wakefield is given as [46]

$$\frac{d\gamma}{d\tau} = -\beta_g(\boldsymbol{\beta}\cdot\boldsymbol{E}) = -\beta_g(\beta_z E_z + \beta_x E_x), \tag{C.5}$$

where β_g is the group velocity of the laser pulse inside the wakefield, and equals to the phase velocity of plasma wave, β_{ph}. It approximately equals to unity, $\beta_g \simeq 1$, in a linear plasma wakefield [42]. Together with Eqs. (C.2), (C.4) and (C.5), the equation of motion for a single electron inside a 2D electric field is given as

$$\frac{d^2x}{d\tau} + \frac{E_x}{\gamma}\left(\frac{dx}{d\tau}\right)^2 - \frac{\beta_z E_z}{\gamma}\frac{dx}{d\tau} + \frac{E_x}{\gamma} = 0. \tag{C.6}$$

By assuming that the longitudinal motion dominates here,

$$\beta_x = dx/d\tau \ll \beta_z \simeq 1, \tag{C.7}$$

the second term in Eq. (C.6) becomes very small and can be neglected. Therefore, Eq. (C.6) becomes

$$\frac{d^2x}{d\tau^2} - \frac{E_z}{\gamma}\frac{dx}{d\tau} + \frac{E_x}{\gamma} = 0, \tag{C.8}$$

where the second term may give the damping effect depending on the longitudinal wakefield.

From Eq. (C.5), the energy evolution is then given as

$$\gamma(\xi) \simeq \gamma_0 - \int_0^\tau E_z(\tau')d\tau', \tag{C.9}$$

where γ_0 is the initial gamma factor of the electron and the energy gain from transverse acceleration $\beta_x E_x$ has been neglected with the condition in Eq. (C.7). By considering a wide laser pulse ($|r_m| \gg |x - x_c|$), the energy gain is then given by using the wakefield in Eq. (4.2)

$$\gamma = \gamma_0(1 + R_\delta \tau), \tag{C.10}$$

where the energy gain rate is defined as

$$R_\delta = -\frac{r_m^2 \Omega_\beta^2 \cos\xi}{4}. \tag{C.11}$$

It is easily seen that the energy gain occurs inside the phase $-(2n+1)\pi < \xi < -(2n+1/2)\pi$ of the wakefield, where n is a non-negative integer. Together with Eqs. (C.8), (C.10) and the transverse wakefield in Eq. (4.3), the transverse equation of motion for a single electron is given as

$$\frac{d^2x}{d\tau^2} + \frac{R_\delta}{1 + R_\delta \tau}\frac{dx}{d\tau} + \frac{\Omega^2}{\mu(1 + R_\delta \tau)}\, x = \frac{x_{c0}\Omega^2}{\mu(1 + R_\delta \tau)} \cos(\Omega\tau), \tag{C.12}$$

where $\mu = -\mu_0/\sin\xi$ with $\mu_0 = \Omega^2/\Omega_\beta^2$, presents the resonance status at the local phase ξ. Note that the equation does not include the singularity point ($\tau = -1/R_\delta$) since $\tau > 0$ in the acceleration phase inside the wakefield.

Now, by introducing a new variable

$$s = \frac{2Q_f}{\mu}\sqrt{1 + \frac{\Omega\tau}{Q_f}}, \tag{C.13}$$

where $Q_f = \Omega/R_\delta$ presents the initial quality factor of the oscillation, the equation of motion in Eq. (C.12) becomes

$$\frac{d^2x}{ds^2} + \frac{1}{s}\,\frac{dx}{ds} + x = g(s), \tag{C.14}$$

it is a time-dependent damping oscillation with extra driving force

$$g(s) = x_{c0}\cos(\frac{\mu}{4Q_f}s^2 - Q_f). \tag{C.15}$$

A general solution of Eq. (C.14) consists of two parts: homogeneous $x_h(s)$ and particular $x_p(s)$ solutions ,

$$x(s) = x_h(s) + x_p(s). \tag{C.16}$$

Firstly, to solve the homogeneous equation of Eq. (C.14),

$$\frac{d^2x}{ds^2} + \frac{1}{s}\frac{dx}{ds} + x = 0, \tag{C.17}$$

the general solution is given in the form of Bessel functions

$$x_h(s) = c_1 J_0(s) + c_2 Y_0(s), \tag{C.18}$$

where c_1 and c_2 are constants, and $J_0(s)$ and $Y_0(s)$ are zero-order of the first and second kinds of Bessel functions, respectively. By inserting the solution in Eq. (C.18) into homogeneous equation in Eq. (C.17) with the initial conditions, the constants c_1 and c_2 are found by

$$\begin{cases} c_1 = -\frac{x_0 Y_{10} + u_{x0} Y_{00}}{W_0} \\ c_2 = \frac{x_0 J_{10} + u_{x0} J_{00}}{W_0} \end{cases}$$

where $x_0 = x(\tau = 0)$ and $u_{x0} = u_x(\tau = 0)$, $W_0 = W(\tau = 0)$ are initial conditions of the injected electron. $W(s) = det(M(s))$ is the Wronskian of Bessel functions $J_0(s)$

and $Y_0(s)$ with the matrix M defined as

$$M = \begin{pmatrix} -Y_1(s) & -Y_0(s) \\ J_1(s) & J_0(s) \end{pmatrix}.$$

Secondly, to find a particular solution by assuming the variation of parameters in the homogeneous solution in Eq. (C.18), a general form can be then written as [25]

$$x_p(s) = \nu_1(s)J_0(s) + \nu_2(s)Y_0(s), \tag{C.19}$$

with an imposed condition

$$v_1' J_0 + v_2' Y_0 = 0. \tag{C.20}$$

By inserting the solution in Eq. (C.19) and the condition in Eq. (C.20) into Eq. (C.14), we could get

$$\begin{cases} \nu_1(s) = -\int_{s_0}^{s} \frac{Y_0(s')g(s')}{W(s')} ds', \\ \nu_2(s) = \int_{s_0}^{s} \frac{J_0(s')g(s')}{W(s')} ds'. \end{cases}$$

Finally, the general solution for the Eq. (C.14) is given as

$$x(s) = x_h(s) + x_p(s) = (c_0 + \nu_1(s))J_0(s) + (c_2 + \nu_2(s))Y_0(s). \tag{C.21}$$

Appendix D

Derivation of dynamics of high-order HG laser modes in parabolic plasma channel

D.1 HG modes guiding in a parabolic plasma channel

The equation governing the dynamics of 2D slowly-varying envelope $\tilde{a}_\perp(\tau, \boldsymbol{r})$ of the laser pulse inside the parabolic plasma channel is given in Eq. (3.4). By assuming that the transverse wave vector $\tilde{a}_\perp$ can be separated into two parts of temporal and spatial components as

$$\tilde{a}(\tau, \boldsymbol{r}) = T(\tau)A(\boldsymbol{r}), \tag{D.1}$$

then, the wave equation in Eq. (3.4) becomes

$$\frac{\partial T}{\partial \tau} = -i\lambda T \tag{D.2}$$

$$\Big(-\frac{\nabla_\perp^2}{2M_p} + V(\boldsymbol{r}) \Big) A = \lambda A, \tag{D.3}$$

where λ is a constant to be determined. The time-dependent solution is easily given as

$$T(\tau) = a_0 e^{-i\lambda\tau}, \tag{D.4}$$

where a_0 is the amplitude of the laser pulse. For the spatial part in Eq. (D.3) of 2D case, where $\nabla_\perp = \partial_x$, the equation can be rewritten as

$$\frac{\partial^2 A}{\partial x^2} + (2M_p\lambda - 1)A - \frac{x^2}{R^2}A = 0, \tag{D.5}$$

where the potential in Eq. (3.5) is applied. By defining a new variable

$$\tilde{x} = \frac{x}{\sqrt{R}}, \tag{D.6}$$

the equation in Eq. (D.5) becomes

$$\frac{\partial^2 A}{\partial \tilde{x}^2} - \tilde{x}^2 A = -\alpha A, \tag{D.7}$$

where $\alpha = (2M_p\lambda - 1)R$. Since the equation

$$\frac{\partial^2 \tilde{A}}{\partial \tilde{x}^2} - \tilde{x}^2 \tilde{A} = -\tilde{A}, \tag{D.8}$$

has the solution

$$\tilde{A}(\tilde{x}) = Ce^{-\frac{\tilde{x}^2}{2}}, \tag{D.9}$$

with a constant C, the solution for Eq. (D.5) can be generally given as

$$A(\tilde{x}) = \tilde{A}(\tilde{x})H(\tilde{x}), \tag{D.10}$$

where $H(\tilde{x})$ is an arbitrary function to be determined. By substituting Eq. (D.10) into Eq. (D.7), it is easily to find such relation

$$\frac{\partial^2 H}{\partial \tilde{x}^2} - 2\tilde{x}\frac{\partial H}{\partial \tilde{x}} + (\alpha - 1)H = 0. \tag{D.11}$$

It is seen that if we let

$$\alpha - 1 = 2n, \tag{D.12}$$

where n is an integer, $H(\tilde{x})$ is actually the Hermite function of n^{th} order [116],

$$H(\tilde{x}) = H_n(\tilde{x}). \tag{D.13}$$

Therefore, the solution for Eq. (D.5) can be written as

$$A_n(x) = Ce^{-\frac{x^2}{2R}} H_n(\frac{x}{\sqrt{R}}), \tag{D.14}$$

with normalization condition

$$\int_{-\infty}^{+\infty} |A_n(x)|^2 dx = 1, \tag{D.15}$$

which gives the constant

$$C = \frac{1}{\sqrt{2^n n!}}. \tag{D.16}$$

Further, since

$$\alpha = 2n + 1 = (2M_p\lambda - 1)R, \tag{D.17}$$

the wavelength is then found as

$$\lambda = \frac{1}{2M_p} + \frac{n + 1/2}{M_p R}. \tag{D.18}$$

Finally, together with Eqs. (D.4) and (D.14), the solution for the paraxial wave equation in 2D case is given as

$$\tilde{a}(\tau, x) = T(\tau)A(x) = a_0 e^{-i(\frac{1}{2M_p} + \frac{n+1/2}{M_p R})\tau} \frac{1}{\sqrt{2^n n!}} e^{-\frac{x^2}{2R}} H_n(\frac{x^2}{2R}). \tag{D.19}$$

For 3D case, where $\nabla_\perp = (\partial_x, \partial_y)$ and $r^2 = x^2 + y^2$ in the harmonic potential in Eq. (3.5), the equation in Eq. (D.3) becomes

$$(\partial_x^2 - \frac{x^2}{R^2})A + (\partial_y^2 - \frac{y^2}{R^2})A = -(2M_p\lambda - 1)A, \tag{D.20}$$

It can be separated into two equations same as Eq. (D.7)

$$(R^2\partial_x^2 - x^2)A = -\alpha_x A \tag{D.21}$$

$$(R^2\partial_y^2 - y^2)A = -\alpha_y A, \tag{D.22}$$

with the constants defined as

$$\alpha_x = j(2M_p\lambda - 1)R, \tag{D.23}$$

$$\alpha_y = (1 - j)(2M_p\lambda - 1)R. \tag{D.24}$$

Following the same treatment of 2D case, the solution of 3D the paraxial wave equation in Eq. (3.4) is given by

$$\tilde{a}(\tau, \boldsymbol{r}) = a_0 \frac{1}{\sqrt{2^{n_x+n_y} n_x! n_y!}} e^{-i(\frac{1}{2M_p} + \frac{n_x+n_y+1}{M_p R})\tau} e^{-\frac{x^2+y^2}{2R}} H_{n_x}(\frac{x^2}{2R}) H_{n_y}(\frac{y^2}{2R}), \tag{D.25}$$

where n_x and n_y are integer and the numbers of modes in $\hat{x}$ and $\hat{y}$ direction respectively.

D.2 Intensity oscillation

In the case of the superposition of various HG modes, due to the difference in the phase velocity, the intensity profile $I = a_\perp(\tau, x, y, \zeta)a_\perp(\tau, x, y, \zeta)^*$ will contain interference terms and can lead to the oscillatory structure which is dependent on the mode numbers. Such oscillation can be seen on Fig. D.1, where the integrated transverse intensity profile of the superposition of the mixture of modes with identical M_p, propagating along the plasma channel is demonstrated for three cases: 1) superposition of two laser modes with $\{m = 0,\ n = 0,\ a = 0.4,\ \varphi = 0\}$ and $\{m = 1,\ n = 0,\ a = 0.05,\ \varphi = 0\}$ (subfigure (a)); 2) superposition of two laser modes with $\{m = 0,\ n = 0,\ a = 0.4,\ \varphi = 0\}$ and $\{m = 3,\ n = 0,\ a = 0.05,\ \varphi = 0\}$ (subfigure (b)); 3) superposition of three laser modes with $\{m = 0,\ n = 0,\ a = 0.4,\ \varphi = 0\}$, $\{m = 1,\ n = 0,\ a = 0.05,\ \varphi = 0\}$ and $\{m = 0,\ n = 1,\ a = 0.05,\ \varphi = \pi/2\}$ (subfigure (c)). The latter case can be also viewed as the superposition of a Gaussian mode and a first order Laguerre-Gaussian mode in the case of which only two pulses are required. In cases 1) and 2), the oscillation is linear in $\hat{x}\hat{z}$ plane. In case 3), the oscillation is helical. One can see a behaviour that is very similar to the case of a single Gaussian laser pulse injected in the parabolic channel with some initial centroid displacement or under a small angle with respect to the channel axis, which is discussed in details in Chapter 3 and 4. From Eq. (5.1), one can also find that by choosing different mode numbers, amplitudes, phases, and wavelengths, one can create oscillatory behavior of the propagating laser pulse with different periods and amplitudes. Ellipticity of the trajectory of the laser pulse centroid can be controlled by the phase difference of the laser modes, as can be seen on Fig. D.1(c). This provides an easy control of the polarization of the plasma channel undulator based on higher-order laser modes.

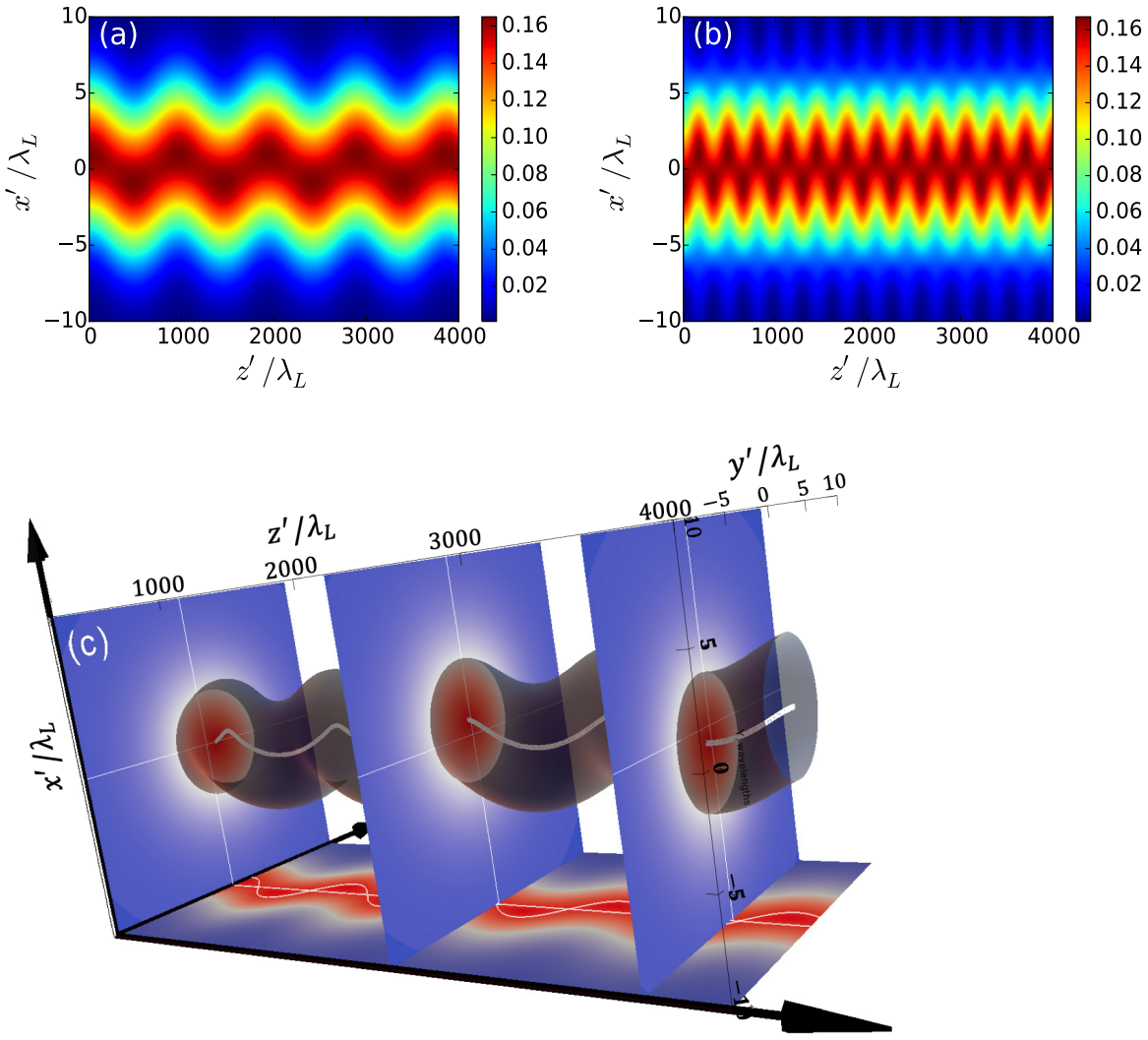

Figure D.1: Integrated transverse intensity profile of laser pulse as a function of propagation distance Z'/λ_L for (a) a fundamental mode plus a first-order HG mode; (b) a fundamental mode plus a third-order HG mode; (c) a fundamental mode plus two first-order HG modes.

D.3 Dephasing effect

To consider the effect of phase slippage for dynamics of an electron in the wakefield in Eq. (5.10), we can write down the longitudinal electric field generated by two modes $\{m = 0, n = 0, a = a_0\}$ and $\{m = 1, n = 0, a = a_1\}$,

$$E_z = -\frac{\partial \phi}{\partial \xi} = E_0 x \cos\xi \cos\Omega\tau. \tag{D.26}$$

It is seen that the longitudinal field is linearly dependent on the transverse coordinates and leads to instability of the beam dynamics. Therefore, it is better to have the injected electron beam tightly focused initially. By solving the momentum equation in $\hat{z}$-direction, the longitudinal trajectories of the electron beam can be given with the phase slippage as

$$u_z \approx u_{z0} - \frac{E_0 x \sin\Omega\tau}{\Omega} \sin(\zeta + \Delta\zeta), \tag{D.27}$$

where the phase slippage $\Delta\xi$ is approximately given as [46]

$$\Delta\zeta \approx (\beta_e - \beta_p)\tau \tag{D.28}$$

with $\beta_p \approx 1 - 1/M_p$ is the phase velocity of plasma wave, $\beta_e \approx 1$ the longitudinal speed of the electron. It is seen that there is no acceleration on axis if the condition in Eq. (5.12) is satisfied. In the case of low plasma density and tightly focused electron beam considered where $M_p \gg 1$, the dephasing effect can be neglected for a short propagation distance in comparison with the dephasing length $L_d \approx 2\pi M_p^2$ [46], and then $u_z \approx u_{z0}$ for the injection phase $\zeta = -3\pi/2$.

Bibliography

[1] The structure of some crystals as indicated by their diffraction of x-rays. *Proceedings of the Royal Society of London A: Mathematical, Physical and Engineering Sciences*, 89(610):248–277, 1913.

[2] A. Abrami et al. Medical applications of synchrotron radiation at the syrmep beamline of elettra. *Nuclear Instruments and Methods in Physics Research Section A: Accelerators, Spectrometers, Detectors and Associated Equipment*, 548(1):221 – 227, 2005. Proceedings of he 4th International Workshop on Medical Applications of Synchrotron Radiation.

[3] E. Allaria et al. Two-colour pumpprobe experiments with a twin-pulse-seed extreme ultraviolet free-electron laser. 4:2476, 2013.

[4] L. Allen, M. W. Beijersbergen, R. J. C. Spreeuw, and J. P. Woerdman. Orbital angular momentum of light and the transformation of laguerre-gaussian laser modes. *Phys. Rev. A*, 45:8185–8189, Jun 1992.

[5] M. F. Andersen, C. Ryu, Pierre Cladé, Vasant Natarajan, A. Vaziri, K. Helmerson, and W. D. Phillips. Quantized rotation of atoms from photons with orbital angular momentum. *Phys. Rev. Lett.*, 97:170406, Oct 2006.

[6] D. Anderson and M. Bonnedal. Variational approach to nonlinear selffocusing of gaussian laser beams. *The Physics of Fluids*, 22(1):105–109, 1979.

[7] N.E. Andreev, V.E. Baranov, B. Cros, V.E. Fortov, S.V. Kuznetsov, G. Maynard, and P. Mora. Electron bunch compression and acceleration in the laser wakefield. *Nuclear Instruments and Methods in Physics Research Section A: Accelerators, Spectrometers, Detectors and Associated Equipment*, 653(1):66 – 71, 2011. Superstrong 2010.

[8] I. a. Andriyash, Ph Balcou, and V. T. Tikhonchuk. Collective properties of a relativistic electron beam injected into a high intensity optical lattice. *The European Physical Journal D*, 65(3):533–540, dec 2011.

[9] I. a. Andriyash, E. D'Humières, V. T. Tikhonchuk, and Ph. Balcou. Betatron emission from relativistic electrons in a high intensity optical lattice. *Physical Review Special Topics - Accelerators and Beams*, 16(10):100703, oct 2013.

[10] I.A. Andriyash, R. Lehe, A. Lifschitz, C. Thaury, J.-M. Rax, K. Krushelnick, and V. Malka. An ultracompact X-ray source based on a laser-plasma undulator. *Nature Communications*, 5:4736, aug 2014.

[11] U. Arp, C. W. Clark, A. P. Farrell, E. Fein, M. L. Furst, and E. W. Hagley. Synchrotron ultraviolet radiation facility surf iii. *Review of Scientific Instruments*, 73(3):1674–1676, 2002.

[12] David Attwood. *Soft X-Rays and Extreme Ultraviolet Radiation: Principles and Applications*. Cambridge University Press, 1999.

[13] M. Babiker, C. R. Bennett, D. L. Andrews, and L. C. Dávila Romero. Orbital angular momentum exchange in the interaction of twisted light with molecules. *Phys. Rev. Lett.*, 89:143601, Sep 2002.

[14] A. Bacci, F. Broggi, C. DeMartinis, D. Giove, C. Maroli, V. Petrillo, A.R. Rossi, L. Serafini, P. Tomassini, L. Cultrera, G. Di Pirro, M. Ferrario, D. Filippetto, G. Gatti, E. Pace, C. Vaccarezza, C. Vicario, F. Bosi, D. Giulietti, L.a. Gizzi, and P. Oliva. Status of Thomson source at SPARC/PLASMONX. *Nuclear Instruments and Methods in Physics Research Section A: Accelerators, Spectrometers, Detectors and Associated Equipment*, 608(1):S90–S93, sep 2009.

[15] Ph Balcou. Proposal for a Raman X-ray free electron laser. *The European Physical Journal D*, 59(3):525–537, sep 2010.

[16] Leslie E Ballentine. *Quantum Mechanics: A Modern Development*. World Scientific Publishing, 2nd edition, 2014.

[17] Stephen M. Barnett and L. Allen. Orbital angular momentum and nonparaxial light beams. *Optics Communications*, 110(5):670 – 678, 1994.

[18] D. F. Bartlett, P. E. Goldhagen, and E. A. Phillips. Experimental test of coulomb's law. *Phys. Rev. D*, 2:483–487, Aug 1970.

[19] D. Bauer, P. Mulser, and W. H. Steeb. Relativistic ponderomotive force, uphill acceleration, and transition to chaos. *Phys. Rev. Lett.*, 75:4622–4625, Dec 1995.

[20] S. Bellucci, S. Bini, V. Biryukov, Yu. Chesnokov, S. Dabagov, G. Giannini, V. Guidi, Yu. Ivanov, V. Kotov, V. Maisheev, C. Malagù, G. Martinelli, a. Petrunin, V. Skorobogatov, M. Stefancich, and D. Vincenzi. Experimental Study for the Feasibility of a Crystalline Undulator. *Physical Review Letters*, 90(3):034801, jan 2003.

[21] Donald H Bilderback, Pascal Elleaume, and Edgar Weckert. Review of third and next generation synchrotron light sources. *Journal of Physics B: Atomic, Molecular and Optical Physics*, 38(9):S773, 2005.

[22] J. A. Bittencourt. *Fundamentals of Plasma Physics*. Springer-Verlag New York, 3rd edition, 2004.

[23] J. Bordas. *Research Facilities for Biology at the Synchrotron Radiation Source at Daresbury Laboratory*. Springer US, Boston, MA, 1989.

[24] A. B. Borisov, A. V. Borovskiy, O. B. Shiryaev, V. V. Korobkin, A. M. Prokhorov, J. C. Solem, T. S. Luk, K. Boyer, and C. K. Rhodes. Relativistic and charge-displacement self-channeling of intense ultrashort laser pulses in plasmas. *Phys. Rev. A*, 45:5830–5845, Apr 1992.

[25] William E. Boyce, Richard C. DiPrima, and Douglas B. Meade. *Elementary Differential Equations and Boundary Value Problems*. Wiley, 11th ed. edition, 2017.

[26] Alain J. Brizard. A new lagrangian formulation for laser-plasma interactions. *Physics of Plasmas*, 5(4):1110–1117, 1998.

[27] M. Bussmann, H. Burau, T. E. Cowan, A. Debus, A. Huebl, G. Juckeland, T. Kluge, W. E. Nagel, R. Pausch, F. Schmitt, U. Schramm, J. Schuchart, and R. Widera. Radiative signatures of the relativistic kelvin-helmholtz instability. In *Proceedings of the International Conference on High Performance Computing, Networking, Storage and Analysis*, SC '13, pages 5:1–5:12, New York, NY, USA, 2013. ACM.

[28] M. Bussmann, H. Burau, T. E. Cowan, A. Debus, A. Huebl, G. Juckeland, T. Kluge, W. E. Nagel, R. Pausch, F. Schmitt, U. Schramm, J. Schuchart, and R. Widera. Radiative signatures of the relativistic kelvin-helmholtz instability. In *Proceedings of the International Conference on High Performance Computing, Networking, Storage and Analysis*, SC '13, pages 5:1–5:12, New York, NY, USA, 2013. ACM.

[29] Davide Castelvecchi. Next-generation x-ray source fires up. *Nature*, 525:15–16, 2015.

[30] Masud Chaichian, Ioan Merches, Daniel Radu, and Anca Tureanu. *Electrodynamics*. Springer spectrum, 2016.

[31] Chao Chang, Chuanxiang Tang, and Juhao Wu. High-Gain Thompson-Scattering X-Ray Free-Electron Laser by Time-Synchronic Laterally Tilted Optical Wave. *Physical Review Letters*, 110(6):064802, feb 2013.

[32] M. Chen, E. Esarey, CGR Geddes, C. Schroeder, G. Plateau, S. Bulanov, S. Rykovanov, and W. Leemans. Modeling classical and quantum radiation from laser-plasma accelerators. *Physical Review Special Topics - Accelerators and Beams*, 16(3):030701, mar 2013.

[33] S Cipiccia et al. Gamma-rays from harmonically resonant betatron oscillations in a plasma wake. *Nature Physics*, 7:867–871, 2011.

[34] James A. Clarke. *The Science and Technology of Undulators and Wigglers*. Oxford university press, 2004.

[35] Gilbert Grynberg Claude Cohen-Tannoudji, Jacques Dupont-Roc. *Photons and Atoms: Introduction to Quantum Electrodynamics*. Wiley, 2007.

[36] S. Corde, K. Ta Phuoc, G. Lambert, R. Fitour, V. Malka, A. Rousse, A. Beck, and E. Lefebvre. Femtosecond x rays from laser-plasma accelerators. *Rev. Mod. Phys.*, 85:1–48, Jan 2013.

[37] S Corde, C Thaury, a Lifschitz, G Lambert, K Ta Phuoc, X Davoine, R Lehe, D Douillet, a Rousse, and V Malka. Observation of longitudinal and transverse self-injections in laser-plasma accelerators. *Nature communications*, 4:1501, jan 2013.

[38] E. Cormier-Michel, E. Esarey, C. G. R. Geddes, C. B. Schroeder, K. Paul, P. J. Mullowney, J. R. Cary, and W. P. Leemans. Control of focusing fields in laser-plasma accelerators using higher-order modes. *Physical Review Special Topics - Accelerators and Beams*, 14(3):031303, mar 2011.

[39] John M. Dawson. Nonlinear electron oscillations in a cold plasma. *Phys. Rev.*, 113:383–387, Jan 1959.

[40] John M. Dawson. Particle simulation of plasmas. *Rev. Mod. Phys.*, 55:403–447, Apr 1983.

[41] A. D. Debus, M. Bussmann, M. Siebold, A. Jochmann, U. Schramm, T. E. Cowan, and R. Sauerbrey. Traveling-wave Thomson scattering and optical undulators for high-yield EUV and X-ray sources. *Applied Physics B*, 100(1):61–76, may 2010.

[42] C. D. Decker and W. B. Mori. Group velocity of large-amplitude electromagnetic waves in a plasma. *Phys. Rev. E*, 51:1364–1375, Feb 1995.

[43] DESY. Petra iii, 2016.

[44] F. Dorchies, F. Amiranoff, V. Malka, J. R. Marqus, A. Modena, D. Bernard, F. Jacquet, Ph. Min, B. Cros, G. Matthieussent, P. Mora, A. Solodov, J. Morillo, and Z. Najmudin. Acceleration of injected electrons in a laser wakefield experiment. *Physics of Plasmas*, 6(7):2903–2913, 1999.

[45] Brian J. Duda and W. B. Mori. Variational principle approach to short-pulse laser-plasma interactions in three dimensions. *Phys. Rev. E*, 61:1925–1939, Feb 2000.

[46] E. Esarey, C. B. Schroeder, and W. P. Leemans. Physics of laser-driven plasma-based electron accelerators. *Rev. Mod. Phys.*, 81:1229–1285, Aug 2009.

[47] E. Esarey, B. A. Shadwick, P. Catravas, and W. P. Leemans. Synchrotron radiation from electron beams in plasma-focusing channels. *Phys. Rev. E*, 65:056505, May 2002.

[48] E. Esarey, P. Sprangle, J. Krall, and A. Ting. Self-focusing and guiding of short laser pulses in ionizing gases and plasmas. *IEEE Journal of Quantum Electronics*, 33(11):1879–1914, Nov 1997.

[49] E. Esarey, P. Sprangle, J. Krall, A. Ting, and G. Joyce. Optically guided laser wakefield acceleration*. *Physics of Fluids B: Plasma Physics*, 5(7):2690–2697, 1993.

[50] Eric Esarey and Mark Pilloff. Trapping and acceleration in nonlinear plasma waves. *Physics of Plasmas*, 2(5):1432–1436, 1995.

[51] Esmaeil Eslami and Saeedeh Afhami. External injection and acceleration of electron bunch in front of the plasma wakefield produced by a periodic chirped laser pulse. *Physics of Plasmas*, 24(1):013110, 2017.

[52] J Faure, Y Glinec, A Pukhov, S Kiselev, S Gordienko, E Lefebvre, J-P Rousseau, F Burgy, and V Malka. A laserplasma accelerator producing monoenergetic electron beams. *Nature*, 431(September):541–544, 2004.

[53] Richard Fitzpatrick. *Plasma Physics: An Introduction*. CRC Press, 2014.

[54] G. Fubiani, E. Esarey, C. B. Schroeder, and W. P. Leemans. Beat wave injection of electrons into plasma waves using two interfering laser pulses. *Phys. Rev. E*, 70:016402, Jul 2004.

[55] C. G. R. Geddes, Cs. Toth, J. van Tilborg, E. Esarey, C. B. Schroeder, J. Cary, and W. P. Leemans. Guiding of relativistic laser pulses by preformed plasma channels. *Phys. Rev. Lett.*, 95:145002, Sep 2005.

[56] C.G.R. Geddes, C. Toth, J. Van Tilborg, E. Esarey, C.B. Schroeder, D. Bruhwiler, C. Nieter, J. Cary, and W.P. Leemans. High-quality electron beams from a laser wakefield accelerator using plasma-channel guiding. *Nature*, 431(September):538–541, 2004.

[57] R.J. Goldston and P.H. Rutherford. *Introduction to Plasma Physics*. CRC Press, 1995.

[58] A. J. Gonsalves, T. P. Rowlands-Rees, B. H. P. Broks, J. J. A. M. van der Mullen, and S. M. Hooker. Transverse interferometry of a hydrogen-filled capillary discharge waveguide. *Phys. Rev. Lett.*, 98:025002, Jan 2007.

[59] L. Gorbunov, P. Mora, and T. M. Antonsen, Jr. Magnetic Field of a Plasma Wake Driven by a Laser Pulse. *Physical Review Letters*, 76(14):2495–2498, apr 1996.

[60] D.J. Griffiths. *Introduction to electrodynamics*. Prentice, 2013.

[61] Z-H He, B Hou, J A Nees, J H Easter, J Faure, K Krushelnick, and A G R Thomas. High repetition-rate wakefield electron source generated by few-millijoule, 30 fs laser pulses on a density downramp. *New Journal of Physics*, 15(5):053016, may 2013.

[62] Tetsuya Ishikawa et al. A compact x-ray free-electron laser emitting in the sub-ngstrm region. 6:540, 2012.

[63] J.D. Jackson. *Classical electrodynamics*. Wiley, New York, NY, 3rd ed. edition, 1999.

[64] Phillips JC, J C Phillips, Wlodawer A, A Wlodawer, Yevitz MM, M M Yevitz, Hodgson KO, and K O Hodgson. Applications of synchrotron radiation to protein crystallography: preliminary results. *PMC*, 73:128–32.

[65] J.Larmor, D.Sc., and F.R.S. Lxiii. on the theory of the magnetic influence on spectra; and on the radiation from moving ions. *The London, Edinburgh, and Dublin Philosophical Magazine and Journal of Science*, 44(271):503–512, 1897.

[66] Roeland Juchtmans and Jo Verbeeck. Orbital angular momentum in electron diffraction and its use to determine chiral crystal symmetries. *Phys. Rev. B*, 92:134108, Oct 2015.

[67] Masaki Kando, Timur Zh. Esirkepov, James K. Koga, Alexander S. Pirozhkov, and Sergei V. Bulanov. Coherent, short-pulse x-ray generation via relativistic flying mirrors. *Quantum Beam Science*, 2(2), 2018.

[68] Martijn Kemerink, Tom J. Dierichs, Julien Dierichs, Hubert Huynen, Joachim E. Wildberger, Jos M. A. van Engelshoven, and Gerrit J. Kemerink. The application of x-rays in radiology: From difficult and dangerous to simple and safe. *American Journal of Roentgenology*, 198:128–32.

[69] A. G. Khachatryan, A. Irman, F. A. van Goor, and K.-J. Boller. Femtosecond electron-bunch dynamics in laser wakefields and vacuum. *Phys. Rev. ST Accel. Beams*, 10:121301, Dec 2007.

[70] A. G. Khachatryan, F. A. van Goor, K.-J. Boller, A. J. W. Reitsma, and D. A. Jaroszynski. Extremely short relativistic-electron-bunch generation in the laser wakefield via novel bunch injection scheme. *Phys. Rev. ST Accel. Beams*, 7:121301, Dec 2004.

[71] S Kneip et al. Bright spatially coherent synchrotron x-rays from a table-top source. *Nature Physics*, 6:980–983, 2010.

[72] Vladimir Kogan, Klaus Bethke, and Roelof de Vries. Applying x-rays in material analysis. *Nuclear Instruments and Methods in Physics Research Section A: Accelerators, Spectrometers, Detectors and Associated Equipment*, 509(1):290 – 293, 2003. Proceedings of the 4th Internatonal Workshop on Radiation Imaging Detectors.

[73] Hans Jrgen Korsch, Hans-Jrg Jodl, and Timo Hartmann. *Chaos*. Springer-Verlag Berlin Heidelberg, 2008.

[74] D. Krause and P. Thörnig. Jureca: General-purpose supercomputer at jülich supercomputing centre. *JLSRF*, 2:A62, 2016.

[75] William L. Kruer. *The Physics Of Laser Plasma Interactions*. Avalon Publishing, 2003.

[76] Brookhaven National Laboratory. National synchrotron light source, 2018.

[77] Juan Francisco Lam, Bernard Lippmann, and Frederick Tappert. Moment theory of self-trapped laser beams with nonlinear saturation. *Optics Communications*, 15(3):419 – 421, 1975.

[78] L.D. Landau and E.M. Lifshitz. *Quantum Mechanics, Non-Relativistic Theory: Volume 3 (Course of Theoretical Physics Series)*. Butterworth-Heinemann, 3rd edition, 1977.

[79] J E Lawler, J Bisognano, R A Bosch, T C Chiang, M A Green, K Jacobs, T Miller, R Wehlitz, D Yavuz, and R C York. Nearly copropagating sheared laser pulse FEL undulator for soft x-rays. *Journal of Physics D: Applied Physics*, 46(32):325501, aug 2013.

[80] W. P. Leemans, A. J. Gonsalves, H.-S. Mao, K. Nakamura, C. Benedetti, C. B. Schroeder, Cs. Tóth, J. Daniels, D. E. Mittelberger, S. S. Bulanov, J.-L. Vay, C. G. R. Geddes, and E. Esarey. Multi-gev electron beams from capillary-discharge-guided subpetawatt laser pulses in the self-trapping regime. *Phys. Rev. Lett.*, 113:245002, Dec 2014.

[81] SPD Mangles, CD Murphy, Z Najmudin, AGR Thomas, JL Collier, AE Dangor, EJ Divall, PS Foster, JG Gallacher, CJ Hooker, DA Jaroszynski, AJ Langley, WB Mori, PA Norreys, FS Tsung, R Viskup, BR Walton, and K Krushelnick. Monoenergetic beams of relativistic electrons from intense laserplasma interactions. *Nature*, pages 535–538, 2004.

[82] Claire Ellen Max, Jonathan Arons, and A. Bruce Langdon. Self-modulation and self-focusing of electromagnetic waves in plasmas. *Phys. Rev. Lett.*, 33:209–212, Jul 1974.

[83] T. Mehrling, J. Grebenyuk, F. S. Tsung, K. Floettmann, and J. Osterhoff. Transverse emittance growth in staged laser-wakefield acceleration. *Phys. Rev. ST Accel. Beams*, 15:111303, Nov 2012.

[84] J. T. Mendonça, B. Thidé, and H. Then. Stimulated raman and brillouin backscattering of collimated beams carrying orbital angular momentum. *Phys. Rev. Lett.*, 102:185005, May 2009.

[85] Parry Moon and Domina Eberle Spencer. Interpretation of the ampre experiments. *Journal of the Franklin Institute*, 257(3):203 – 220, 1954.

[86] Philip Morrison. Extrasolar x-ray sources. *Annual Review of Astronomy and Astrophysics*, 5(1):325–350, 1967.

[87] T. Ohkubo, S. V. Bulanov, A. G. Zhidkov, T. Esirkepov, J. Koga, M. Uesaka, and T. Tajima. Wave-breaking injection of electrons to a laser wake field in plasma channels at the strong focusing regime. *Physics of Plasmas*, 13(10):103101, 2006.

[88] A. Pak, K. A. Marsh, S. F. Martins, W. Lu, W. B. Mori, and C. Joshi. Injection and trapping of tunnel-ionized electrons into laser-produced wakes. *Phys. Rev. Lett.*, 104:025003, Jan 2010.

[89] V.a. Papadichev. An electrostatic undulator with single-polarity feed. *Nuclear Instruments and Methods in Physics Research Section A: Accelerators, Spectrometers, Detectors and Associated Equipment*, 429(1-3):377–385, jun 1999.

[90] B D Patterson, R Abela, H-H Braun, U Flechsig, R Ganter, Y Kim, E Kirk, A Oppelt, M Pedrozzi, S Reiche, L Rivkin, Th Schmidt, B Schmitt, V N Strocov, S Tsujino, and A F Wrulich. Coherent science at the swissfel x-ray laser. *New Journal of Physics*, 12(3):035012, 2010.

[91] C. Pellegrini. The history of x-ray free-electron lasers. *The European Physical Journal H*, 37(5):659–708, Oct 2012.

[92] Herbert C. Pollock. The discovery of synchrotron radiation. *American Journal of Physics*, 51(3):278–280, 1983.

[93] A. Pukhov and J. Meyer-ter Vehn. Relativistic magnetic self-channeling of light in near-critical plasma: Three-dimensional particle-in-cell simulation. *Phys. Rev. Lett.*, 76:3975–3978, May 1996.

[94] A. Pukhov and J. Meyer-ter Vehn. Laser wake field acceleration: the highly non-linear broken-wave regime. *Applied Physics B*, 74(4):355–361, Apr 2002.

[95] Brice Quesnel and Patrick Mora. Theory and simulation of the interaction of ultraintense laser pulses with electrons in vacuum. *Phys. Rev. E*, 58:3719–3732, Sep 1998.

[96] W. Rittershofer, C. B. Schroeder, E. Esarey, F. J. Grüner, and W. P. Leemans. Tapered plasma channels to phase-lock accelerating and focusing forces in laser-plasma accelerators. *Physics of Plasmas*, 17(6):063104, 2010.

[97] P. Roth, G. K. L. Wong, R. Beravat, C. M. Harvey, M. H. Frosz, R. Sopalla, and P. St.J. Russell. Measurement of the orbital angular momentum spectrum in twisted coreless photonic crystal fiber. In *Conference on Lasers and Electro-Optics*, page SW3K.2. Optical Society of America, 2018.

[98] Antoine Rousse et al. Production of a kev x-ray beam from synchrotron radiation in relativistic laser-plasma interaction. *Phys. Rev. Lett.*, 93:135005, Sep 2004.

[99] S. G. Rykovanov, M. Chen, C. G. R. Geddes, C. B. Schroeder, E. Esarey, and W. P. Leemans. Virtual detector of synchrotron radiation (vdsr) - a c++ parallel code for particle tracking and radiation calculation. *AIP Conference Proceedings*, 1507(1):399–403, 2012.

[100] S G Rykovanov, C. G. R. Geddes, J.-L. Vay, C. B. Schroeder, E. Esarey, and W. P. Leemans. Quasi-monoenergetic femtosecond photon sources from thomson scattering using laser plasma accelerators and plasma channels. *J. Phys. B*, 47:234013, November 2014.

[101] S. G. Rykovanov, C. B. Schroeder, E. Esarey, C. G. R. Geddes, and W. P. Leemans. Plasma undulator based on laser excitation of wakefields in a plasma channel. *Phys. Rev. Lett.*, 114:145003, Apr 2015.

[102] S. G. Rykovanov, J. W. Wang, V. Yu. Kharin, B. Lei, C. B. Schroeder, C. G. R. Geddes, E. Esarey, and W. P. Leemans. Tunable polarization plasma channel undulator for narrow bandwidth photon emission. *Phys. Rev. Accel. Beams*, 19:090703, Sep 2016.

[103] Peter Schmser, Martin Dohlus, and Jrg Rossbach. Springer, Berlin, Heidelberg.

[104] C. B. Schroeder, E. Esarey, B. A. Shadwick, and W. P. Leemans. Trapping, dark current, and wave breaking in nonlinear plasma waves. *Physics of Plasmas*, 13(3):033103, 2006.

[105] W Schumaker et al. Making pions with laser light. *New Journal of Physics*, 20(7):073008, 2018.

[106] N. B. Simpson, K. Dholakia, L. Allen, and M. J. Padgett. Mechanical equivalence of spin and orbital angular momentum of light:an optical spanner. *Opt. Lett.*, 22(1):52–54, Jan 1997.

[107] P. Sprangle, E. Esarey, J. Krall, and G. Joyce. Propagation and guiding of intense laser pulses in plasmas. *Phys. Rev. Lett.*, 69:2200–2203, Oct 1992.

[108] P. Sprangle, E. Esarey, and A. Ting. Nonlinear theory of intense laser-plasma interactions. *Phys. Rev. Lett.*, 64:2011–2014, Apr 1990.

[109] P. Sprangle, B. Hafizi, and J. Peñano. Laser-pumped coherent x-ray free-electron laser. *Physical Review Special Topics - Accelerators and Beams*, 12(5):050702, may 2009.

[110] P. Sprangle, C. Tang, and E. Esarey. Relativistic self-focusing of short-pulse radiation beams in plasmas. *IEEE Transactions on Plasma Science*, 15(2):145–153, April 1987.

[111] P. Sprangle, A. Ting, and C. M. Tang. Analysis of radiation focusing and steering in the free-electron laser by use of a source-dependent expansion technique. *Phys. Rev. A*, 36:2773–2781, Sep 1987.

[112] SSRF. Shanghai synchrotron radiation facility, 2018.

[113] Xiao-Dong Su, zhang Heng, Thomas C.Terwilliger, Anders Liljas, Junyu Xiao, and Yuhui Dong. Protein crystallography from the perspective of technology developments. *PMC*, 21:122–153, 2015.

[114] Sami Tantawi, Muhammad Shumail, Jeffery Neilson, Gordon Bowden, Chao Chang, Erik Hemsing, and Michael Dunning. Experimental Demonstration of a Tunable Microwave Undulator. *Physical Review Letters*, 112(16):164802, apr 2014.

[115] Roman Tatchyn. Variable-period electrostatic and magnetostatic undulator designs for generating polarized soft x rays at PEP. *Review of Scientific Instruments*, 60(8):2571, 1989.

[116] Sundaram Thangavelu. *Lectures on Hermite and Laguerre Expansions*, volume 42. Princeton University Press, 1993.

[117] Ulrik I. Uggerhøj. The interaction of relativistic particles with strong crystalline fields. *Reviews of Modern Physics*, 77(4):1131–1171, oct 2005.

[118] D. Umstadter, E. Esarey, and J. Kim. Nonlinear plasma waves resonantly driven by optimized laser pulse trains. *Phys. Rev. Lett.*, 72:1224–1227, Feb 1994.

[119] Motohiro Uo, Takahiro Wada, and Tomoko Sugiyama. Applications of x-ray fluorescence analysis (xrf) to dental and medical specimens. *Japanese Dental Science Review*, 51(1):2 – 9, 2015.

[120] J. Vieira, J. T. Mendonça, and F. Quéré. Optical control of the topology of laser-plasma accelerators. *Phys. Rev. Lett.*, 121:054801, Jul 2018.

[121] N A Vinokurov and E B Levichev. Undulators and wigglers for the production of radiation and other applications. *Physics-Uspekhi*, 58(9):850, 2015.

[122] W. Panofsky W. E. Spicer and E. Garwin. Use of cyclotron radiation from storage ring for solid state studies, 1968.

[123] Henry Snowden Ward. *Practical Radiography: a Hand-book of the Applications of the X-rays*. Pub. for the Photogram, Limited, Dawbarn & Ward, Limited, 1896.

[124] Helmut Wiedemann. *Particle Accelerator Physics*. Springer International Publishing, 2015.

[125] Herman Winick and Bill Kirk. Stanford sychrotron radiation projects, 1975.

[126] Tobias N. Wistisen, Kristoffer K. Andersen, Serdar Yilmaz, Rune Mikkelsen, John Lundsgaard Hansen, Ulrik I. Uggerhøj, Werner Lauth, and Hartmut Backe. Experimental realization of a new type of crystalline undulator. *Physical Review Letters*, 112(25):1–4, 2014.

[127] H. Xu., W. Chang, H. Zhuo, L. Cao, and Z. Yue. Parallel programming of 2 1/2-dimensional pic under distributed-memory parallel environments. *Chin. J. Comput. Phys.*, 19:305 (in Chinese), 2002.

[128] Alison M. Yao and Miles J. Padgett. Orbital angular momentum: origins, behavior and applications. *Adv. Opt. Photon.*, 3(2):161–204, Jun 2011.

[129] Z. T. Zhao et al. First lasing of an echo-enabled harmonic generation free-electron laser. 6(6):360–363, 2012.

[130] M. Zolotorev. Laser driven attosecond SASE X-ray FEL. *Nuclear Instruments and Methods in Physics Research Section A: Accelerators, Spectrometers, Detectors and Associated Equipment*, 483(1-2):445–448, May 2002.

List of scientific publications and presentations

1. B. Lei, T. Teter, J. Wang, V. Kharin, M. Zepf, C. B. Schroeder and S.G.Rykovanov, Flexible X-ray source with tunable polarization and orbital angular momentum from Hermite-Gaussian laser modes driven plasma channel wakefield , Phy. Rev. Accel. Beams 22, 071302 2019.

2. B. Lei, J. Wang, V. Kharin, M. Zepf, and S. Rykovanov, γ-Ray generation from plasma wakefield resonant wiggler, Phys. Rev. Lett. 120, 134801 2018.

3. B. Lei, J. Wang, and S. Rykovanov, γ-Ray generation from plasma wakefield resonant wiggler, PHEDM-Hirschegg Workshop, 2017

4. S.G. Rykovanov, J.W. Wang, V.Yu. Kharin, B. Lei, C.B. Schroeder, C.G.R. Geddes, E. Esarey, and W.P. Leemans, Tunable polarization plasma channel undulator for narrow bandwidth photon emission, Phys. Rev. Accel. Beams 19, 090703, 2016

5. B. Lei, J. Wang, V. Kharin, and S. Rykovanov, Helical plasma channel undulator, PHEDM-Hirschegg Workshop, awarded as Poster Prize, 2016

6. B. Lei, et al., Numerical study of self-modulation process in PWFA, TEMF-DESY Collaboration, Hamburg, 2015

7. B. Lei, ASTRA simulation of transport system for PITZ Plasma experiment, PITZ, Zeuthen,2014

8. LEI Bi-feng, et al., Study on a MicroTCA-EPICS based Control System; Atomic Energy Sci. and Tech., p545-549, vol.03. 2014

9. LV Hui-hui, LEI Bi-feng, et al., CSNS Control Cable Information Management System Based on Web, Atomic Energy Sci. and Tech., p555-558, vol.03, 2014

10. LIU Zhengtong, LEI Bi-feng, et al., Research on PCI-e Bus Based EPICS System, Nuclear electronic and detection technology, p657-661, vol.06, 2013